ENHANCEMENT OF NEAR-INFRARED DIFFUSE OPTICAL TOMOGRAPHY FOR PROSTATE CANCER IMAGING

By

GUAN (GARY) XU

Bachelor of Science in Electrical Engineering
Hebei University of Technology
Tianjin, CHINA
2006

Submitted to the Faculty of the
Graduate College of the
Oklahoma State University
in partial fulfillment of
the requirements for
the Degree of
DOCTOR OF PHILOSOPHY
December, 2011

ENHANCEMENT OF NEAR-INFRARED

DIFFUSE OPTICAL TOMOGRAPHY FOR

PROSTATE CANCER IMAGING

Dissertation Approved:

Dr. Daqing Piao

Dissertation Adviser

Dr. Jerzy S. Krasinski

Dr. James C. West

Dr. Charles F. Bunting

Dr. Wei Yin

Outside Committee Member

Dr. Sheryl A. Tucker

Dean of the Graduate College

TABLE OF CONTENTS

LIST OF TABLES

LIST OF FIGURES

CHAPTER I

BACKGROUND AND INTRODUCTION

1.1 Theoretical feasibility

Biological tissue is highly scattering at near-infrared (NIR) wavelengths (600-1000nm), and it can be observed from Fig.1.1 that in the range of 700-900nm, the absorption of water is much lower than that of oxygenated hemoglobin and deoxygenated hemoglobin. Both features ensure considerable penetration depths and possibility of the measuring tissue oxygen saturation level with Near-infrared light. With such theoretical basis and assuming homogeneity in biological tissue, Near-infrared optical spectroscopy has been developed to monitor the hemoglobin concentration and oxygen saturation in human tissue with a single source-detector pair. Subsequently, it is demonstrated that with multiple measurements, the heterogeneities of the hemoglobin concentration and oxygen saturation level can actually be resolved, which extends the spectroscopy system to a tomography system [1].

The method is successfully implemented in imaging applications such as the diagnosis of breast and prostate cancer, the analysis of premature infant brain activities, and imaging of small animals as optical contrast generated by functional variation of biological tissue is sufficiently high for near-infrared light. However, since scattering dominates the photon propagation in biological tissue in the near-infrared band, the resolution of NIR tomography is relatively low.

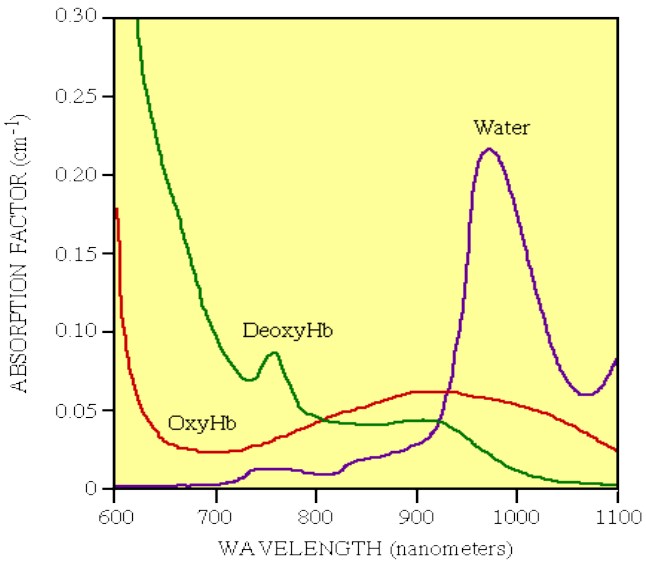

Fig.1.1 Absorption spectrum of human tissue in near-infrared band

1.2 Computational modeling

The propagation of photon flux can be analytically modeled by the diffusion approximation of the radiative transfer equation, which will be specified in later in this study. For imaging geometry, human tissue can be modeled as either infinite (optode insertion, Fig 1.2(a)) or semi-infinite (surface detection, Fig 1.2(b)).

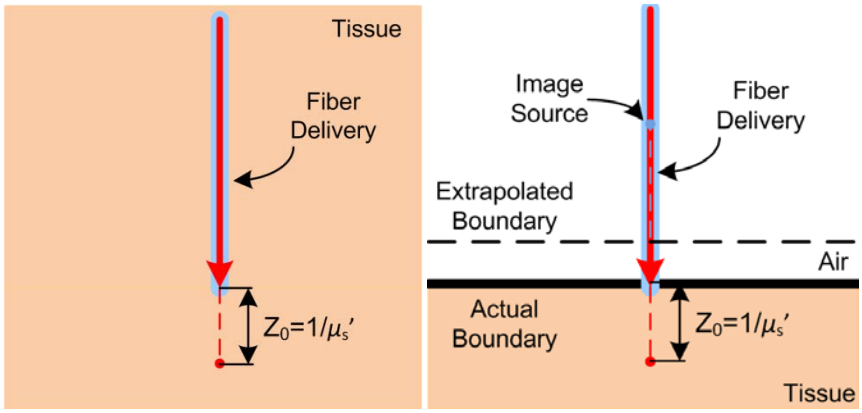

(a) Infinite medium (b) Semi-infinite medium

Fig.1.2 Models of light propagation in infinite and semi-infinite medium

In Fig. 1.2 μ_s' is the inverse of the distance where the intensity of incident light is scattered to 1/e and at such condition, the scattered light can be regarded as an isotropic source.

The modeling of NIR spectroscopy and tomography consists of two parts: 1) a forward model, which represents the light interaction to the medium being imaged; and 2) an inverse model, which is solved for the optical properties of the imaged medium.

For the forward model of NIR spectroscopy, explicit analytical solution of the light propagation can be solved. As is shown in Fig 1.2(a), by assuming that all the photons are initially scattered at a depth of Z_0 (the inverse of reduced scattering coefficient μ_s'), the photon propagation in an infinite medium can be solved. For a semi-infinite medium, by applying mirror method with the precondition that photon density is zero at the extrapolated boundary, the solution for the photon propagation in infinite medium is derived. However, for more complicated tomography cases, which reconstructs the spatially varied of optical property distribution, numerical methods such as finite element method and finite difference method are used. As to inverse model, NIR spectroscopy only involves the solution of the analytical equation set while tomography reconstruction iteratively fits the forward model to the actual measurements.

Although the forward model based on finite element and finite difference methods reliably produces a unique solution, there exists disagreement of uniqueness for the inverse model of the imaging technique, especially on systems generating only steady state measurement. This problem will be discussed throughout this study and approaches ensuring the unique solutions will be introduced.

1.3 Reconstruction enhancements with *a priori* information

Despite careful design of computational methods and instrumentation, since near-infrared tomography bases on the interaction between diffused photon and turbid media, the spatial resolution of the imaging modality is relatively low (Fig.1.3). Furthermore, non-uniform spatial and spectral sensitivity with respect to the optical contrast also limits the resolving power of the

imaging technique. Many enhancement approaches have been investigated for more reliable image reconstruction.

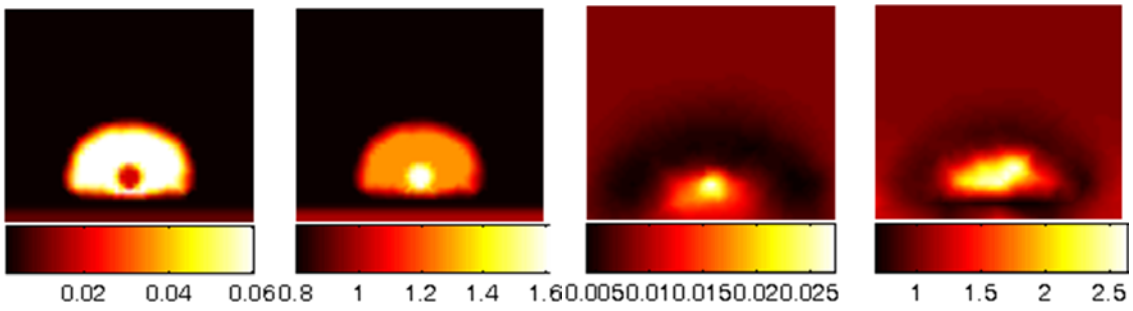

(a) Forward model (b) Reconstructed image

Fig.1.3 Low spatial resolution of optical tomography. The structures in the forward model cannot be recovered by pure DOT reconstruction

1.3.1 Spatial *prior*

As is shown in Fig1.4-1.7, the imaging modalities such as x-ray, ultrasound, and magnetic resonance imaging (MRI) provide higher imaging resolution but low functional contrast in biological tissue, which is opposite to optical diffuse imaging. Compensating optical imaging with spatial *a priori* information extracted from ultrasound or MRI imaging can potentially improve the specificity of DOT to malignant tissue.

Fig.s 1.4 [2] and 1.5 [3] demonstrated the MRI spatial *a priori* information extraction and its integration into the geometry generation and region division of the finite element meshes.

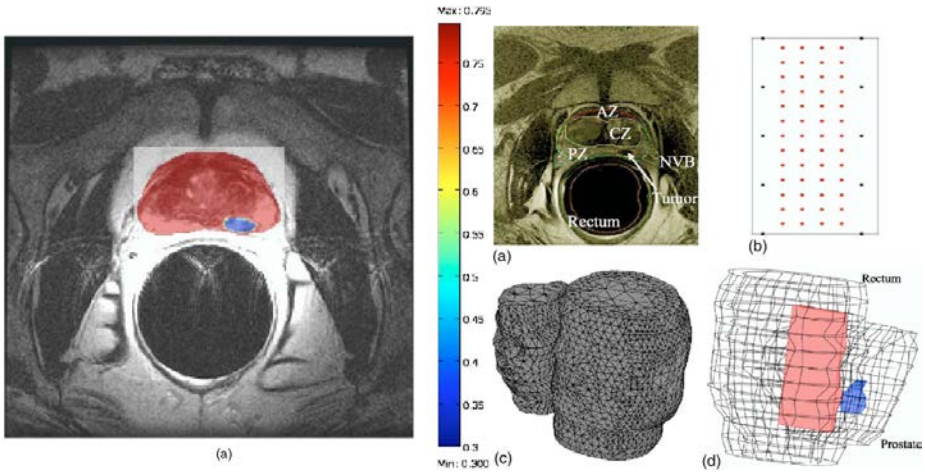

Fig. 1.4 MRI *a priori* information utilization in NIR tomography on prostate cancer diagnosis

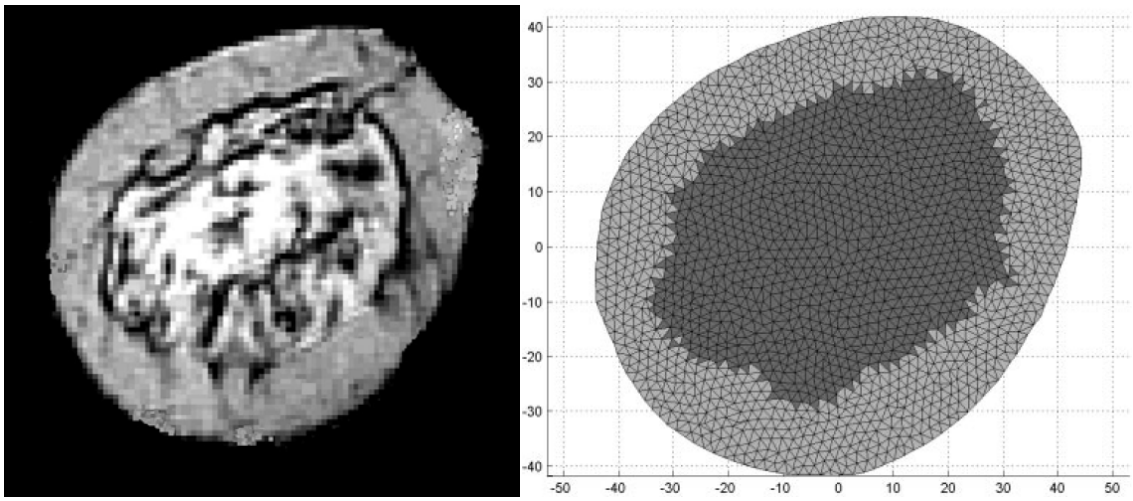

(a)MRI image (b) FEM mesh

Fig.1.5 MRI *a priori* information utilization in NIR tomography on brain functional imaging

Compared to the huge system volume of MRI a more compact imaging modality, more compact and portable ultrasound imaging devices have also been integrated to optical tomography systems. The pioneering works of ultrasound *prior* guided optical tomography reconstruction was conducted in optical imaging group of University of Connecticut. As is shown

in Fig.1.6 [4], the suspicious region detected by ultrasound imaging modality is marked and densely segmented for higher sensitivity.

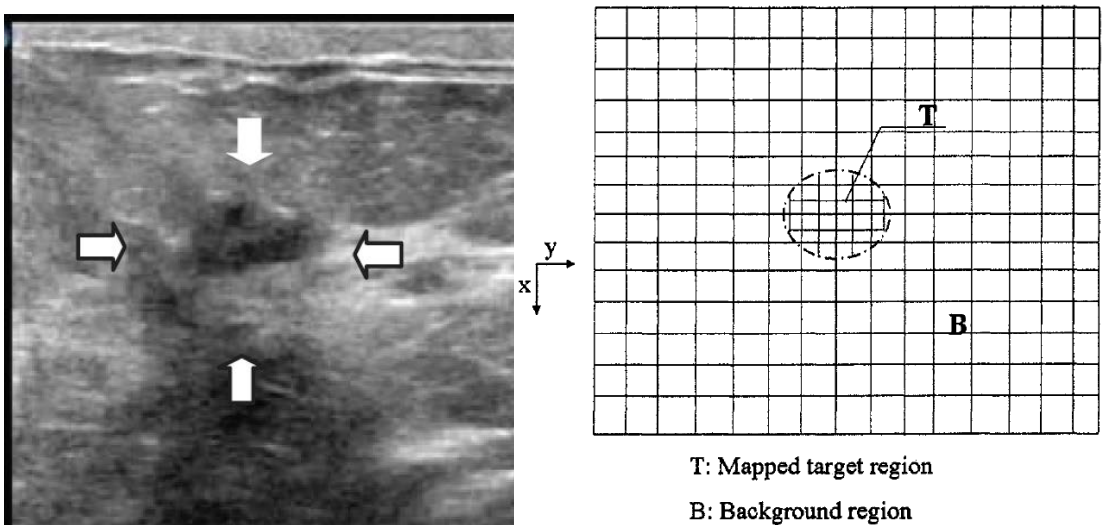

(a) (b)

Fig.1.6 Ultrasound *a priori* information utilization NIR tomography on brain functional imaging. (a) Ultrasound image with suspicious target region marked (b) FEM mesh generated integrating the spatial *prior* information

Since trans-rectal ultrasound is widely used in prostate cancer diagnosis and prostate biopsy guidance, our system integrates a sagittal trans-rectal ultrasound imager for struactral *prior* extraction. Fig.1.7 [5] displays one set of experiment on canine cadaver conducted by our group.

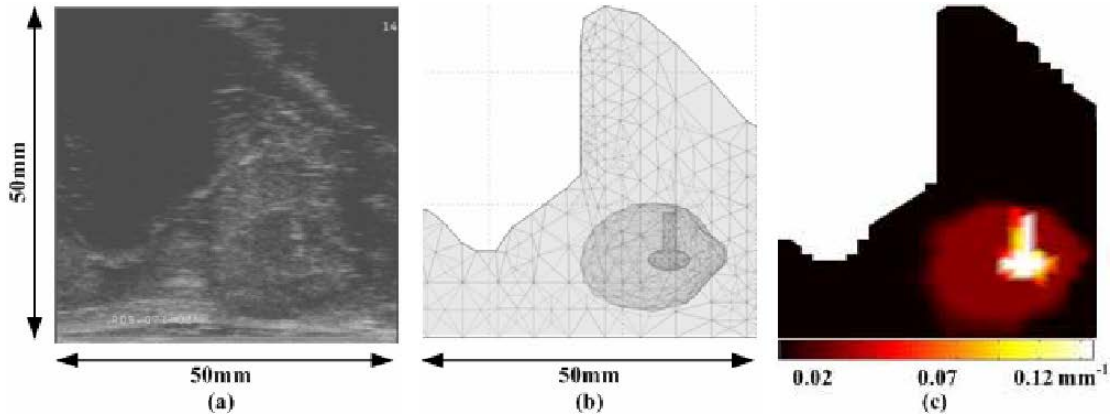

Fig.1.7 Ultrasound *a priori* information utilization NIR tomography on canine cadaver experiment. (a) Ultrasound image (b) FEM mesh (c) Optical tomography image

The application of spatial *prior* is not limit to FEM generation but also contribute to inverse problem regularization. Two categories of methods: hard and soft *prior* integration to reconstruction algorithms are practiced and discussed in several literatures [6]. Hard *prior* method basically divides the imaging volume into several regions according to the contours observed from the *prior* providing image and assumes optical property homogeneity within each region. This method substantially reduced the unknown optical properties values compared to traditional reconstruction methods (number of regions versus number of nodes in FEM mesh) and generate high optical property recovery accuracy. Whereas the soft *prior* method still reconstructs the optical properties of each node of the FEM mesh yet the update ratio of the suspected region is intentionally elevated, producing weighted sensitivity distribution, improving the reconstruction reliability [6]. However, the structural *prior* method will not be applicable at occasions where the malignant tissue cannot be visibly segmented. Chapter 2 of this dissertation presents a novel reconstruction algorithm based on hard *prior* for stable iteration convergence in an endoscopic prostate cancer imaging.

1.3.2 Spectral *prior*

Another type of *prior* utilizes the variation of absorptive and scattering properties of chromophores with respect to wavelength spectrum to generate multiple sets of measurements from identical imaging geometry. Therefore, the ill-posed-ness of the inverse problem can be fundamentally reduced, leading to more determinant reconstruction results. As is shown in Fig.1.8[7] with multiple spectral measurements, the reconstruction variable becomes the concentration of the chromophores and the scattering parameter, all of which are constant but can produce different absorption and scattering optical properties with respect to the wavelengths.

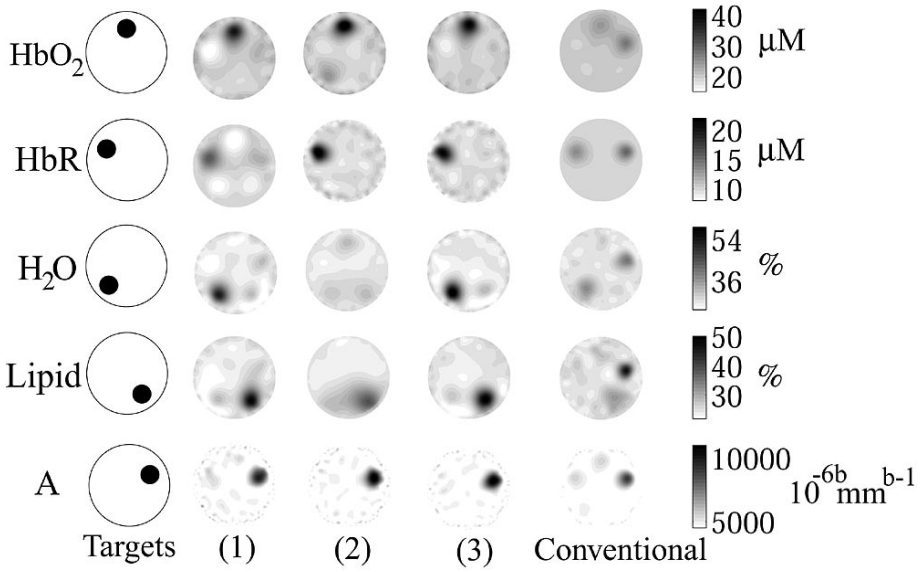

Fig.1.8 Multi-spectral optical tomography. (1) (2) (3) are reconstruction results with measurements at different wavelengths

Fig.1.9 (a) and (b) demonstrates multi-spectral tomography systems with 2 and 6 wavelengths, respectively. Since the uniqueness of such system structure with steady state measurement has been proved by previous studies, it is attractive to obtain reliable reconstruction by implementing multiple light sources to steady state measurement systems instead of constructing of complicated and expensive frequency domain systems. However, few studies have compared the performance between steady state and frequency domain system, which will be the topic of chapters 3 and 4 of this dissertation. Moreover, reconstruction artifact estimation and optimum wavelength selection methods are also introduced base on the theoretical analysis in chapters 3 and 4.

1.4 Spatially variant sensitivity distribution

In DOT, a spatially non-uniform sensitivity can be observed in most of the imaging geometry, especially in the reflectance imaging geometry for brain activity monitoring and endoscopic imaging geometry for prostate cancer detection. The spatially non-uniform sensitivity is unfavorable due to the resulted non-uniformity in contrast, resolution, and particularly the

biased localization of an occlusion toward the position of local sensitivity maxima [6, 8-11], as is shown in Fig. 1.9.

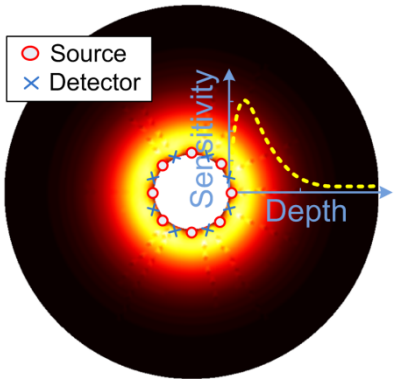

Fig.1.9 Spatial sensitivity profile of an endoscopic. Severe sensitivity magnitude variation induces inaccurate target localization in radial direction

Several previous studies have implemented a weighting matrix to counterbalance the degradation of the spatial sensitivity. However, such arbitrary factor could introduce artifacts in the reconstructed images. In chapter 6 of this dissertation, a geometric differential sensitivity method is presented. The method rescales the solution domain of the inverse problem of DOT by linear transformation, leading to spatially less variant sensitivity profile and more accurate target depth localization.

1.5 Instrumentation

The instrumentation design of NIR tomography system is determined by the system measurement type (steady state or frequency domain, single or multiple wavelengths) and light delivery/collection approaches. In this study, we focus on the instrumentation of steady state measurement systems.

The most commonly implemented system structure is mechanical source-detector switching. As is shown in Fig 1.10(a)[12], which is the schematics of our current clinical experiment system, the system integrates two wavelengths with a bifurcated fiber and delivers the source light to each source channel by horizontal displacement stage controlled by a PC. Similarly, system in Fig. 1.10(b) [13] implements a rotational plate to switch the detector

channels. Both systems possess the advantage of using single light source, ensuring the source intensity uniformity and signal independence. However, in medical imaging scenarios, it is never desirable that the sequential, physical displacement of either the source or detector channels limits data acquisition rate.

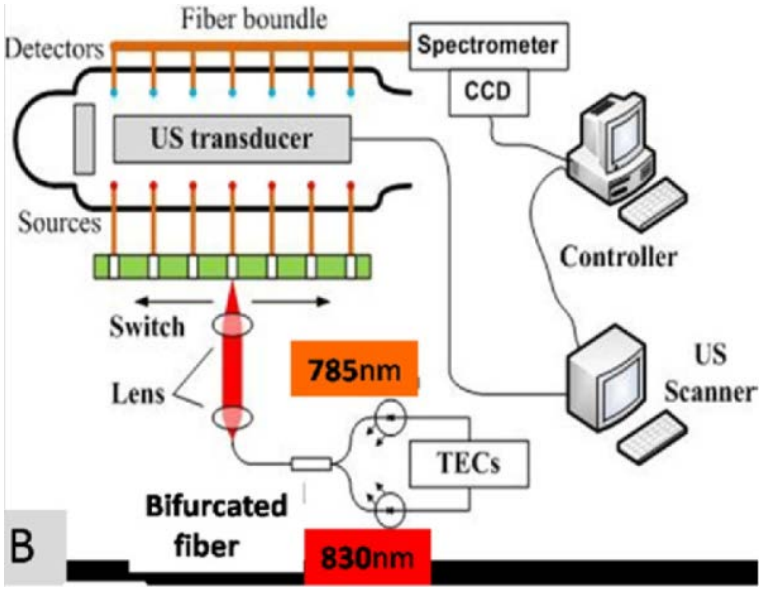

(a)

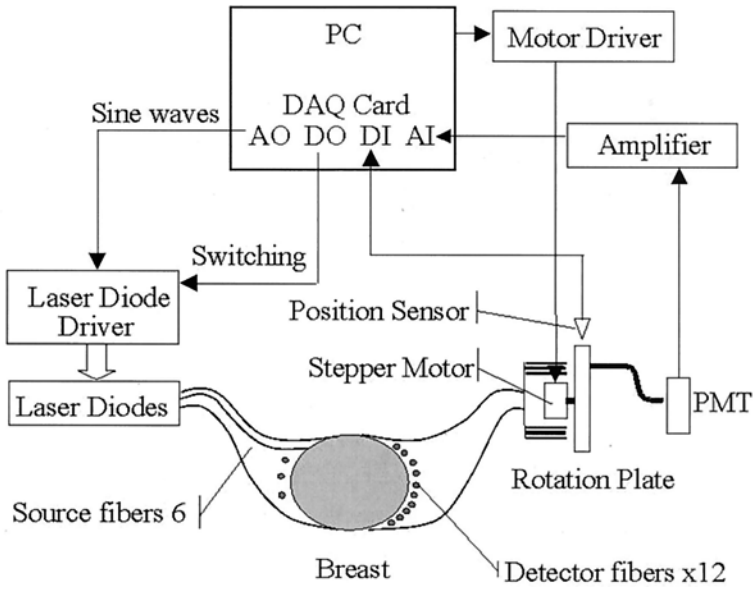

(b)

Fig 1.10 Mechanical switching. (a) Source channel switching system currently used in Oklahoma State University laboratory; (b) Detector channel switching system constructed by University of Connecticut

Rapid data acquisition systems are designed and constructed for capturing instantaneous variation of the optical property distributions in the imaging domain. As is shown in Fig.1.11 [14], both system facilitate the data acquisition from all sources and detector channel by source channel spectral encoding. Fig.1.11(a) realize the encoding by using multiple laser diodes, while Fig.1.11(b) utilizes a low coherent broadband light source. The details of these two rapid NIR tomography systems structure will be discussed in chapter 5 of this dissertation along with a novel wavelength encoding instrumentation approach.

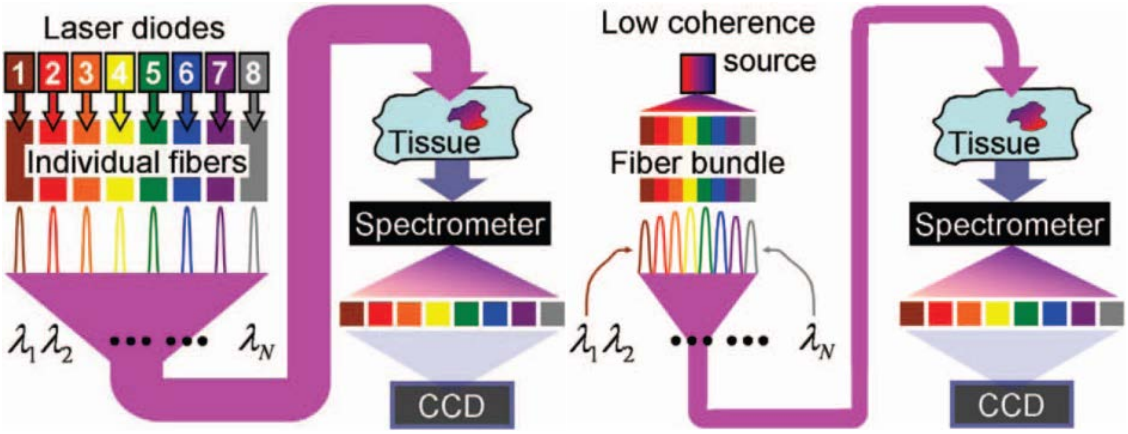

Fig 1.11 Rapid data acquisition near-infrared tomography systems. (a) System structure with multiple laser diodes; (b) System structure with multiple low coherent broadband light source

1.5 Fluorescence

Besides all the computational and instrumentation improvement of the diffuse optical tomography mentioned above, the administration of fluorescence emitting material provides an ultimate optical contrast enhancement. However, the feasibility of such approach requires the specificity of the fluorescence agent to either the background or the target. In this study, fluorescence optical tomography for prostate cancer detection will be proposed based on a zinc-

specific flurorophor under development of a bio-tech company NeuroBio Tex Inc. in Galveston, TX. One feature distinguishes the zinc-specific fluorophor from the previous investigated ones is that instead of producing fluorophor uptake within the malignant tissue, it concentrates in the benign tissue region. Therefore, the imaging scenario will be imaging a dark target within a bright ambience, which will be subjective to significant noise level in the measurement.

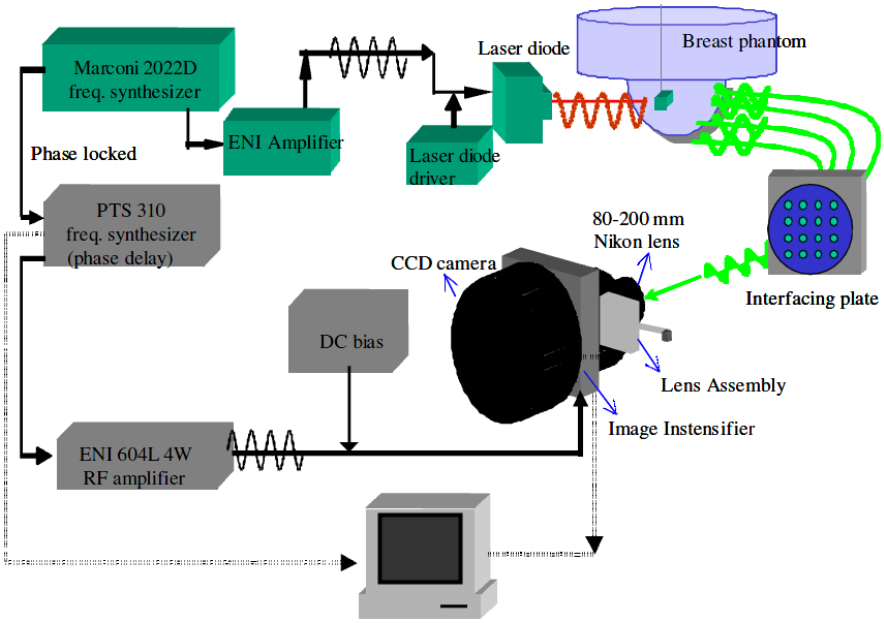

Fig.1.12 Instrumentation of a frequency domain fluorescence optical tomography system

Fluorescence enhanced optical tomography includes the modeling of light propagation at two wave bands, the excitation band and emission band. Fig.1.12 [15] shows the structure of a frequency domain fluorescence optical tomography system for breast cancer detection.

An optical filter will also be added because the significant magnitude difference between the excitation and emission band signal might exceed the dynamic range of the CCD camera, which will be detailed in chapter 7 of the study.

Since fluorescence emission spectral does not vary with respect to the excitation wavelengths, the traditional rapid system captures light signal from all sources by spectral encoding cannot be transformed to fluorescence optical tomography. Chapter 5 introduces a

spectral and temporal encoded excitation band source light can, which facilitates rapid fluorescence tomography data acquisition. A series of experiments will be designed and conducted to validate the system design.

1.6 Summary

This dissertation includes the author's works on both the computational and instrumentation aspects on the prostate cancer detection with near-infrared optical tomography. Finally the experiment setup negative contrast fluorescence enhanced optical tomography is designed and preliminary validated by simulation studies.

CHAPTER II

NEAR-INFRRARED DIFFUSE OPTICAL TOMOGRAPHY RECONSTRUCTION WITH SPATIAL *PRIOR*

2.1. Introduction

Prostate cancer is the 2nd most commonly diagnosed cancer and the 2nd leading cause of cancer deaths in American men [16]. Prostate cancer screening is recommended by use of digital rectal examination (DRE), measurement of serum prostate-specific antigen (PSA) [17], and a combination of these tests [18]. The introduction of PSA screening test has resulted in substantially increased detection of organ-confined prostate cancer or considerable stage migration [19]. However, PSA is not a specific indicator of prostate malignancy and post-treatment tumor recurrence, except after radical prostatectomy [20]. Only a clearly increased serum PSA value (>20 ng/ml) indicates the presence of a prostate carcinoma at a very high probability. In the gray zone between 4 and 10 ng/ml the tissue marker PSA is frequently influenced by benign alterations, so that it is not possible—on the basis of the PSA value alone—to differentiate between benign and malignant cases [21-22]. DRE can often distinguish between prostate cancer and non-cancerous conditions. DRE may also detect prostate cancers having normal PSA levels. However, palpation during a DRE is subjective, insensitive, and more than half of all prostate cancers detected today are not palpable [18]. When the suspicion of prostate cancer is raised by abnormal PSA and/or DRE, the diagnostic regarding the onset and the

clinical significance of the tumor can be made only by biopsy. Today, the technique of trans-rectal ultrasound (TRUS) based trans-rectal prostate biopsy, carried out with a semi-automatic coil spring device and an 18-gauge needle, is considered as the gold standard [21].

Prostate cancer may be identified on TRUS as a hypo-echoic lesion [23]. However, at most 60% cancers appear hypo-echoic on TRUS while most of the remaining cancers appear iso-echoic with respect to the surrounding parenchyma [24]. There can be hypo-echoic, cancer-suspicious areas that may be histologically either benign or malignant. TRUS can display the needle trajectory accurately, but it does not differentiate a tumor reliably from normal tissues. The lack of TRUS specificity thereby prompts the "systematic biopsy" strategy with a preference in the peripheral zone where most prostate cancers are found, rather than just sampling an area abnormal on DRE or TRUS. However, despite years of research, the exact number of biopsies to be taken is still largely unknown [25]. The current trend is to use 10- to 12-core biopsy without the transition zone as the initial biopsy strategy. A significant number of biopsies are negative, and in men with persistent suspicion of prostate cancer after several negative biopsies, more extensive protocols (>12 cores) up to saturation biopsy (24 cores) represent a necessary diagnostic procedure [26].

The need for many biopsy-cores for systematic, yet random, tissue sampling of the prostate may be alleviated if the acoustic contrast that TRUS relies on can be augmented with functional or "surrogate" markers of the prostate tumor. The augment of a functional contrast may lead to sampling of the most suspicious lesions. Augmenting TRUS may also desire that such a functional imaging modality be non-invasive and non-ionizing as is TRUS. Optical tomography based on near-infrared (NIR) light could emerge as one such modality.

Near-infrared measurements of attenuation through tissue have demonstrated significant contrast gradients between blood and parenchymal tissue that is otherwise difficult to obtain [27-32]. The alteration of vascularity or the hemoglobin content in the tumor renders high intrinsic optical contrast between the tumor and benign tissues. This high NIR tumor-tissue contrast has

been well-demonstrated in functional imaging of breast cancer [27-32]. When multi-spectral detection is engaged, NIR imaging is also known for direct quantification of chromorphore concentration that is important for characterization of the malignancy [27-32]. In prostate, studies have shown vascular density gradient in malignant versus benign tissue specimens [33], and different water concentrations in cancerous and benign tissues *in vitro* [34]. Invasive NIR measurements of prostate have been reported for experimental prostate tumors [35] and human prostate [36-37]. Surface measurements of implanted prostate tumors have also been conducted [36, 38-39]. These studies have been based on using NIR to detect the prostate cancer. In fact NIR diffuse optical measurement, performed interstitially, is becoming an important tool for monitoring photodynamic therapy in prostate [36-37]. Non-invasive NIR imaging of the prostate has also been analyzed and attempted via trans-urethral probing [2, 40]. Recently, trans-rectal NIR imaging of the prostate has been investigated in simulation in the context of assisting MRI for treatment decision [27]. Trans-rectal probing is undoubtedly the most suitable way of prostate imaging for optical means. This probing option, however, indicates that trans-rectal optical imaging may be combined with TRUS to provide broader clinical utility, e.g. prostate screening and biopsy guidance.

To our knowledge, experimental work on trans-rectal NIR tomography has not been conducted except for our recent attempts [41-42]. This may largely due to the challenge of fabricating an applicator for trans-rectal probing. Optical tomography typically needs 10s of channels of NIR optodes in order to achieve reasonable spatial resolution within a large tissue volume being interrogated. The NIR illumination can be delivered by small diameter fibers, but the detection of weak scattered light prefers using fibers of large diameters and/or large numerical apertures. Unlike breast NIR tomography where there is minimum spatial restriction of the optode deployment, trans-rectal prostate NIR tomography has to deploy many optodes in a very compact space. This restriction could become more pronounced when trans-rectal NIR tomography is to be combined with TRUS. Since the depth of tissue interrogation by diffuse NIR light is

approximately one-half of the source-detector separation for typical scattering-dominant biological tissue, reaching targets centimeters deep in prostate implies an NIR array dimension of several centimeters. Trans-rectal administration of an NIR array of such dimension would be feasible if the optodes are arranged longitudinally to provide sagittal-view trans-rectal NIR imaging. The images obtained by trans-rectal NIR tomography alone would, however, be difficult to correlate with the anatomy. Unlike breast imaging where the NIR applicator can be accurately positioned, accurate positioning of a trans-rectal NIR applicator with respect to the prostate is difficult due to the "blind" intra-pelvic location of the prostate, slow NIR image reconstruction, and lack of anatomic details in NIR tomography images. It is thereby imperative to use a real-time morphological imaging modality concurrently with trans-rectal NIR tomography to provide positioning guidance for NIR applicator to correlate the NIR tomography findings with the prostate anatomy, and more importantly to use the structural information of the prostate as the *prior* [43] to improve the accuracy of NIR image reconstruction. Among the standard prostate imaging techniques, TRUS is perhaps the best modality for combining with trans-rectal NIR tomography if the clinical endpoint is defined for screening and biopsy targeting. The integration of trans-rectal NIR tomography with TRUS could augment the US anatomic details with NIR functional contrast.

The benefit of complement NIR contrast to ultrasound has been demonstrated in breast imaging [44-45]. The methodology of combining NIR/US can certainly be extended from breast imaging to prostate imaging; nevertheless, the technique of combining NIR with US cannot be applied directly from imaging the breast to imaging the prostate without a combined NIR/US applicator suitable for trans-rectal manipulation. In this work, we demonstrate the feasibility of trans-rectal NIR optical tomography of prostate in the context of combining NIR with TRUS. This work is separately reported in two consecutive papers. The Part-I paper, based solely on simulation, investigates designs of NIR tomography applicator that can be integrated with a commercial TRUS transducer. The Part-II paper implements the probe design suggested by the

Part-I paper, presents the details of the instrumentation of the combined trans-rectal NIR/US imager, and demonstrates the feasibility of concurrent trans-rectal NIR/US imaging in phantoms and tissue samples including canine prostate *in situ*. In this Part-I paper a hierarchical image reconstruction routine is developed for taking advantage of the TRUS structural *a priori* information. This hierarchical reconstruction method is then used to evaluate a number of NIR applicator designs. The results suggest a working geometry of the trans-rectal NIR array that can be integrated with a TRUS transducer.

2.2. Preliminaries

2.2.1 Working geometry of sagittal trans-rectal NIR array for coupling with sagittal TRUS

A bi-plane (sagittal and transverse) TRUS probe is commonly used in prostate clinics. Sagittal and transverse views are frequently switched during prostate imaging, but for the biopsy procedure, the spring-loaded needle is fired in the sagittal plane wherein the needle trajectory is accurately marked. We have acquired a bi-plane TRUS probe (Aloka UST-672-5/7.5) as is shown in Fig.2.1(a). This bi-plane TRUS probe has a sagittal transducer spanning 60mm×10mm and a transverse transducer spanning 120°×10mm. The cylindrical TRUS probe has a maximum diameter of 20mm at its distal end. Integrating NIR optical tomography array to this TRUS probe implies that the radial and longitudinal dimensions of the NIR array are quite limited. For NIR tomography, longer source-detector separation is needed to interrogate deeper targets. The rectal insertion also limits the radial extent of the combined probe. Under these conditions, a feasible NIR array geometry may be distributing a single line of optodes on each lateral side of the sagittal TRUS transducer as illustrated in Fig.2.(b). Considering the supporting structure of the optodes, the combined probe will likely have a cross-section that is at least a few millimeters larger than the diameter of the TRUS probe. NIR tomography has to use multimode fibers to allow detection of weak diffuse light, and these multimode fibers must be delivered longitudinally before being side-fired. Bending the fiber is not a viable solution here for side-firing unless the fibers are

passed inside the TRUS probe. The side-firing alternatively may be realized by implementing micro-optical components. Since the compact space inside or surrounding the probe cannot accommodate too many channels of multi-mode NIR fibers, we propose that a working geometry of the NIR array for coupling to TRUS is to have 7 channels on each lateral side of the TRUS to span 60mm longitudinally as the TRUS transducer window does and the optical channels have 10mm spacing. The NIR array must leave the 10mm-wide sagittal TRUS transducer unblocked; therefore a 20mm separation of the NIR optodes from one lateral side to the other is needed. These considerations lead to the NIR array geometry shown in Fig.2.1(c) where 14 optodes are spaced 10mm longitudinally and 20mm laterally. Fig.2.1(d) illustrates an NIR/US probe if the sagittal NIR array can be fabricated synergistically with the TRUS probe.

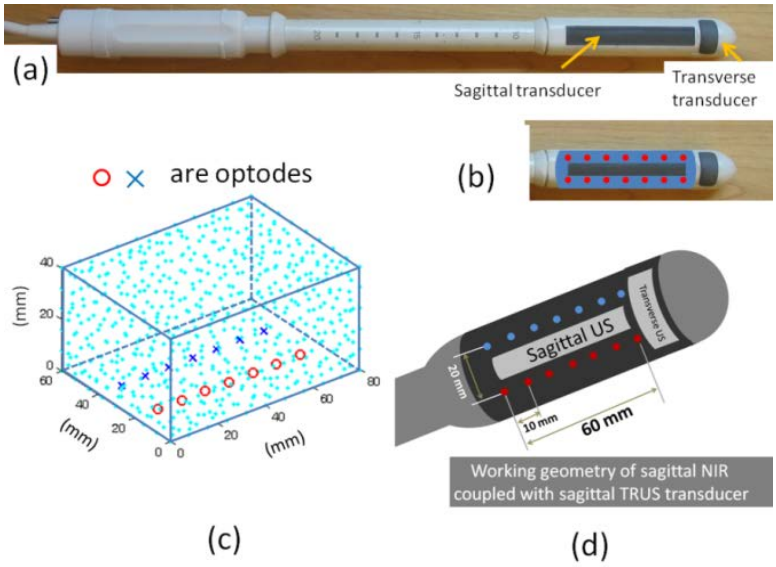

Fig.2.1 Geometry of the TRUS-DOT combined probe (a) Photograph of a bi-plane TRUS transducer. (b) A feasible geometry of NIR array for coupling with sagittal TRUS transducer. (c) The NIR imaging geometry for the one depicted in (b). (d) Cartoon-art illustration of a fully-integrated sagittal trans-rectal NIR/US probe.

2.2.2 Forward and inverse methods for sagittal trans-rectal optical tomography

The prostate and peripheral tissues are scattering-dominant [34-37]. The light propagation in scattering-dominant tissue can be modeled using the diffusion approximation to the radiative transport equation. We use the well-known frequency-domain photon diffusion equation [46]:

$$-\nabla\cdot\kappa(\vec{r})\nabla U(\vec{r},\omega)+(\mu_a+\frac{i\omega}{c})U(\vec{r},\omega)=q_0(\vec{r},\omega) \tag{2.1}$$

where $U(\vec{r},\omega)$ is the photon fluence rate at position $\vec{r}$, $q_0(\vec{r},\omega)$ is the source term, ω is the source modulation frequency, c is the speed of light in medium, μ_a is the absorption coefficient, and $\kappa=[3(\mu_a+\mu_s')]^{-1}$ is the diffusion coefficient with μ_s' being the reduced or transport scattering coefficient.

We use finite-element method [47] to solve equ. (2.1) under the Robin-type boundary condition [46]

$$U(\vec{r}_0,\omega)+2\kappa A\hat{n}_0\cdot\nabla U(\vec{r}_0,\omega)=0 \tag{2.2}$$

at the boundary $\vec{r}_0$, where $\hat{n}_0$ is the outward normal vector of the boundary, *A* is the refractive index mismatch coefficient. The refractive indices of air and tissue are 1 and 1.33 respectively, for the tissue-air boundary, leading to *A*=2.82 as in [46].

The imaging volume for trans-rectal optical tomography can be divided approximately to 4 domains or regions-of-interest (ROIs): the rectum wall, the peri-prostate tissue, the prostate, and the prostate tumor. When a prostate lesion is shown suspicious on TRUS, the thickness of the rectum wall, the size/shape of the prostate, and the spatial information of the prostate lesion can be used to guide the trans-rectal NIR image reconstruction. The TRUS structural information is utilized in this work as the "hard" *prior* [43-45]. The "hard" *a priori* method treats each ROI as homogenous; thereby 8 parameters are to be recovered for the μ_a and μ_s' in the four ROIs. The Jacobian values are calculated for each ROI instead of for each node in every ROI and has the form of:

$$\begin{bmatrix} \frac{\partial \ln I_{11}}{\partial \mu_{a\_rect}} & \frac{\partial \ln I_{11}}{\partial \mu_{a\_peri}} & \frac{\partial \ln I_{11}}{\partial \mu_{a\_pros}} & \frac{\partial \ln I_{11}}{\partial \mu_{a\_lesi}} & \frac{\partial \ln I_{11}}{\partial \mu'_{s\_rect}} & \frac{\partial \ln I_{11}}{\partial \mu'_{s\_peri}} & \frac{\partial \ln I_{11}}{\partial \mu'_{s\_pros}} & \frac{\partial \ln I_{11}}{\partial \mu'_{s\_lesi}} \\ \frac{\partial \ln I_{12}}{\partial \mu_{a\_rect}} & \ddots & \ddots & \vdots & \vdots & \ddots & \ddots & \vdots \\ \vdots & \ddots & \ddots & \vdots & \vdots & \ddots & \ddots & \vdots \\ \frac{\partial \ln I_{77}}{\partial \mu_{a\_rect}} & \cdots & \cdots & \frac{\partial \ln I_{77}}{\partial \mu_{a\_lesi}} & \frac{\partial \ln I_{77}}{\partial \mu'_{s\_rect}} & \ddots & \ddots & \frac{\partial \ln I_{77}}{\partial \mu'_{s\_lesi}} \\ \frac{\partial \phi_{11}}{\partial \mu_{a\_rect}} & \frac{\partial \phi_{11}}{\partial \mu_{a\_peri}} & \frac{\partial \phi_{11}}{\partial \mu_{a\_pros}} & \frac{\partial \phi_{11}}{\partial \mu_{a\_lesi}} & \frac{\partial \phi_{11}}{\partial \mu'_{s\_rect}} & \cdots & \cdots & \frac{\partial \phi_{11}}{\partial \mu'_{s\_lesi}} \\ \frac{\partial \phi_{12}}{\partial \mu_{a\_rect}} & \ddots & \ddots & \vdots & \vdots & \ddots & \ddots & \vdots \\ \vdots & \ddots & \ddots & \vdots & \vdots & \ddots & \ddots & \vdots \\ \frac{\partial \phi_{77}}{\partial \mu_{a\_rect}} & \cdots & \cdots & \frac{\partial \phi_{77}}{\partial \mu_{a\_lesi}} & \frac{\partial \phi_{77}}{\partial \mu'_{s\_rect}} & \cdots & \cdots & \frac{\partial \phi_{77}}{\partial \mu'_{s\_lesi}} \end{bmatrix} \tag{2.3}$$

where I_{ij} $(i, j = 1,2,...,7)$ and ϕ_{ij} $(i, j = 1,2,...,7)$ are the intensity and phase terms of $U(\vec{r}, \omega)$, respectively. In equ. (2.3), "rect", "peri", "pros", and "lesi" denote "rectum wall", "peri-prostate tissue", "prostate", and "prostate lesion" respectively.

The Levenberg-Marquart (LM) algorithm governs the iterative recovery of the optical properties by updating the ROI-specific values of μ_a and μ_s' according to

$$x_{k+1} = x_k + \alpha \cdot [J^T(x_k)J(x_k) + \lambda I]^{-1} J^T(x_k)\Delta v(x_k) \tag{2.4}$$

where x is the array of parameters to be optimized, J is the Jacobian matrix defined by equ. (2.3), Δv is the forward projection error, λ is a penalty or regularization term. A small damping factor α in the range of (0, 1) is introduced in equ. (2.4) to stabilize the convergence. It is shown in [48] that an α chosen empirically could make the LM algorithm more reliable and computationally more efficient.

2.2.3 TRUS *prior* assisted finite-element mesh for trans-rectal NIR tomography reconstruction

In this study the TRUS images available in open sources [37] are used. Utilizing the US *prior* to guide NIR tomography reconstruction could be performed by direct segmentation of the US image. Alternatively, as shown in [44] for breast imaging, the location and size of a suspected lesion can be derived from US images to directly generate a mesh that contains 2 ROIs to represent the lesion with a dense mesh and the background tissue with a coarse mesh. TRUS

information may be utilized in similar way, but trans-rectal imaging demands a mesh containing more ROIs that include at least the rectum wall, the peri-prostate tissue, the prostate, and the tumor within the prostate.

The TRUS image was first imported into a software 3ds-MAX [Autodesk Inc] (shown in Fig.2.2(a)). The 3ds-max provides very flexible geometry-deforming functions, with which a basic 3-D geometry of the prostate can be outlined manually. The finalized 3-D mesh of the prostate is converted to COMSOL Multiphysics [COMSOL AB] compatible format (shown in Fig.2.2(b)) with MeshToSolid [Syncode Inc]. The absorption and reduced scattering coefficients of rectum, peri-prostate tissue, and prostate in each individual ROI are assigned with the values suggested by literature [2]. A spherical shape is adopted for the prostate tumor. Fig.2.3 illustrates one example of the completed FEM-mesh of the imaging volume for trans-rectal optical tomography derived from a TRUS image. The imaging volume is $80\times80\times80$ mm^3 (lateral-medial $\times$ cranial-caudal $\times$ ventral-dorsal).

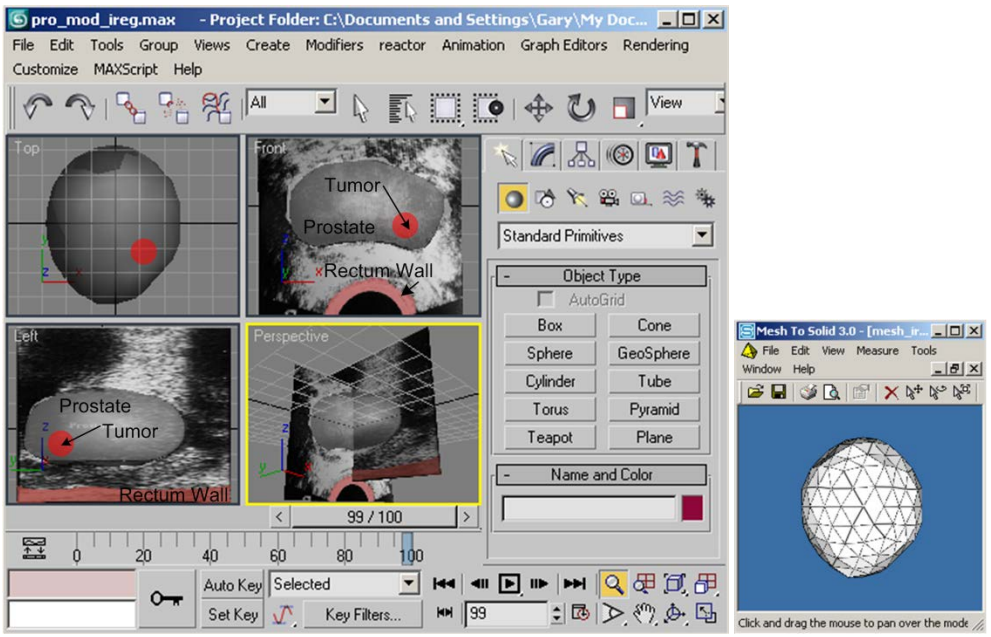

(a) (b)

Fig.2.2 Mesh Generation (a) 3ds-MAX Interface, (b) Mesh-to-Solid Interface

The Robin-type boundary condition defined in Equ. (2.2) is applied to all of the 6 surfaces among which only the rectum wall is a physical boundary. Since the dimensions, specifically the lateral-medial and ventral-dorsal ones, well exceed the potential volume of photon propagation for the NIR array given in Fig.2.1(c), treating the 5 surfaces other than the rectum wall as physical boundaries should have negligible effect upon the results.

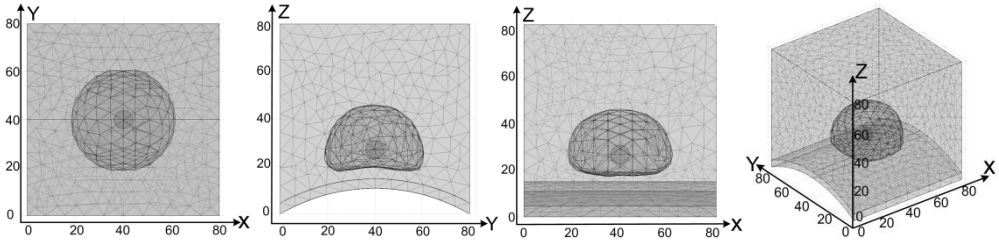

(a) Coronal View (b) Axial View (c) Sagittal View (d) Perspective View

Fig.2.3 FEM mesh of the imaging volume generated based on approaches in Fig.2.2.

The prostate in Fig.2.3 has a walnut shape of maximum dimensions of 50×50×30 mm^3. The rectum wall is 4mm thick and the curvature has a radius of 80mm. This radius is significantly

larger than what a rectum could have. However, when an NIR array wider than 20mm is applied to the rectum in addition to the cylindrical TRUS transducer, the local rectum lumen is likely to be transformed to have an elliptical cross-section. We have also found that setting a larger-radius to the rectum curvature gives more flexibility to the details of the posterior prostate region in the mesh. A larger rectum radius is therefore utilized. The completed mesh similar to that shown in Fig.2.3 contains approximately 4000 nodes and 20000 elements.

The source modulation frequency ω in equ. (2.1) has been set at 100MHz for all the simulations, and 1% Gaussian noise has been added to all forward calculations to form the measurement data. In all the figures presented, the unit of length is millimeter, x denotes the longitudinal coordinate in the range of [0, 80], y denotes the lateral coordinate in the range of [0, 80], and z denotes the depth coordinate in the range of [0, 80], as is shown in Fig.2.3.

2.3. A hierarchical spatial *prior* approach for trans-rectal NIR tomography reconstruction

2.3.1 Sensitivity of the sagittal trans-rectal NIR array

The NIR array proposed in Fig.2.1(c) has 7 source channels occupying one lateral line and 7 detection channels occupying the other line. The sensitivity of this imaging geometry with respect to a perturbation of the optical properties is determined by the corresponding Jacobian values in equ. (2.3). The sensitivity is calculated by projecting the Jacobian values along a line in the imaging volume. Figure 2.4 plots the sensitivity specific to absorption, or $\partial \ln I_{ij} / \partial \mu_a$, for a medium optical properties of $\mu_a = 0.01 mm^{-1}$ and $\mu_s^{'} = 1.0 mm^{-1}$. The Fig.2.4(a) is the longitudinal sensitivity in the mid-sagittal plane for a line from (0, 40, 30) to (80, 40, 30), Fig.2.4(b) is the lateral sensitivity in the mid-transverse plan for a line from (40, 0, 30) to (40, 80, 30), and Fig.2.4(c) is the depth sensitivity in the mid-sagittal plane for a line from (40, 40, 15.1) (here 15.1 is the z coordinate, but the actual depth from the rectum surface is 0mm owing to the curvature of the rectum) to (40, 40, 80), respectively. The dimension or the locations of the source &

detector array is marked on the abscissa of all three plots. The TRUS sagittal plane is located at y=40mm, which is the mid-sagittal plane within the NIR imaging volume.

Fig.2.4 indicates that the longitudinal sensitivity has ~6dB variation in the middle 75% range of the array, and the lateral sensitivity is peaked at the mid-saggital plane. In the middle-sagittal plane the sensitivity degrades at ~1dB/mm as z-coordinate increases from 20mm, which is apparently due to the side-way placement of the NIR array. This type of depth-degrading sensitivity will reconstruct a deeper target at a shallower position [41] if no spatial *prior* is incorporated.

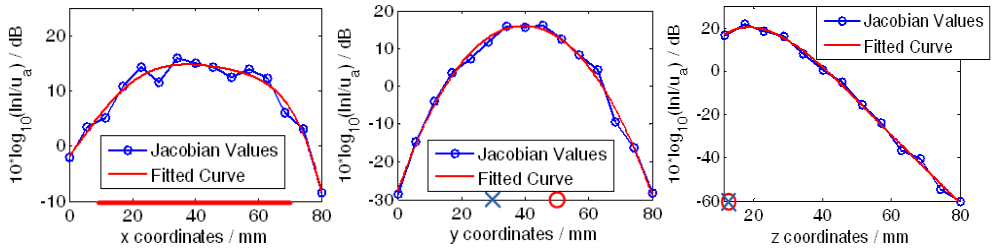

(a) (b) (c)

Fig.2.4 Sensitivity plots. (a) mid-sagittal plane, longitudinal sensitivity, (b) mid-transverse plane, lateral sensitivity. (c) mid-saggital plane, depth sensitivity. The marks on abscissa or the origin show the positions of optodes and x,y,z coordinates are denoted according to Fig.2.3.

2.3.2 Trans-rectal NIR image reconstruction without *a priori* information

The performance of recovering tumor target by trans-rectal NIR tomography is first examined without the structural *prior*. The accurate forward measurement is calculated by the TRUS-defined geometry as shown in Fig.2.3, and the iterative image reconstruction is conducted using mesh of homogenous element density throughout the entire volume. The optical properties of a 10mm diameter tumor target are $\mu_a = 0.02mm^{-1}$ and $\mu_s' = 1.6mm^{-1}$, with the parameters of other regions identical to those given in Fig.2.3 and listed in Table 2.1. Fig.2.5 lists the results for the tumor target being placed at left, middle, and right within the prostate. The top row in Fig.2.5

lists the μ_a and μ_s' target images used to calculate the forward data. The forward data is then reconstructed with meshes of no *prior* information to obtain the images listed at the bottom row. It is observed that without spatial *prior*, a tumor target may be localized, but with poor resolution in location and spatial content. The accuracy of optical property recovery is also poor. The lesions shown, which are recovered by NIR information only as no spatial *prior* information is utilized in the inverse computation, are difficult to interpret without a location correlation with TRUS. Further, we have found in simulation that a tumor with negative absorption contrast can hardly be recovered by trans-rectal NIR tomography alone without the spatial *prior*.

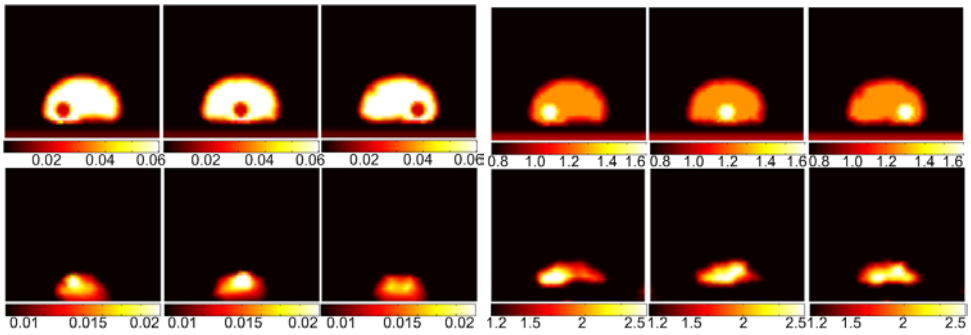

(a) (b)

Fig.2.5 NIR-only reconstruction of a tumor target in varied longitudinal locations

Row 1: target image for calculating the forward data; Row 2: Images reconstructed without any spatial *prior*. (a): μ_a (mm^{-1}) images; (b): μ_s' (mm^{-1}) images.

2.3.3 A hierarchical spatial *prior* method for TRUS guided trans-rectal NIR reconstruction

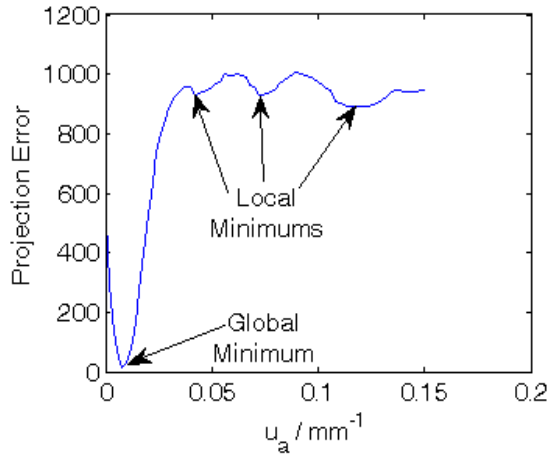

Fig.2.6 Local-minimum issue in reconstruction.

Note: The forward calculation is based on Fig.2.3(a) with assumption of homogeneous imaging volume. The projection error is calculated by using reduced scattering coefficient of the true value (0.008mm^{-1}), and using an absorption coefficient value from 0 to 0.15mm^{-1} at a step of 0.002mm^{-1}, with respect to the forward data. Other than the global minimum, three local minimums can be observed where the iteration can stop incorrectly. This is the effect of varying only one parameter. More local minimums may occur when reconstructing more parameters.

The tissue volume involved in trans-rectal prostate imaging constitutes nested-structures including a thin layer of rectum wall, a large volume of peri-prostate tissue, a relatively absorbing prostate, and the lesion within the prostate. These nested imaging domains may be further complicated by the pelvic bone that could interfere with the light propagation. Schweiger, et al. [49], Kolehmainen et al., [50-52], and Srinivasan et al. [53] investigated the issue of recovering the shapes and optical properties of regions with optical contrast inside a non-nested or nested domains, where the shapes of the ROIs were derived from optical information when no spatial *prior* is obtained from other complementary imaging modalities. The methods showed sufficient robustness in recovering the shapes and optical properties of the ROIs, yet the problem of

stability and/or slow convergence was noticed in those approaches dealing with nested-domains. In our approach of coupling trans-rectal NIR with TRUS, the shapes of the ROIs for trans-rectal optical tomography reconstruction could be defined directly from TRUS. The simplest approach of implementing the TRUS *a priori* information could be assigning homogenous optical properties within each ROIs of the imaging domain. However the convergence and the accuracy of reconstruction are still dependent upon the initial guess. This can be attributed to the gradient based solver for which the local minimum feature [48] would likely be exaggerated in prostate imaging in which the multiple combinations of optical properties of the nested-structures in the imaging volume may have multiple combinations of optical properties fitting the measurements. There are also disagreements regarding the optical contrast of prostate tumor, namely positive or negative. All these features together challenge the accuracy and robustness of image reconstruction in trans-rectal optical tomography wherein finding the global minimum for the iterations to converge is particularly intriguing as indicated in Fig.2.6. The local-minimum problem makes the reconstruction sensitive to the initial guess of optical properties.

When TRUS *prior* is available, a conventional way of utilizing the TRUS spatial information would be the "hard" *a priori* method in which the optical properties of each ROIs are set homogenous and updated simultaneously at each iteration. However, we have found that this conventional approach may not lead to reliable convergence for prostate imaging, which is believed to be due to the local-minimum problem. One example is given in Table 2.1 for the NIR array shown in Fig.2.1(c). The prostate model is generated according to a previous work [2] (the details are given in the later text and Fig.2.8(c)), and a target of 10mm in diameter is located at a coordinate setting of (40, 50, 15) that is 15 mm from the rectal surface. When the four ROIs including the rectum, the peri-prostate tissue, the prostate, and the prostate tumor are updated simultaneously from the same initial guess of μ_a =0.01mm^{-1} and μ_s' =1.0mm^{-1}, the iteration stops

after 1 round due to the negative μ_a value obtained for the rectum wall. The iteration fails to continue due to the local minimum issue.

Table 2.1 Results of simultaneously updating the 4 ROIs from the same initial guess

	μ_a (mm^{-1})				μ_s' (mm^{-1})			
Regions	Surrounding Tissue	Rectum Wall	Prostate	Tumor	Surrounding Tissue	Rectum Wall	Prostate	Tumor
Set value	0.002	0.01	0.06	0.02	0.8	1	1.27	1.6
Simultaneous Update	0.1216	**-0.008**	0.026	0.0215	1.1482	2.3602	0.6173	0.7073

The local minimum problem may be mitigated by a cascaded initial-guess approach or a hierarchical spatial *prior* method. This hierarchical spatial *prior* method may allow steady and global convergence of the iteration. The fundamental idea of this method is to first reconstruct the global optical properties of the entire volume, then to reconstruct the optical properties of prostate and rectum wall, and last to reconstruct the tumor lesion area. The 2nd and 3rd steps use the value obtained in the previous step as the initial guess of that specific ROI. Therefore at each step, the perturbation by a relatively smaller region is less influential and convergence of iteration is better warranted. The detailed steps are shown in Fig.2.7 and described in below:

(a) The first iterations assume an entirely homogenous imaging volume. In this round the initial projection errors will be large and the converging process is most likely to be affected by the global minimum. Therefore, a single set of optimum values of μ_a and μ_s' are determined with LM algorithm and will be used as the initial guess in the second step.

(b) The second iterations consider three regions of rectum wall, peri-prostate tissue, and prostate within the imaging volume. The iterations of optical properties of these three ROIs start at the same initial guess provided in step (a) and converge at different values.

(c) The values obtained from step (b) are used as the initial guess for the same three ROIs but with a tumor added to the prostate. The tumor and the prostate take the same initial values resulted from the previous step. Now each of the four ROIs (rectum wall, peri-prostate tissue, prostate, and tumor) converges to different end values.

The change of the overall projection error for the three steps is plotted in Fig.2.7(d). Rapid and reliable convergence is observed. The hierarchy of the implementation of initial values for iteration is illustrated alternatively in Fig.2.7(e).

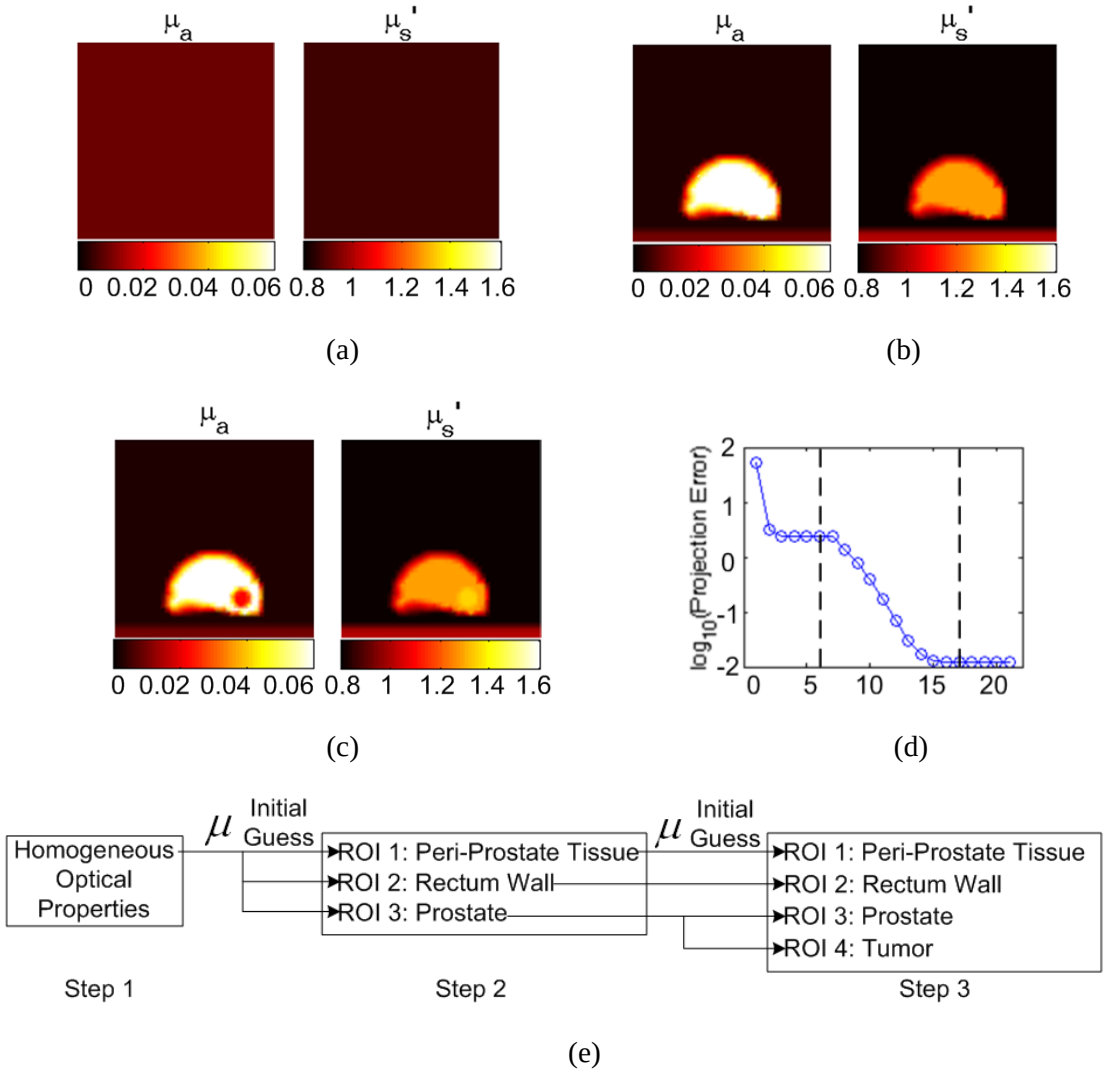

Fig.2.7. The 3-step hierarchical reconstruction method.

(a) step 1—one ROI for the entire volume; (b) step 2—three ROIs representing rectum wall, peri-prostate tissue, prostate; (c) step 3—four ROIs representing rectum wall, peri-prostate tissue, prostate, tumor; (d) change of the overall projection error, where the dash lines separate the converging of the three steps in

(a)—(c); (e) block chart of the hierarchical initial guess assignment. Note: units of colorbars: mm^{-1}

2.3.4 Evaluation of the hierarchical spatial *prior* method against literature-given results

Recently Li et al. reported simulation results for trans-rectal optical tomography reconstruction in the context of using MRI anatomic information [2]. Their work is referred as "NIR/MRI" in the following text. We have tested the performance of our hierarchical spatial *prior* method using the probe geometry and the optical properties presented in the NIR/MRI work. In the NIR/MRI work, the trans-rectal NIR probe is stand-alone from MRI, thereby the NIR optodes could occupy the entire surface region of the planar probe. The size and depth of the tumor for simulation were not specified in the NIR/MRI work, but our incorporation of a diameter of 10 mm and a depth of 15mm from the planar probe surface is considerably close to the one presented. The challenge of local minimum is also indicated in the NIR/MRI work. The authors set an arbitrary searching range for the optical properties (μ_a:0-0.1 mm^{-1}, μ_s':0-2 mm^{-1}), and in 4 sets of the results, 3 of the tumor μ_a values reached the limits thereby were stopped from further iteration, whereas the 4th value converged at a number more than 2 folds of the set value.

The NIR/MRI work reconstructed the optical properties of entire regions simultaneously. Since our hierarchical spatial *prior* approach is more robust in avoiding the local minimum problem, it is expected that the hierarchical method will even-perform or outperform the NIR/MRI one. In the NIR/MRI work, the best result is deducted when 10 sources and 28 detectors are employed. Therefore the hierarchical method is tested using the same probe geometry that is re-plotted in Fig.2.8. The reconstruction is also preformed in transverse-view as the NIR/MRI work did. The noise added to the forward solution is 1% in both methods.

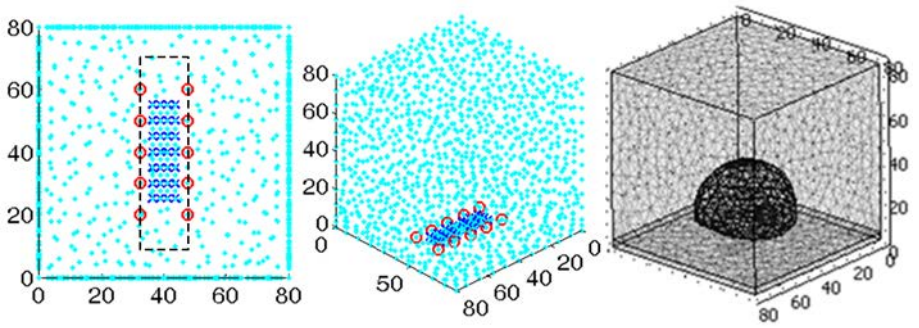

(a) (b) (c)

Fig.2.8 The FEM mesh generated by following the geometry in NIR/MRI paper. (a) the geometry of the optodes, where the dash rectangle delineates the dimension of the NIR array that will be evaluated later for integration with US; (b) the 3-d view of the optodes and the imaging volume; (c) FEM containing the prostate and the tumor.

The parameters used are identical to those in Table 2.1., Table 2.2 lists the results of the hierarchical method in comparison with those given in NIR/MRI paper. It is observed that the hierarchical method (listed as "3-step" in the table), as expected, slightly outperforms the NIR/MRI method in terms of the accuracy of recovering optical properties. The results of recovering a target of positive absorption contrast are listed in Table 2.3 using the NIR/MRI probe geometry and our 3-step method. Since NIR/MRI paper did not present results for the case of target with positive absorption contrast, only the 3-step method is presented in Table 2.3 for comparison with the set values. In Table 2.3 the absorption coefficient of prostate is set much lower than that in Table 2.2 but the tumor optical properties are kept the same as those in Table 2.2. If the absorption of prostate in Table 2.3 is kept the same as in Table 2.2, the positive absorption target can hardly be reconstructed. The choice of lower prostate absorption is for testing our hierarchical method, but it does not necessarily disagree with the actual value of prostate absorption. As a matter of fact, the absorption properties of prostate has shown large variation in literatures [34-37] where the measurement are either taken from *in vitro* tissue or may

be interfered by bleeding of *in vivo* tissue under invasive measurement. The absorption coefficient of intact prostate is not available so far, and if available, is likely lower than the values reported in literatures for non-intact prostate.

Table 2.2 Reconstruction of prostate tumor of negative contrast with respect to the prostate

	μ_a (mm^{-1})				μ_s' (mm^{-1})			
Regions	Surrounding Tissue	Rectum Wall	Prostate	Tumor	Surrounding Tissue	Rectum Wall	Prostate	Tumor
Set value	0.002	0.01	0.06	0.02	0.8	1	1.27	1.6
NIR/MRI	0.0025	0.01	0.0575	0.0448	0.8324	1	1.339	1.075
3-step	0.002	0.0099	0.06	0.0208	0.8012	1.0028	1.2824	1.3495

Table 2.3 Reconstruction of prostate tumor of positive contrast with respect to the prostate

	μ_a (mm^{-1})				μ_s' (mm^{-1})			
Regions	Surrounding Tissue	Rectum Wall	Prostate	Tumor	Surrounding Tissue	Rectum Wall	Prostate	Tumor
Set value	0.002	0.01	0.006	0.02	0.8	1	1.27	1.6
3-step	0.0020	0.0100	0.0061	0.0163	0.7998	0.9997	1.2863	1.2434

The reconstructed images for both negative and positive contrasts are listed in Fig.2.9. These results demonstrate the capability of our hierarchical spatial *prior* method in reconstructing prostate lesion with either negative or positive absorption contrast.

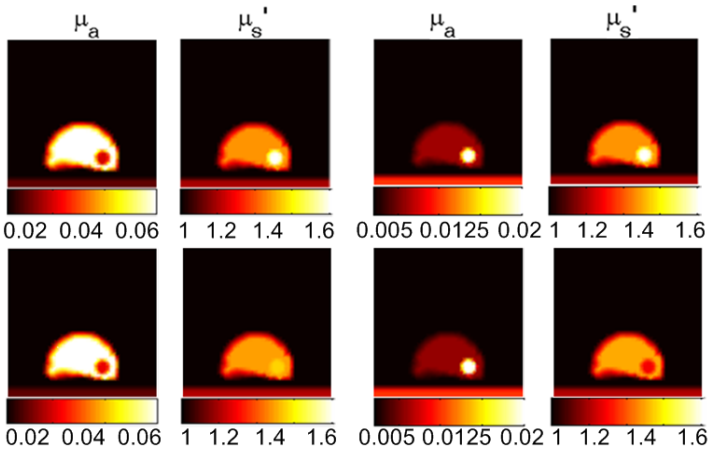

(a) (b)

Fig.2.9 Reconstructed images for a target with absorption contrast.

Top row: forward model; Bottom row: reconstruction images. (a) negative contrast (b) positive contrast. Note: units of colorbars: mm^{-1}

2.4 Assessment of NIR applicator designs for coupling NIR with TRUS

It has been previously stated that the dual-line NIR array geometry is feasible for concurrent NIR/TRUS imaging considering the space limitation for coupling with TRUS transducer and the requirement of endo-rectal insertion. Based on fabrication reality, we have also suggested that each line array consist of 7 channels. The 7 channels on each line array could be all for source or detector as shown in Fig.2.10(a), or for interspersed source/detector as in Fig.2.10(b). If the difficulty of fabrication or insertion is overlooked, there are certainly a number of NIR geometries that can be coupled to TRUS sagittal transducer. Compared with the one in Fig.2.10(a), more channels could be added to each line-array as shown in Fig.2.10(f), more numbers of lines can be added as shown in Fig.2.10(c), or more lines and more channels added as in Fig.2.10(h). More options are also listed in Fig.2.10.

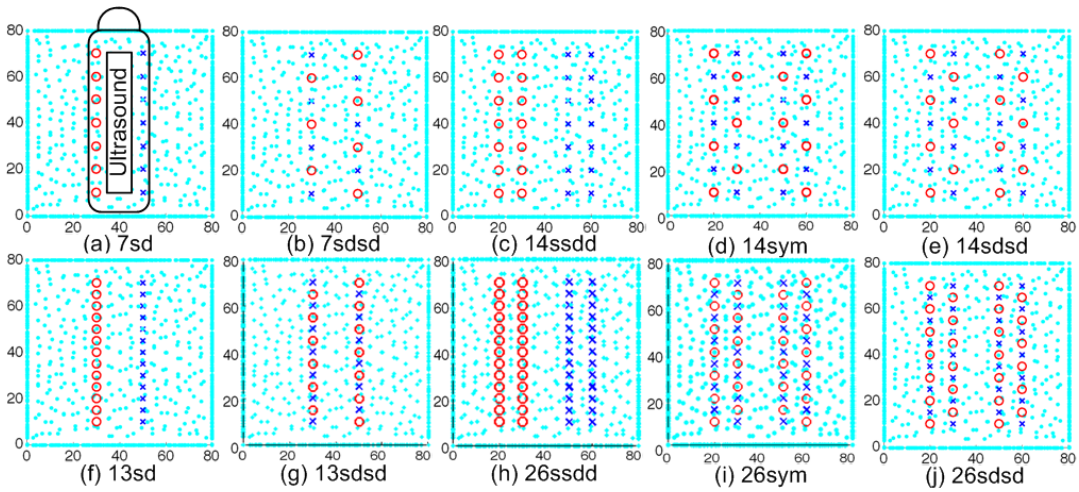

Fig.2.10 NIR array designs

The dimension of the sagittal TRUS transducer window is shown in (a). The number of the Fig. caption denotes the amount of channels in each lateral side of the sagittal TRUS transducer as is depicted in (a). “sd” denotes one line of source array and one line of detector array. “ssdd” denotes two lines of source arrays and two lines of detector array. “sdsd” denotes mixed source/detector channels in one line. “sym” denotes symmetric distribution of the optodes with respect to the sagittal TRUS transducer.

The geometry of (a) is the most desirable one in terms of fabrication easiness and endo-rectal applicability. The designs in (a), (b), (f) and (g) correspond to an NIR probe with a minimum lateral dimension of 20mm. The designs in (c)-(e) and (h-j) correspond to NIR probe with a minimum 40mm lateral dimension which is not suitable for endo-rectal use. The geometries in (a)—(e) represent a 10mm spacing between the closest optodes, and the geometries in (f)—(j) require a 5mm spacing between the closest optodes. The smaller spacing in (f)—(j) will be challenging for fabrication considering the number of fiber channels and the side-firing configuration if the probe is to be integrated to TRUS probe unless the internal structural of the TRUS probe can be altered.

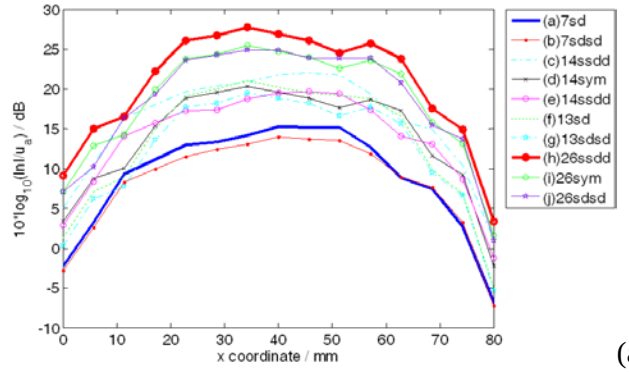

(a)

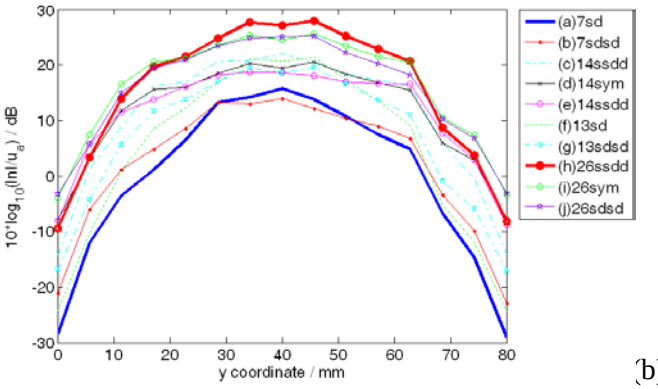

(b)

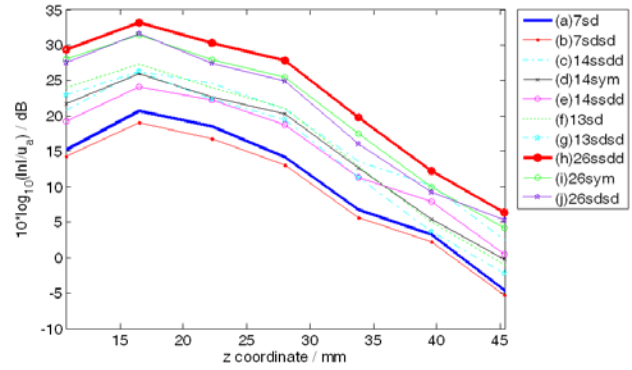

(c)

Fig.2.11 Sensitivity comparison

(a) longitudinal direction, (b) lateral direction, (c) depth direction. The upper thicker line correspond to the configuration (h) in Fig.2.10, and the lower thicker line correspond to the desired configuration (a) in Fig.2.10.

2.4.1 Sensitivity comparison

It is known that more optodes lead to better NIR imaging performance [54]. The sensitivities of all the 10 configurations of Fig.2.10 are compared in Fig.2.11. The mesh in Fig.2.3

with homogeneous optical properties ($\mu_a = 0.01mm^{-1}$ and $\mu_s^{'} = 1.0mm^{-1}$) is used for the sensitivity calculation. Fig.2.11 evaluated the sensitivity at the lines identical to those in Fig.2.4. Again only the absorption sensitivity which is the $\partial \ln I_{ij} / \partial \mu_a$ part of the Jacobian values is evaluated.

Several observations could be made from Fig.2.11: (1) increasing the spatial dimension of source-detector array generally improves the sensitivity; (2) increasing the number of source-detector pairs generally improves the sensitivity; (3) interspersed source-detector layout may have slightly wider lateral sensitivity but is not necessarily better than non-dispersed source-detector layout for other imaging views; (4) the geometry of 26ssdd (the upper thicker line) does have the best sensitivity feature among the 10 geometries, therefore it can be used as a reference to evaluate the simple geometry of 7sd (the lower thicker line).

2.4.2 Comparison between the 7sd design and the 26ssdd design

The 7sd design represents an array less challenging in fabrication and more practical for endo-rectal use. The 26ssdd geometry is impractical for endo-rectal application, difficult to fabricate, but has the best performance among the designs listed. It is shown in Fig.2.11 that the sensitivity of 7sd design is approximately 10dB less than that of 26ssdd in the specified longitudinal, lateral, and depth directions. The lack of sensitivity in 7sd design must affect the accuracy of reconstruction, but to what extent is unknown. Performance on reconstruction is thus compared between these two geometries for representative target variations. The optical properties listed in Table 2.2 (set values) are used for the following simulations.

2.4.2.1 Reconstruction accuracy versus target longitudinal location

A target with 10mm diameter is placed at the middle-sagittal plane of y=40mm, z=26mm, and varied in longitudinal coordinates from x=25 to 55mm with a step of 5mm, as is shown in Fig.2.12 (a). The optical properties reconstructed by the two geometries are compared with respect to the true values in Fig.2.12 (b) and (c). It is observed that the optical properties

recovered by 26ssdd and 7sd designs are close to each other at most of the longitudinal locations, but the 7sd design showed large variation in the recovered absorption contrast at x=30mm and x=50mm compared to other positions. This large variation may be related to fewer source-detector pairs that contribute to the target detection when close to the boundary or the existence of any "jittering" elements in the mesh for reconstruction.

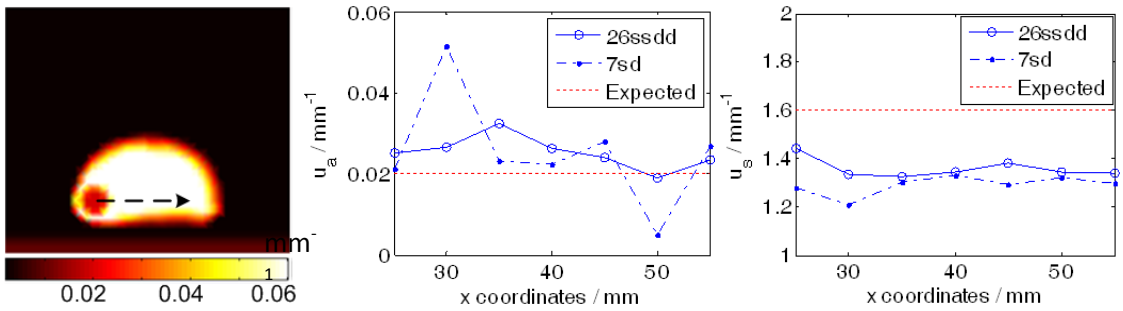

(a) (b) (c)

Fig.2.12 Comparison of two geometries for a target varying in longitudinal location in the middle-sagittal plane: (a) illustration of the target location change; (b) comparison of absorption coefficient reconstruction; (c) comparison of reduced scattering coefficient reconstruction

2.4.2.2 Reconstruction accuracy versus target depth

A target with 10mm diameter is placed at the middle-sagittal plane at x=40mm, y=40mm, and the depth is varying from z=25 to 40mm at a step of 2.5mm (the last data point is simulated at z=39mm, because at 40mm, the target is out of the prostate), as is shown in Fig.2.13(a). The reconstructed optical properties are compared in Fig.2.13(b) and (c). The 26ssdd configuration outperforms the 7sd one again. However, beyond z=30mm, both designs are incapable of recovering the absorption coefficient of the target from the prostate background. This depth limitation is related to the maximum span of the NIR array, the absorption coefficient of the prostate, and the size of the target. For a larger target such as a diameter of 14mm, it is verified that the target may be resolved up to 36mm from the NIR array in comparison to 30mm for the

same NIR array span and prostate absorption coefficient. A potentially smaller absorption coefficient of intact prostate will also increase the depth limit of target detection.

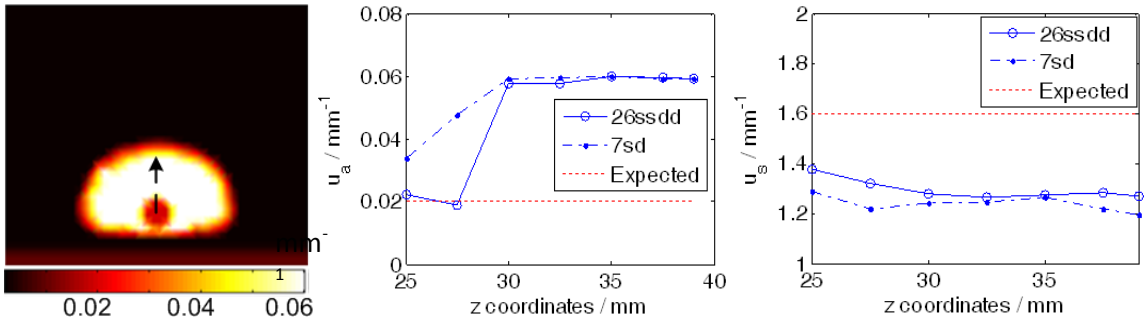

(a) (b) (c)

Fig.2.13 Comparison of two geometries for a target varying in depth in the middle-sagittal plane: (a) illustration of the target location change; (b) comparison of absorption coefficient reconstruction; (c) comparison of reduced scattering coefficient reconstruction

2.4.2.3 Reconstruction accuracy versus target size

Target at middle-sagittal plane of x=40mm, y=40mm and z=26mm is simulated for a diameter from 4mm to 14mm with a step of 1mm. The target diameter change is illustrated in Fig.2.14(a). The reconstructed optical properties are compared in Fig.2.14(b) and (c). It is clear that the larger the target, the better the accuracy of reconstruction. The 26ssdd can recover the absorption contrast of the target when the diameter is greater than 6mm and the 7sd can recover the target for target diameter greater than 8mm.

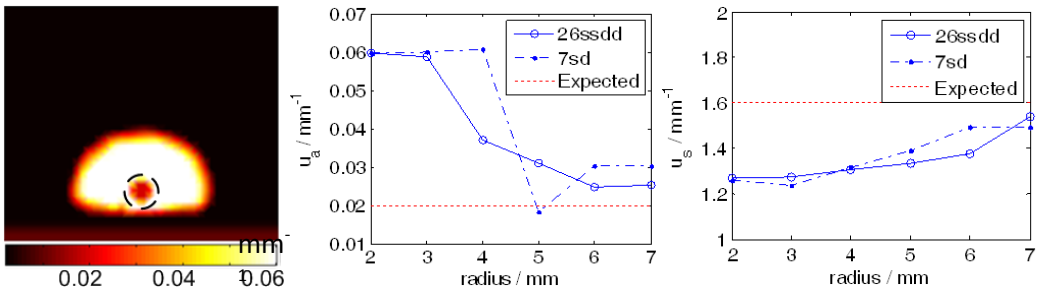

(a) (b) (c)

Fig.2.14 Comparison of two geometries for a target varying in size in the middle-sagittal plane: (a) illustration of the target size change; (b) comparison of absorption coefficient reconstruction; (c) comparison of reduced scattering coefficient reconstruction

These comparisons do suggest that the 7sd design is inferior to the 26ssdd design, especially for the reconstruction of absorption properties. However, the accuracy of reconstructing scattering properties by the 7sd design is close to that of 26ssdd. With all the previously discussed challenges in trans-rectal NIR probing for coupling with TRUS, it is fair to consider the 7sd design as a working geometry.

2.4.3 Capability of recovering two targets by the 7sd design in sagittal plane

Capability of differentiating two targets is of particular relevance to prostate cancer imaging owing to the frequent existence of secondary or multifocal tumors [55-56]. The multiple lesions may fall into the same TRUS field-of-view (FOV), or one falls outside the TRUS FOV. For the former cases, the US *prior* serves as the guidance for NIR reconstruction. For the latter case NIR may actually be able to interrogate the out-of-plane target owing to its 3-D imaging capability. However, the location information of NIR reconstruction of the target will apparently not be reliable. Nevertheless the out-of-plane target suggested by NIR may actually help to redirect the US to the plane containing the target for further clarification. Thus, the two imaging modalities may actually complement each other for multi-lesion cases. In this section, however, we investigate only the former cases of two targets residing in the same sagittal plane. This

requires implementing the multi-target location information in the last step of the hierarchical spatial *prior* routine. The following simulations are conducted with the 7sd probe design only.

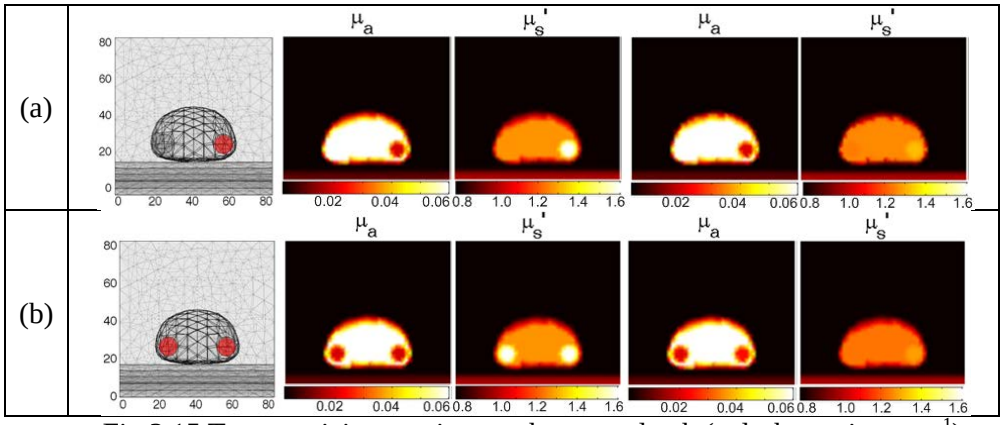

Fig.2.15 Two suspicious regions at the same depth (colorbar units: mm^{-1})

2.4.3.1 Reconstruction of two targets located at the same depth within the sagittal plane

As is shown in Fig.2.15, two 10mm-diameter regions are added to the prostate, with coordinates (25, 40, 26) and (55, 40, 26), respectively. In Fig.2.15(a) only one region is assigned true optical contrast, and in Fig.2.15(b) both regions have true optical contrast. In both cases the optical contrast can be reconstructed with good accuracy, as is shown in Table 2.4. Accuracy of the reconstructed μ_a values for the target with true optical contrast is within ±20% of the set values and the μ_s' values can be reconstructed within ±23% of the set values. There are some artifact reconstructed for the target with no true optical contrast, nevertheless, the target with true optical contrast can be easily differentiated from the other one.

Table 2.4 Comparison of reconstructed optical properties(mm^{-1}) in Fig.2.15

μ_a(mm^{-1})						
Fig.	Regions	Peri-prostate	Rectum	Prostate	Target 1	Target 2
(a)	Set value	0.002	0.01	0.06	0.06	0.02
	Reconstructed	0.002	0.0101	0.0601	0.0778	0.0208
(b)	Set value	0.002	0.01	0.06	0.02	0.02
	Reconstructed	0.002	0.01	0.0597	0.0207	0.024
μ_s' (mm^{-1})						
Fig.	Regions	Peri-prostate	Rectum	Prostate	Target 1	Target 2
(a)	Set value	0.8	1.0	1.27	1.27	1.6
	Reconstructed	0.7995	0.9935	1.261	1.2187	1.3216
(b)	Set value	0.8	1.0	1.27	1.6	1.6
	Reconstructed	0.8007	0.9953	1.2343	1.2302	1.2837

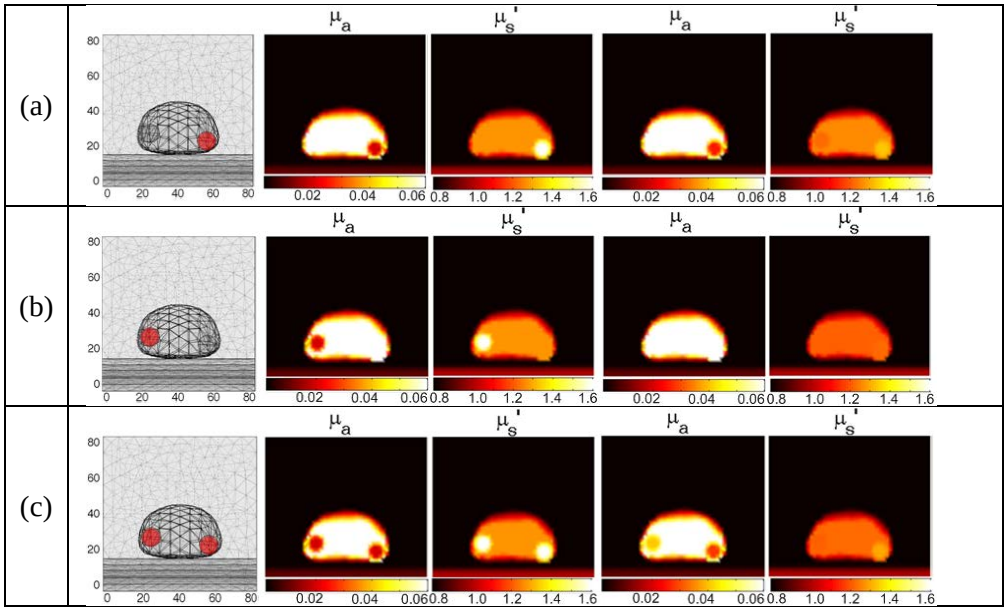

Fig.2.16 Two targets at different depths: negative contrast cases (colorbar units: mm^{-1})

Table 2.5 Comparison of reconstructed optical properties (mm^{-1}) in Fig.2.16

μ_a (mm^{-1})						
Fig.	Regions	Peri-prostate	Rectum	Prostate	Region 1	Region 2
(a)	Set value	0.002	0.01	0.06	0.06	0.02
	Reconstructed	0.002	0.01	0.0594	0.0674	0.0252
(b)	Set value	0.002	0.01	0.06	0.02	0.06
	Reconstructed	0.002	0.0101	0.0597	0.0592	0.0607
(c)	Set value	0.002	0.01	0.06	0.02	0.02
	Reconstructed	0.002	0.01	0.0596	0.0402	0.0276
μ_s' (mm^{-1})						
Fig.	Regions	Peri-prostate	Rectum	Prostate	Region 1	Region 2
(a)	Set value	0.8	1.0	1.27	1.27	1.6
	Reconstructed	0.8009	0.9977	1.2538	1.2167	1.3286
(b)	Set value	0.8	1.0	1.27	1.6	1.27
	Reconstructed	0.8015	0.9931	1.2102	1.2179	1.2083
(c)	Set value	0.8	1.0	1.27	1.6	1.6
	Reconstructed	0.8015	0.9956	1.2177	1.2024	1.2962

2.4.3.2 Reconstruction of two targets located at different depth within the sagittal view

Two regions at different depthes are also simulated. The two targets of 10mm diameter are located at coordinates of (25, 40, 28) and (55, 40, 24), respectively. Reconstruction results are displayed in Fig.2.16 and Table 2.5 for target of negative absorptin contrast.

For the target at the depth of 24mm, the μ_a and μ_s' can be reconstructed within ±20% and ±25% of the set values, respectively. However, the target at 28mm depth cannot be reconstructed. This must be related to the high absorption coefficient of $0.06mm^{-1}$ set to the prostate. When the prostate absoption is set at a reduced value of $0.006mm^{-1}$ and positive optical contrast is set in the two target regions, both tartgets can be recovered as shown in Fig.2.17 and Table 2.6. For the cases of target with positive absorption contrast, the μ_a of the target can be reconstructed within ±5% of the set value, while the μ_s' is still reconstructed within ±23% of the expected values.

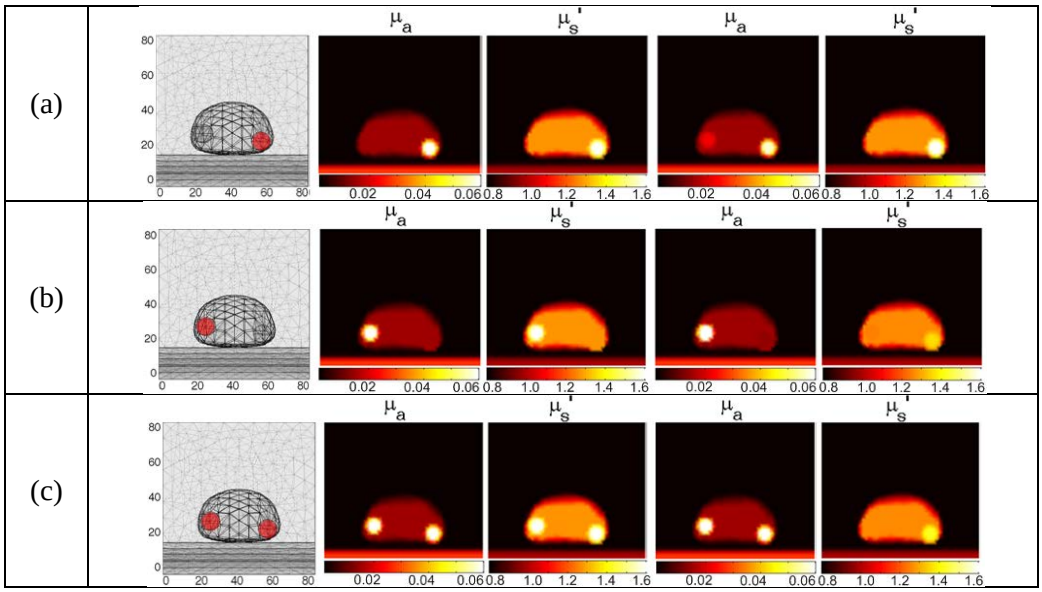

Fig.2.17 Two targets at different depths: positive contrast cases (colorbar units: mm^{-1})

Table 2.6 Comparison of reconstructed optical properties (mm^{-1}) in Fig.2.17

$\mu_a(mm^{-1})$						
Fig.	Regions	Peri-prostate	Rectum	Prostate	Region 1	Region 2
(a)	Set value	0.002	0.01	0.006	0.006	0.02
	Reconstructed	0.002	0.0101	0.006	0.0083	0.0191
(b)	Set value	0.002	0.01	0.006	0.02	0.006
	Reconstructed	0.002	0.0101	0.006	0.0116	0.0058
(c)	Set value	0.002	0.01	0.006	0.02	0.02
	Reconstructed	0.002	0.0099	0.006	0.0208	0.0199
$\mu_s'(mm^{-1})$						
Fig.	Regions	Peri-prostate	Rectum	Prostate	Region 1	Region 2
(a)	Set value	0.8	1.0	1.27	1.27	1.6
	Reconstructed	0.7993	0.9934	1.2637	1.2689	1.6722
(b)	Set value	0.8	1.0	1.27	1.6	1.27
	Reconstructed	0.8008	0.993	1.259	1.2402	1.3586
(c)	Set value	0.8	1.0	1.27	1.6	1.6
	Reconstructed	0.8049	0.9979	1.2576	1.2538	1.424

2.5. Discussions

The purpose of this work is to investigate the feasibility of trans-rectal NIR tomography of the prostate in the context of coupling with sagittal TRUS for concurrent trans-rectal NIR/US imaging. There is considerable interest emerging recently on trans-rectal NIR tomography to

augment existing imaging modalities, but such promise would not be validated or fulfilled without an applicator that can be inserted rectally and thereby imaged trans-rectally. With a trans-rectally applicable probe, trans-rectal NIR tomography can be obtained stand-alone. However, the resulted images would be difficult to correlate with the anatomy. Without a position coupling with a real-time anatomic imaging modality such as TRUS, the actual position of the NIR probe will be unknown due to the disadvantage features of NIR tomography. Fixing the NIR applicator with TRUS would provide accurate positioning information that can be used for localization and guided image reconstruction of trans-rectal NIR tomography. There could be a variety of NIR array designs for coupling with TRUS; however, the rectal application as well as the fabrication difficulty will determine the choices on the probe dimensions and number of channels for NIR optodes.

The utilization of a hierarchical spatial *prior* is under the condition that the anatomic information of the prostate tumor is explicit from TRUS. The prostate boundary is well-delineated in TRUS, and the spatial extent of a tumor can be defined if it is shown as hypo-echoic on TRUS. This is when the NIR functional contrast can help determine whether a tissue suspicious on US is malignant or not [45]. However, since as many as 40% of the tumors may be shown as iso-echoic on TRUS, the utility or accuracy of this hierarchical imaging approach is hindered when TRUS images do not specify a suspicious region, or when it is difficult to define the spatial extent of a suspicion region in TRUS. Under these circumstances, the third step of recovering the tumor lesion in the prostate may proceed by reconstructing the optical properties on every element within the prostate instead of treating the prostate as homogenous other than an inclusion that is also treated as homogenous in the simulation. Such approach is proven effective based on our other investigations, but the accuracy and robustness may be affected by the depth-dependent sensitivity. More dedicated investigations are needed in the future along with the experimental validations of this combined trans-rectal NIR/US approach. Prostate trans-rectal optical imaging is a relatively new area where the initial approach should focus on characterizing

the lesions most suspicious to TRUS. Trans-rectal NIR imaging of the lesions marginally suspicious to TRUS or non-suspicious to TRUS is apparently more challenging and should be preceded by trans-rectal NIR/US characterization of a lesion suspicious to US.

The presented simulations are largely based on setting the absorption properties of prostate at a high level of $0.06mm^{-1}$. This is significantly larger than that of breast tissue, and it is this parameter that dominates the detection depth of trans-rectal NIR tomography for the given geometry of NIR array. Recent studies indicate that better measurement condition may lead to a lower absorption value of prostate [37]. If in the future the measurement of intact prostate can be facilitated by trans-rectal optical tomography, an even lower absorption coefficient of the prostate may be obtained by suppression of any invasive interference. A lower absorption coefficient will certainly lead to detection of deeper target for the same NIR array geometry. The successful development and application of TRUS-coupled trans-rectal NIR tomography may not only help characterize lesions suspicious to TRUS, but also help answer the basic questions of optical properties of intact prostate.

2.6 Summary

The feasibility of obtaining trans-rectal optical tomography of prostate when coupling with TRUS is investigated by simulation. The trans-rectal NIR applicator has the geometry requirements of integrating with a commercial TRUS transducer for operation in the rectal lumen. We first developed a hierarchical iteration method for incorporation of TRUS spatial *prior* into trans-rectal optical tomography reconstruction. This method is based on a cascaded initial-guess approach to deal with local minimum problems common to near-infrared optical tomography reconstruction and is shown to render more reliable recovery of tissue optical properties for trans-rectal optical tomography. This reconstruction method is then utilized to evaluate a number of designs of near-infrared imaging applicator for integration with a sagittal TRUS transducer. The simulations suggested a working NIR imaging geometry that is feasible in terms of the dimension for rectal insertion and the easiness for fabrication. This design contains single line of optode on

each lateral side of the sagittal TRUS transducer, with 20mm lateral separation between the two line arrays and 10 mm longitudinal spacing among the total 7 channels on each line-array. The performance of this simple NIR array design is evaluated for the recovery of single lesion in prostate by comparison with a more accurate and much complicated design that is virtually impractical for trans-rectal use. The simple design is also evaluated for the recovery of two targets in the prostate. Results suggest the feasibility of integrating this simple NIR array geometry to TRUS for trans-rectal imaging of the prostate.

The experimental validation of this study[5] presents the instrumentation of a TRUS-coupled NIR array and demonstrates trans-rectal optical tomography of prostate by the combined trans-rectal NIR/US applicator. The trans-rectal NIR array has incorporated the design suggested by Fig.2.10(a). Concurrent trans-rectal imaging is acquired in the same sagittal plane by both US and NIR optical tomography. The real-time TRUS is used for accurate positioning of the trans-rectal NIR applicator and for guided NIR image reconstruction with the spatial *a priori* information. Tests on phantoms and tissues using the combined NIR/US imager demonstrate that absorption contrast may be recovered by NIR imaging only but with improved accuracy when the TRUS spatial *prior* is incorporated. Trans-rectal imaging of a healthy canine prostate *in situ* administered with tissue contrast validates the rectal applicability of the combined trans-rectal NIR/US probe as well as the method of TRUS guided trans-rectal NIR image reconstruction.

CHAPTER III

PARAMETRIC RECOVERY UNCERTAINTY LEVEL IN NEAR INFRARED DIFFUSE OPTICAL TOMOGRAPHY

3.1 Introduction

Diffuse optical tomography (DOT) based on measurement of near-infrared (NIR) light diffused through thick biological tissue aims to quantify the heterogeneities of NIR absorbing chromophors and scattering particles [57]. There are generally three categories of DOT measurements: (1) continuous-wave wherein only the steady-state or direct-current (DC) detection is carried out; (2) time-domain wherein the attenuation and pulse-width broadening of the excitation light are the measurands [58-61]; and (3) frequency-domain which is mathematically the Fourier-transform equivalent of the time-domain method [8, 31, 45, 62-70] but is considerably less complicated in instrumentation. The frequency-domain detection ideally renders three types of information: the DC attenuation, the modulation intensity change (AC) and the modulation phase shift (PHS). Some frequency-domain DOT works, however, have utilized the AC and PHS, rather than the complete measurands of DC, AC and PHS. Excluding the DC in frequency-domain DOT reconstruction implied that the DC information was considered unlikely to improve the outcome of reconstruction when the AC and PHS are available. Such consideration could have been prompted if the DC information had been redundant in frequency-domain reconstruction, but indeed it has not been either justified or negated.

On the other hand, many works in DOT have relied on only the DC measurements [5, 71-78]. Although lacking phase information will certainly reduce the accuracy or confidence of quantitative reconstruction, almost all these studies have demonstrated that the absorption and reduced scattering characteristics can be separately and absolutely reconstructed by use of DC information only. But all these works lack a direct comparison of the outcome of DC-based reconstruction with that of frequency-domain reconstruction, which is needed to provide a basis to assess the compromise for reconstruction based solely upon DC information. Out of these DC-based DOT reconstructions, there also exists a common but not widely-stated feature in the images---------the recovered background is usually more homogeneous than the general level of background artifacts seen in images reconstructed in frequency-domain. Less image artifacts in the background may be beneficial for identifying target-of-interest over a relatively heterogeneous background, but what contributes to the less image artifacts in the background has not been well-understood.

This work studies the level of artifacts associated with measurement-uncertainties in three modes of image reconstruction, namely DC, AC+PHS, and DC+AC+PHS. The studies are conducted both analytically and by synthetic measurements, to address why the DC-based reconstruction results in lower background artifacts and to demonstrate that including DC information in frequency-domain generally improves the reconstruction outcome. Clearly the analysis of this study shall be based upon the propagation of measurement noises to the image. Contributing to the image artifacts are a number of noise sources, among which is an error due to coupling loss as studied by Schweiger et al [79]. That study treated coupling errors as coupling coefficients appended to the solution space, and demonstrated reconstruction of frequency-domain data contaminated with synthetic coupling errors. Similar studies are necessary to understanding reconstruction with contaminated DC data.

The level of artifacts is a critical indicator of the capability of reliably recovering the optical heterogeneity. Ntziachristos et al. [80] demonstrated that the reconstruction of localized

lesions deteriorated as a function of background-heterogeneity. They also found that increasing the data set size, specifically the number of detectors used, improves the reconstruction of the lesion structure, but does not remove the artifacts. Those results, performed on frequency-domain synthetic and experimental data, indicate that certain artifacts are inherent to the image formation and thereby cannot be removed completely. The cause of such artifacts must as well be inherent to DC-based reconstruction, wherein the outcome relative to frequency-domain reconstruction is unknown.

The analytic approach of this study is based primarily upon a method introduced by Fantini et al [81] to model the accuracies or equivalently the errors associated with a two-distance measurement technique for quantifying the optical properties of bulk homogeneous medium. Reconstructing optical properties in a homogeneous medium is essentially a process of fitting the slopes of measurements with respect to different source-detector distances, for which Fantini et al. introduced their models of the "relative error" of absorption and reduced scattering coefficients using the intensity exponential factor, AC exponential factor, and phase factor between the measurements made at two different source-detector distances. The tomography of optical heterogeneity relies on multiple measurements among spatially-resolved sources and detectors, and the image reconstruction is a process of optimizing the local optical properties to minimize the difference of model prediction for these source/detector pairs with respect to the measured values. The accuracy of reconstruction is thereby dependent upon the capability of distinguishing the signal variations for single source-detector pair due to all types of measurement fluctuations as well as local changes of tissue optical properties, such variations among different source-detector pairs, and mapping such variations to the image-space. Hence, the "relative error" initially discussed in [81] equally applies to tomography of optical heterogeneity, because the "relative error" of measurement determines the upper-limit of reconstruction accuracy, in other words it sets the "parameter-recovery-uncertainty-level (PRUL)" in the tomography images.

This study analyzes the PRULs of the absorption coefficient, the reduced scattering coefficient, and the diffusion coefficient, for the measurement conditions of DC+AC, DC+PHS, and AC+PHS, and examines their representations as image artifacts in synthetic models. Much of the analytic approach of this study is based upon the method established in [78]; however, there are substantial differences in the measurement configurations investigated, and also in this novel study the analytic results partially suggested by [78] are quantitatively evaluated to compare the PRULs among these configurations. It is also noted that [78] considered the measurement configurations of DC+AC, AC+PHS, and DC+PHS. When FD information is available, it is straightforward to apply AC+PHS, as employed by many works [6-12, 14-15], to image reconstruction. The utilization of DC+AC and DC+PHS are mathematically valid; however, those configurations have seldom been used for image reconstruction. This study investigates the level of artifacts in the DC, AC+PHS, and DC+AC+PHS configurations as they are the most likely implemented approaches toward image-reconstruction, therefore among the results previously stated in [78] only those related to AC+PHS have been included in this study when appropriate. The AC+PHS result for absorption coefficient in [78] is cited directly, but the AC+PHS result in [78] for reduced scattering is revised to a more generalized form that is consistent with the result for absorption coefficient. Table 3.1 in subsection 3.3.1 is introduced to make clear these distinctions. This study also investigates reconstruction of the diffusion coefficient, because not only are the absorption and reduced scattering coefficients coupled, but also generally the diffusion coefficient is involved in the reconstruction process *prior* to formulating the reduced scattering coefficient. The diffusion coefficient image may provide new insights to the study even though its artifacts are expected to be close to that seen in reduced scattering image.

The rest of the paper is organized in the following sections: Section 2 analyses the PRUL for three categories: (1) DC only, (2) AC+PHS, and (3) DC+AC+PHS. Tissue and measurement parameters typical to optical tomography applications are implemented to evaluate quantitatively the PRULs expected in the images. Section 3 uses synthetic data to examine the uncertainty of the

parameters recovered for homogeneous medium, single inclusion with different types of optical contrast, and multiple inclusions with specific optical contrasts. These synthetic models are also evaluated selectively for the condition of having spatial *a priori* to the image reconstruction. Section 4 discusses the implications of the results.

3.2 Theory

The reconstruction accuracy of optical tomography is determined by many factors including the accuracy of forward model, the determinacy of inverse formulation, the characteristics of instrument noise [82], etc. An analytic approach has been introduced in [78] to demonstrate that the uncertainty (or error) in the measurement maps to the uncertainty of recovering the assembled optical properties of bulk tissue. The same uncertainty (or error) of the measurement, when involved in tomographic reconstruction to recover spatially-resolved tissue optical properties, will translate to spatially-varying artifacts that reduces the contrast to noise ratio of the target-of-interest. This effect may seem obvious; however, the extent of it was not well-understood. This work closes this gap of knowledge in three conditions of DOT measurements, namely DC, AC+PHS, and complete frequency-domain information by DC+AC+PHS.

3.2.1 Parameter-recovery-uncertainty-level (PRUL)

The variation of the recovered optical properties is modeled as "parameter-recovery-uncertainty-level (PRUL)", which for AC+PHS has been derived in [78] in terms of the attenuation of the AC amplitude and phase shift versus a change of source-detector distances. We implement the approach in [78], but extend it to DC only and DC+AC+PHS configurations, and applying to diffusion coefficient in addition to absorption and reduced scattering coefficients.

The frequency-domain measurement of photon density consists of a steady-state and time-varying components as $U_{FD}(\vec{r},\omega) = U_{DC}(\vec{r}) + U_{AC}(\vec{r},\omega)$, where $\vec{r}$ is the position vector,

and ω is the angular modulation frequency of the light source. The $U_{FD}(\vec{r},\omega)$ satisfies the photon diffusion equation of

$$\left(-\frac{\mu_a(\vec{r})}{D(\vec{r})}+\frac{i\omega}{vD(\vec{r})}\right)U_{FD}(\vec{r},\omega)+\nabla^2 U_{FD}(\vec{r},\omega)=-\frac{S(\vec{r},\omega)}{D(\vec{r})} \tag{3.1}$$

where v is the speed of light in the medium, μ_a is the absorption coefficient, D=[3(μ_a+μ_s')]$^{-1}$ is the diffusion coefficient, μ_s' is the reduced scattering coefficient, and the source term $S(\vec{r},\omega)$ has a direct-current component $S_{DC}(\vec{r})$ and a time-varying component $S_{AC}(\vec{r},\omega)$. For a homogeneous infinite medium with a detector at $\vec{r}$ and a source at $\vec{r}\,'$, thereby a source-detector distance of $d=\left|\vec{r}'-\vec{r}\right|$, we have

$$U_{FD}(\vec{r},\omega)=U_{DC}(\vec{r})+\left|U_{AC}(\vec{r},\omega)\right|\exp(i\Phi_{AC})=\frac{S_{DC}(\vec{r}')}{4\pi Dd}\exp(-k_{DC}d)+\frac{S_{AC}(\vec{r}',\omega)}{4\pi Dd}\exp(-k_{AC}d)\cdot\exp(ik_{PHS}d) \tag{3.2}$$

where

$$k_{DC}=\sqrt{\frac{\mu_a}{D}},\quad k_{AC}=\sqrt{\frac{\mu_a}{2D}\left(\sqrt{1+\frac{\omega^2}{v^2{\mu_a}^2}}+1\right)},\quad k_{PHS}=\sqrt{\frac{\mu_a}{2D}\left(\sqrt{1+\frac{\omega^2}{v^2{\mu_a}^2}}-1\right)} \tag{3.3}$$

It is noted that $k_{AC}>k_{DC}$ and k_{AC} is correlated with but not linearly dependent upon k_{DC}. The attenuation of DC component of the photon density is thus not equal to or linearly dependent upon that of AC component, which is an indication that the DC information would not be a duplication of any of AC or PHS.

Denoting $d_2>d_1$ and $\rho=\left|d_1-d_2\right|$ as the difference of source-detector distance between two measurements corresponding to the same source, one has [78] (reproduced here for convenience)

$$\delta=\ln\left(\frac{d_2}{d_1}\frac{U_{DC}(d_2)}{U_{DC}(d_1)}\right)=-\rho\cdot k_{DC}=-\rho\cdot\sqrt{\frac{\mu_a}{D}}$$

$$\alpha = \ln\left(\frac{d_2}{d_1}\frac{U_{AC}(d_2)}{U_{AC}(d_1)}\right) = -\rho \cdot k_{AC} = -\rho \cdot \sqrt{\frac{\mu_a}{2D}\left(\sqrt{1+\frac{\omega^2}{v^2{\mu_a}^2}}+1\right)} \tag{3.4}$$

$$\phi = \Phi(d_2) - \Phi(d_1) = \rho \cdot k_{PHS} = \rho \cdot \sqrt{\frac{\mu_a}{2D}\left(\sqrt{1+\frac{\omega^2}{v^2{\mu_a}^2}}-1\right)}$$

Table 3.1 lists the "PRUL" of five different measurement configurations, among which three were investigated in [78]. As stated previously, the configuration of DC+AC and DC+PHS were seldom used for image reconstruction, therefore only the AC+PHS results of [78] are cited for this comparative study.

Table 3.1 Comparison of the analytic derivations in this work with that in [78]

	Measurements				
	DC	**DC + AC**	**AC + PHS**	**DC + PHS**	**DC + AC + PHS**
$\frac{\Delta\mu_a}{\mu_a}\left(\frac{\sigma_{\mu_a}}{\mu_a}\right)$	***This study***	[78]	[78]	[78]	***This study***
$\frac{\Delta\mu_s'}{\mu_s'}\left(\frac{\sigma_{\mu_s'}}{\mu_s'}\right)$	***This study***	[78]	[78]*	[78]	***This study***
$\frac{\Delta D}{D}\left(\frac{\sigma_D}{D}\right)$	***This study***		***This study***		***This study***

* The derivation was revised to a more generalized form.

In CW measurement, we have

$$\mu_a|_{DC} = D \cdot \left(\frac{\delta}{\rho}\right)^2 \tag{3.5}$$

References [83-84] suggest that for steady-state surface measurements μ_a and D collectively determine the diffuse reflectance, denoted as R_∞, by the relationship $[\mu_a \cdot D] = K(R_\infty)$. It is noted that the diffuse reflectance is not $U_{DC}(\vec{r})$, which implies treating $K(R_\infty)$ as not significantly dependent upon $U_{DC}(\vec{r})$, thereby equ (3.5) may be converted to

$$\mu_a\big|_{DC} = \frac{\sqrt{K(R_\infty)}}{\rho}\cdot\delta \tag{3.6}$$

and estimating the PRUL of μ_a for DC by

$$\left.\frac{\sigma_{\mu_a}}{\mu_a}\right|_{DC} = \frac{1}{\mu_a}\left[\frac{\partial\mu_a}{\partial\delta}\sigma_\delta\right] = \frac{\sigma_\delta}{\delta} \quad or \quad \left(\frac{\sigma_\delta^2}{\delta^2}\right)^{1/2} \tag{3.7}$$

We have for AC+PHS [78]

$$\mu_a\big|_{AC+PHS} = \frac{\omega}{2v}\left(\frac{\phi}{\alpha}-\frac{\alpha}{\phi}\right) \tag{3.8}$$

and a PRUL of [78]

$$\left.\frac{\sigma_{\mu_a}}{\mu_a}\right|_{AC+PHS} = \frac{1}{\mu_a}\left[\left(\frac{\partial\mu_a}{\partial\alpha}\right)^2\sigma_\alpha^2+\left(\frac{\partial\mu_a}{\partial\phi}\right)^2\sigma_\phi^2\right]^{1/2} = \frac{\alpha^2+\phi^2}{\alpha^2-\phi^2}\left(\frac{\sigma_\alpha^2}{\alpha^2}+\frac{\sigma_\phi^2}{\phi^2}\right)^{1/2} \tag{3.9}$$

For DC+AC+PHS measurement, we have

$$\mu_a\big|_{DC+AC+PHS} = -\frac{\omega}{v}\cdot\frac{\delta^2}{2\alpha\phi} \tag{3.10}$$

and accordingly a PRUL of

$$\left.\frac{\sigma_{\mu_a}}{\mu_a}\right|_{DC+AC+PHS} = \frac{1}{\mu_a}\left[\left(\frac{\partial\mu_a}{\partial\delta}\right)^2\sigma_\delta^2+\left(\frac{\partial\mu_a}{\partial\alpha}\right)^2\sigma_\alpha^2+\left(\frac{\partial\mu_a}{\partial\phi}\right)^2\sigma_\phi^2\right]^{1/2} = \left(4\frac{\sigma_\delta^2}{\delta^2}+\frac{\sigma_\alpha^2}{\alpha^2}+\frac{\sigma_\phi^2}{\phi^2}\right)^{1/2} \tag{3.11}$$

The PRULs in equ.s (3.7), (3.9) and (3.11) all have the shape of

$$\frac{\sigma_\mu}{\mu} = \eta\cdot(\xi)^{1/2} \tag{3.12}$$

that contains a multiplication factor η and a square root term $\sqrt{\xi}$. The relative levels of these PRULs become comparable as $\frac{\sigma_\phi^2}{\phi^2}, \frac{\sigma_\alpha^2}{\alpha^2}$ and $\frac{\sigma_\delta^2}{\delta^2}$ are practically the same [78]. It is indicated in

Table 3.2 that the PRUL of μ_a will be the lowest in DC-based reconstruction, but whether the PRUL of μ_a is lower in AC+PHS or in DC+AC+PHS depends upon the difference in α and ϕ .

Table 3.2 Comparison on PRUL of μ_a (σ_{μ_a}/μ_a)

Equ.	Condition	η		$\sqrt{\xi}$		Normalized $\eta\cdot\sqrt{\xi}$
		Expression	Value	Expression	Normalized value	
(3.7)	**DC**		1	$\left(\frac{\sigma_\delta^2}{\delta^2}\right)^{1/2}$	1	1
(3.9)	**AC+PHS**	$\left(\frac{\alpha^2+\phi^2}{\alpha^2-\phi^2}\right)$	>1	$\left(\frac{\sigma_\alpha^2}{\alpha^2}+\frac{\sigma_\phi^2}{\phi^2}\right)^{1/2}$	1.41	>1.41
(3.11)	**DC+AC+ PHS**		1	$\left(4\frac{\sigma_\delta^2}{\delta^2}+\frac{\sigma_\alpha^2}{\alpha^2}+\frac{\sigma_\phi^2}{\phi^2}\right)^{1/}$	2.45	2.45

Because the image reconstruction recovers *D* to formulate μ_s', it is imperative to analyze the PRUL of *D.* For the case of DC, similar to the derivation for μ_a we have

$$D\big|_{DC}=\sqrt{K(R_\infty)}\cdot\left(\frac{\rho}{\delta}\right) \tag{3.13}$$

and

$$\left.\frac{\sigma_D}{D}\right|_{DC}=\frac{1}{D}\left[\frac{\partial D}{\partial\delta}\sigma_\delta\right]=\frac{\sigma_\delta}{\delta}\quad or\quad \left(\frac{\sigma_\delta^2}{\delta^2}\right)^{1/2} \tag{3.14}$$

For AC+PHS and DC+AC+PHS, the expressions are the same:

$$D\big|_{AC+PHS}=D\big|_{DC+AC+PHS}=-\frac{\omega\rho^2}{2v}\cdot\frac{1}{\alpha\phi} \tag{3.15}$$

Therefore

$$\left.\frac{\sigma_D}{D}\right|_{AC+PHS}=\left.\frac{\sigma_D}{D}\right|_{DC+AC+PHS}=\frac{1}{D}\left[\left(\frac{\partial D}{\partial\alpha}\right)^2\sigma_\alpha^2+\left(\frac{\partial D}{\partial\phi}\right)^2\sigma_\phi^2\right]^{1/2}=\left(\frac{\sigma_\alpha^2}{\alpha^2}+\frac{\sigma_\phi^2}{\phi^2}\right)^{1/2} \tag{3.16}$$

The PRULs of *D* in (3.15) and (3.16) are compared in Table 3.3. Apparently when AC and phase are employed the DC component is redundant for the recovery of *D.*

Table 3.3 Comparison on PRUL of *D*

Equ.	Condition	Expression	Normalized Value
(3.14)	**DC**	$\left(\frac{\sigma_\delta^2}{\delta^2}\right)^{1/2}$	1
(3.16)	**AC+PHS & DC+AC+PHS**	$\left(\frac{\sigma_\alpha^2}{\alpha^2}+\frac{\sigma_\phi^2}{\phi^2}\right)^{1/2}$	~1.41

The PRUL of μ_s' is derived by:

$$\frac{\sigma_{\mu_s'}}{\mu_s'}=\frac{1}{\mu_s'}\left[\left(\frac{\partial\mu_s'}{\partial D}\right)^2\sigma_D^2+\left(\frac{\partial\mu_s'}{\partial\mu_a}\right)^2\sigma_{\mu_a}^2\right]^{1/2}=\left[\frac{1}{3D}-\mu_a\right]^{-1}\cdot\left[\left(\frac{1}{3D}\right)^2\left(\frac{\sigma_D}{D}\right)^2+(\mu_a)^2\left(\frac{\sigma_{\mu_a}}{\mu_a}\right)^2\right]^{1/2} \quad (3.17)$$

so the PRUL of μ_s' for DC is,

$$\left.\frac{\sigma_{\mu_s'}}{\mu_s'}\right|_{DC}=\left[\frac{1}{3D}-\mu_a\right]^{-1}\left[\left(\frac{1}{3D}\right)^2\cdot\left(\frac{\sigma_\delta^2}{\delta^2}\right)\cdot+\mu_a^2\cdot\left(\frac{\sigma_\delta^2}{\delta^2}\right)\cdot\right]^{1/2} \quad (3.18)$$

for AC+PHS is [78]*:

$$\left.\frac{\sigma_{\mu_s'}}{\mu_s'}\right|_{AC+Phs}=\left[\frac{1}{3D}-\mu_a\right]^{-1}\cdot\left[\left(\frac{1}{3D}\right)^2\left(\frac{\sigma_\alpha^2}{\alpha^2}+\frac{\sigma_\phi^2}{\phi^2}\right)+\mu_a^2\cdot\left(\frac{\alpha^2+\phi^2}{\alpha^2-\phi^2}\right)^2\cdot\left(\frac{\sigma_\alpha^2}{\alpha^2}+\frac{\sigma_\phi^2}{\phi^2}\right)\right]^{1/2} \quad (3.19)$$

(*Notes: the original derivation in [78] for $\sigma_{\mu_s'}/\mu_s'$ has ρ in the equation, which is inconsistent with that obtained for σ_{μ_a}/μ_a . equ (3.19) corrected this inconsistency) and for DC+AC+PHS is:

$$\left.\frac{\sigma_{\mu_s'}}{\mu_s'}\right|_{DC+AC+Phs}=\left[\frac{1}{3D}-\mu_a\right]^{-1}\cdot\left[\left(\frac{1}{3D}\right)^2\left(\frac{\sigma_\alpha^2}{\alpha^2}+\frac{\sigma_\phi^2}{\phi^2}\right)\cdot+\mu_a^2\cdot\left(4\frac{\sigma_\delta^2}{\delta^2}+\frac{\sigma_\alpha^2}{\alpha^2}+\frac{\sigma_\phi^2}{\phi^2}\right)\right]^{1/2} \quad (3.20)$$

Based on the estimation leading to Table 3.2, the PRULs in Eqs. (3.19) and (3.20) can be normalized with respect to equ (3.18). The results are given in Table 3.4. Again the PRUL of μ_s'

will be the lowest for DC. Whether the PRUL of μ_s' is lower in AC+PHS or in DC+AC+PHS depends also upon the difference in α and ϕ as for the PRUL of μ_a, but because of the dominance of $1/3D$ over μ_a, the difference between AC+PHS and DC+AC+PHS will be less than that observed for PRUL of μ_a in Table 3.2.

Table 3.4 Comparison on PRUL of μ_s'

Equ.	Condition	Expression	Normalized as
(3.18)	**DC**	$\left[\left(\frac{1}{3D}\right)^2\left(\frac{\sigma_\delta^2}{\delta^2}\right)+\mu_a^2\cdot\left(\frac{\sigma_\delta^2}{\delta^2}\right)\right]^{1/2}$	1
(3.19)	**AC+PHS**	$\left[\left(\frac{1}{3D}\right)^2\left(\frac{\sigma_\alpha^2}{\alpha^2}+\frac{\sigma_\phi^2}{\phi^2}\right)+\mu_a^2\cdot\left(\frac{\alpha^2+\phi^2}{\alpha^2-\phi^2}\right)^2\cdot\left(\frac{\sigma_\alpha^2}{\alpha^2}+\frac{\sigma_\phi^2}{\phi^2}\right)\right]^{1/2}$	>1.41
(3.20)	**DC+AC+PHS**	$\left[\left(\frac{1}{3D}\right)^2\left(\frac{\sigma_\alpha^2}{\alpha^2}+\frac{\sigma_\phi^2}{\phi^2}\right)+\mu_a^2\cdot\left(4\frac{\sigma_\delta^2}{\delta^2}+\frac{\sigma_\alpha^2}{\alpha^2}+\frac{\sigma_\phi^2}{\phi^2}\right)\right]^{1/2}$	>1.41

3.2.2 Summary of the PRUL analyses

The DC-only reconstruction seems to give the least level of relative uncertainty of the parameter in the reconstruction. The AC+PHS configuration seems to be equivalent to DC+AC+PHS in the level of PRULs of reduced scattering and diffusion coefficient, but it is unclear for absorption coefficient. These analyses have been conducted for infinite homogeneous medium, but results will be readily translatable to a medium with boundaries and with inclusions.

3.3 Synthetic studies

Simulations are carried out to study the practical issues of PRUL, such as background noise, the accuracy of optical property recovery, and the inter-parameter cross-coupling, of the three measurements setups.

3.3.1 Synthetic model

The forward model is carried out by finite element method (FEM) solution of equ (3.1) using the Robin type boundary condition:

$$U(\vec{r}_0,\omega) - 2DA\hat{n}_0 \cdot \nabla U(\vec{r}_0,\omega) = 0 \tag{3.21}$$

where A is related to refractive index-mismatch, and $\hat{n}_0$ is an outgoing normal vector. The Jacobian is structured to the form of:

$$J = \begin{bmatrix} DC \\ AC \\ PHS \end{bmatrix} = \begin{bmatrix} \frac{\partial \ln U_{DC}}{\partial \mu_a} & \frac{\partial \ln U_{DC}}{\partial D} \\ \frac{\partial \ln |U_{AC}|}{\partial \mu_a} & \frac{\partial \ln |U_{AC}|}{\partial D} \\ \frac{\partial \Phi_{AC}}{\partial \mu_a} & \frac{\partial \Phi_{AC}}{\partial D} \end{bmatrix} \tag{3.22}$$

where the indices of each block of Jacobian could be node-based for pixel-wise reconstruction or region-based for *prior*-guided region-wise reconstruction. Utilizing only the first row leads to CW, utilizing the second and third rows renders AC+PHS, and utilizing all three rows gives DC+AC+PHS. The inverse solver implements the Levernberg-Marquardt algorithm as

$$x_{k+1} = x_k + \alpha \cdot [J^T(x_k)J(x_k) + \lambda I]^{-1} J^T(x_k)\Delta v(x_k) \tag{3.23}$$

where x is the array of unknown parameters, Δv is the forward projection error and λ is a penalty or regularization term. The value of λ is initially set as 100, and is reduced to its fourth root after each iteration of which the projection error is reduced. The damping factor, α , in the range of (0, 1) is introduced when only region-wise reconstruction is performed to facilitate stable convergence [46] and is set at 0.5 in this study when included. For pixel-wise reconstructions using NIRFAST [11, 85], α is set to 1.

3.3.2 Simulation Results

Synthetic data are generated for a homogeneous medium, a medium with single inclusion, and a medium with multiple inclusions with mixed type of optical heterogeneities.

3.3.2.1 The PRULs in a homogeneous medium

A cylinder-applicator geometry [54, 86] of 60mm in height and 86mm in diameter with 16 optodes is adopted, like the one shown in Fig.3.1. The optodes are turned on sequentially for

the measurements being taken by all other optodes, generating a total of 240 measurements for each data set.

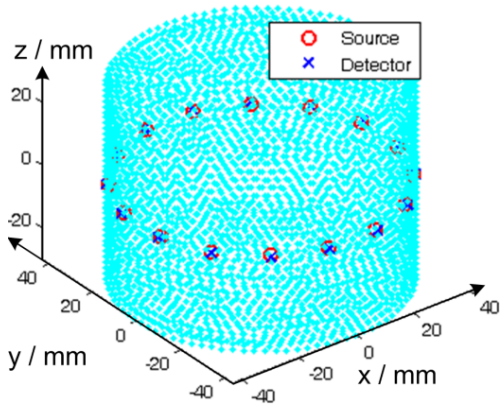

Fig.3.1. Imaging geometry for a homogeneous medium

The volume is discretized into an FEM mesh of 12695 nodes for forward computation while a smaller FEM mesh of 600 nodes is used in the reconstruction. Because this synthetic study specifically investigates the level of artifacts reconstructed to the same level of recovered parameter in an otherwise homogeneous medium, the same optical properties of μ_a=0.01mm^{-1} and μ_s'=1mm^{-1} are used for both forward computation and as the initial values of the inverse routine, with 1% noise added to the forward simulation data to maintain the same measurement error. In addition, all controlling parameters of the inverse model are maintained the same for DC, AC+PHS, and DC+AC+PHS configurations.

Table 3.5 demonstrates that the variations recovered to the parameters of a homogeneous medium are lowest in DC, as expected from the analytic analysis. The DC+AC+PHS slightly outperforms AC+PHS in μ_a recovery, but AC+PHS slightly outperforms DC+AC+PHS in μ_s'/D recovery.

Table 3.5 Mean value and standard deviation reconstructed for homogeneous medium

	$\overline{\mu_a}$	σ_{μ_a} (mm^{-1})		$\overline{\mu_s'}$	$\sigma_{\mu_s'}$ (mm^{-1})		$\overline{D}$	σ_D (mm)	
		Abs.	Norm.		Abs.	Norm.		Abs.	Norm.
DC	0.01	0.69×10^{-6}	1	1.00	0.80×10^{-4}	1	0.33	2.64×10^{-3}	1
AC+PHS	0.01	3.13×10^{-6}	4.50	1.00	1.18×10^{-4}	1.47	0.33	3.83×10^{-3}	1.45

DC+AC +PHS	0.01	2.98×10^{-6}	4.29	1.00	1.31×10^{-4}	1.64	0.33	4.24×10^{-3}	1.60

Note: "Abs." denotes the absolute value of the standard deviation. "Norm." denotes the standard deviation normalized with respect to the standard deviation of DC. The same notations apply to Tables 6 and 8.

The normalized numbers (1.45~1.64) for μ_s'/D recovery are considerably close to those in the analytical derivation--with the same average optical properties, the background standard deviation of the images reconstructed by FD system measurements is at least 1.41 times larger than those reconstructed by CW system. However, in μ_a reconstruction, the variations in FD configurations are about twice of those predicted in Table 3.2. It is noted that the analytic results in this study are based upon perturbation analysis. It is well-known that DOT is a non-linear process wherein the absorption perturbation is more pronounced than scattering perturbation. In this specific model of homogeneous medium, the signal perturbation is evenly distributed to the entire volume of the homogeneous medium instead of mostly confined to smaller lesions with higher optical property contrast as in the later examinations, therefore the perturbations from AC and PHS could have been coupled to and non-linearly amplified as the variation of absorptions.

3.3.2.2 Contrast to noise ratio analysis for single target

The results in the last subsection indicate that for 1% noise in the measurement of homogeneous medium, DC only reconstruction clearly maintains a lower artifact level compared to DC+AC+PHS and AC+PHS. This study examines the contrast of a target inclusion in an otherwise homogeneous medium at different measurement noise levels when reconstructed by DC, AC+PHS, DC+AC+PHS configurations. The synthetic model is similar to that in 3.3.2.1, but with a spherical heterogeneity added at (x=0mm, y=-20mm, z=0mm) with μ_a=0.025mm^{-1} and μ_s'=1.75mm^{-1}. The reconstruction basis of 2760-nodes is larger than the one used for 3.3.2.1. Varying noise levels of 0% to 10% are integrated into the forward data to examine the contrast to noise ratios of the target (CNR = [max(target-region-value)-mean(background-value)] / background-standard-deviation) with respect to the background artifacts. The background

deviation is calculated by excluding the areas within a distance of 1.5 times of the target radius away from its center [54]. The calculated CNRs are given in Fig.3.2 for the three types of target contrasts. It is observed in Fig.3.2 that the CNR levels of μ_a and D look similar when compared to that of μ_s', which supports the assumptions made for deriving PRULs of μ_a and D in Eqs. (3.7) and (3.14). In Fig.3.2, the CNR levels of μ_a is found lower than that of μ_s', which may be due to underestimation of μ_a and over-estimation of μ_s' in such pixel-wise image reconstruction. Despite this, several features can be observed in Fig.3.3: (1) At zero-noise level, the three methods are comparable in the CNR; (2) When the noise becomes higher, the DC clearly outperforms the other two in CNR, while DC+AC+PHS slightly outperforms AC+PHS. (3) At 10% noise level, the CNRs of all methods are similar for μ_s' and D recovery, but DC still outperforms the other two in μ_a reconstruction.

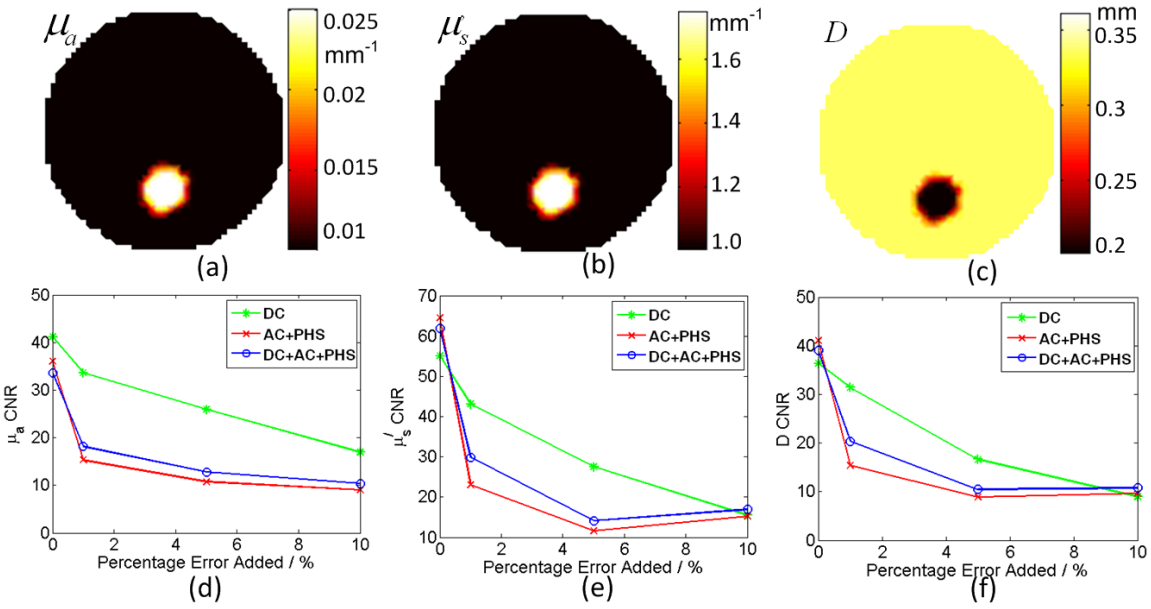

Fig.3.2. Contrast-to-noise-ratio (CNR) with respect to the measurement noise levels.. (a) (b) (c) $\mu_a/\mu_s'/D$ distribution in the z=0 plane of forward model (d) μ_a CNR Comparison (e) μ_s' CNR Comparison (f) D CNR Comparison

3.3.2.3 Multiple target case

The geometry for having multiple inclusion is shown in Fig.3.3, where three spherical targets with radius of 7.5mm are located in the longitudinal middle plane (z=0) of the cylindrical imaging volume and are all 20mm away from the center of the circular cross-section, ensuring the same spatial sensitivity at their positions. The target 1 at the upper-left (x=-14.14mm, y=14.14mm, z=0mm) has only absorption contrast (μ_a=0.025mm^{-1}, μ_s'=1mm^{-1}), the target 2 at upper-right (x=14.14mm, y=14.14mm, z=0mm) has only scattering contrast (μ_a=0.01mm^{-1}, μ_s'=1.75mm^{-1}), and the target 3 at lower side (x=0mm, y=-20mm, z=0mm) has contrasts of both absorption and reduced scattering (μ_a=0.025mm^{-1}, μ_s'=1.75mm^{-1}). The gold dashed line in the figure marks the position of the target when it presents no contrast in that category. Table 3.6 lists the deviation of the background optical property in the reconstructed images. Standard deviation values in Table 3.6 are normalized along each column versus those of DC-only reconstruction.

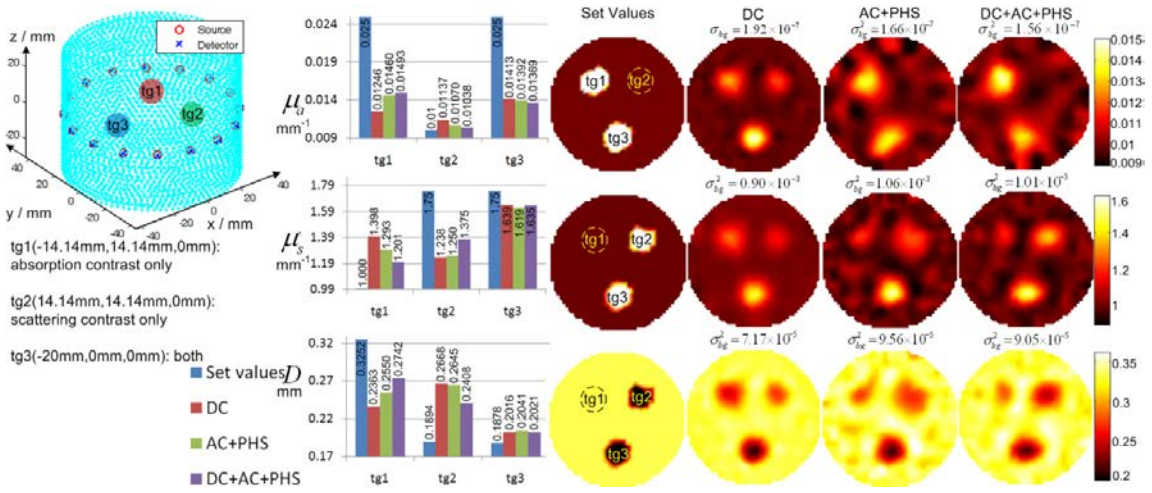

Fig.3.3. Simulation studies for reconstructing multiple targets in a 3-dimensional cylindrical geometry with the optodes and targets located on one plane.

Table 3.6 Standard deviation of background optical properties in Fig.3.3

	σ_{μ_a} (mm^{-1})		$\sigma_{\mu_s'}$ (mm^{-1})		σ_D (mm)	
	Abs.	Norm.	Abs.	Norm.	Abs.	Norm.
DC	1.92×10^{-4}	1	2.46×10^{-2}	1	7.25×10^{-3}	1
AC+PHS	3.63×10^{-4}	1.89	2.88×10^{-2}	1.17	9.01×10^{-3}	1.24

DC+AC+PHS	3.45×10^{-4}	1.79	2.49×10^{-2}	1.01	7.75×10^{-3}	1.07

For background homogeneity, comparison in Table 3.6 indicates that DC only demonstrates the lowest artifact level in the image background while the background artifact level of DC+AC+PHS and AC+PHS is approximately 1 to 2 times higher. Although the numerical simulative result does not exactly match the values in Table 3.2 to 3.4, it qualitatively agrees with the analytical derivations. The analytical derivations given in Table 3.2 to 3.4 indicate that DC+AC+PHS and AC+PHS produces similar background homogeneity, but the simulation results all indicated a slightly lower background artifact level in DC+AC+PHS reconstruction. For target accuracy, the reconstructed images in Fig.3.3 and data comparison in Table 3.7 are seen with DC+AC+PHS superior to AC+PHS, which along with the comparison on the background homogeneity, indicates that including DC generally improves the FD reconstruction. In terms of the inter-parameter cross-coupling, the DC has more coupling than FD, which is well-known. The cross-coupling in DC+AC+PHS is slightly less severe than that in AC+PHS.

Table 3.7 Comparison of the accuracy of recovered optical properties in Fig.3.3

	μ_{a1} (mm^{-1})		μ_{s1}' (mm^{-1})		D_1 (mm)	
	value	**error**	**value**	**error**	**value**	**error**
Set	0.025		1		0.325	
DC	0.0125	-50.16%	1.398	39.84%	0.236	-27.35%
AC+PHS	0.0146	-41.62%	1.293	29.27%	0.255	-21.59%
DC+AC+PHS	0.0149	-40.30%	1.201	20.06%	0.274	-15.67%
	μ_{a2} (mm^{-1})		μ_{s2}' (mm^{-1})		D_2 (mm)	
	value	**error**	**value**	**error**	**value**	**error**
Set	0.01		1.75		1.75	
DC	0.0114	13.68%	1.238	-29.25%	1.639	-6.34%
AC+PHS	0.0107	6.95%	1.250	-28.56%	1.619	-7.47%
DC+AC+PHS	0.0104	3.81%	1.375	-21.45%	1.635	-6.55%
	μ_{a3} (mm^{-1})		μ_{s3}' (mm^{-1})		D_3 (mm)	
	value	**error**	**value**	**error**	**value**	**error**
Set	0.025		1.75		0.188	
DC	0.0141	-43.48%	1.639	-6.34%	0.2012	7.37%
AC+PHS	0.0139	-44.31%	1.619	-7.47%	0.204	8.70%

DC+AC+PHS	0.0137	-45.24%	1.635	-6.55%	0.202	7.64%

A similar study is conducted for the same targets in a three-ring setup [86] in Fig.3.4 which has three identical rings of optodes at the azimuthal planes of z=-10mm, z=0mm and z=10mm. Each set of data contains a total of 2256 measurements by turning on one source and detecting at all other optodes. The key values are compared in Table 3.8, 3.9. Most features of the three aspects discussed for the single ring case can be reconfirmed, except that the target contours recovered by FD reconstructions are more accurately defined, but nonetheless the difference between DC+AC+PHS and AC+PHS is insignificant.

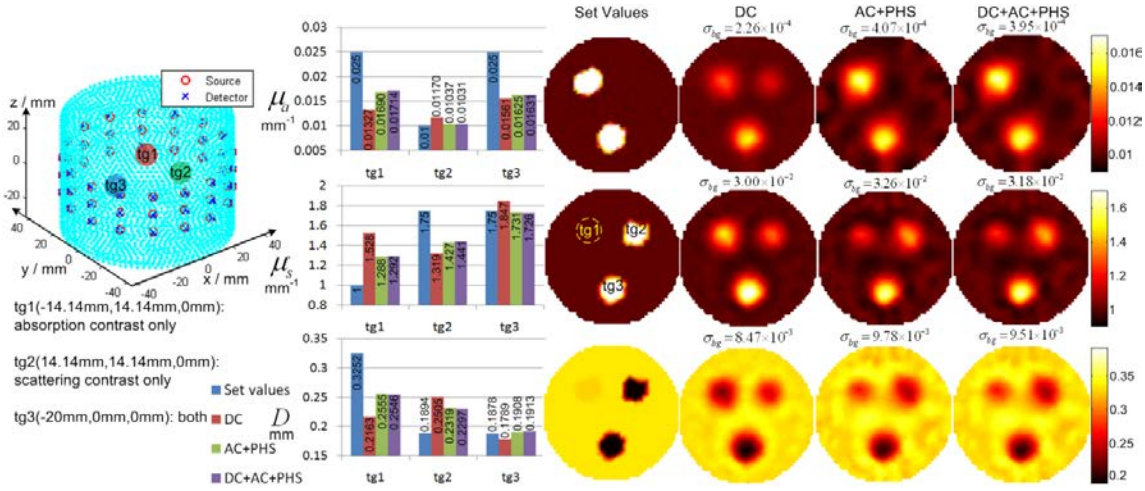

Fig.3.4. Simulation studies for reconstructing multiple targets in a 3-dimensional cylindrical geometry with the optodes located on 3 different planes and targets located on the middle plane.

Table 3.8 Standard deviation of background optical properties in Fig.3.4

	σ_{μ_a} (mm^{-1})		$\sigma_{\mu_s'}$ (mm^{-1})		σ_D (mm)	
	Abs.	Norm.	Abs.	Norm.	Abs.	Norm.
DC	2.26×10^{-4}	1	3.00×10^{-2}	1	8.47×10^{-3}	1
AC+PHS	4.07×10^{-4}	1.80	3.26×10^{-2}	1.09	9.78×10^{-3}	1.15
DC+AC+PHS	3.95×10^{-4}	1.75	3.18×10^{-2}	1.06	9.51×10^{-3}	1.12

Table 3.9 Comparison of the accuracy of recovered optical properties in Fig.3.4

	μ_{a1} (mm^{-1})		μ_{s1}' (mm^{-1})		D_1 (mm)	
	value	**error**	**value**	**error**	**value**	**error**
Set	0.025		1		0.325	
DC	0.0133	-46.93%	1.528	52.81%	0.216	-33.49%
AC+PHS	0.0169	-32.39%	1.288	28.77%	0.256	-21.43%
DC+AC+PHS	0.0171	-31.42%	1.292	29.21%	0.255	-21.70%
	μ_{a2} (mm^{-1})		μ_{s2}' (mm^{-1})		D_2 (mm)	
	value	**error**	**value**	**error**	**value**	**error**
Set	0.01		1.75		0.189	
DC	0.0117	16.95%	1.319	-24.63%	0.251	32.26%
AC+PHS	0.0104	3.73%	1.427	-18.45%	0.232	22.46%
DC+AC+PHS	0.0103	3.09%	1.441	-17.66%	0.230	21.31%
	μ_{a3} (mm^{-1})		μ_{s3}' (mm^{-1})		D_3 (mm)	
	value	**error**	**value**	**error**	**value**	**error**
Set	0.025		1.75		0.188	
DC	0.0156	-37.57%	1.847	5.57%	0.178	-4.73%
AC+PHS	0.0163	-35.02%	1.731	-1.10%	0.191	1.61%
DC+AC+PHS	0.0163	-34.77%	1.726	-1.38%	0.191	1.88%

Prior-guided region-based reconstructions are also performed on both of the imaging geometries of Fig.3.3 and 3.4 to examine if including accurate *a priori* structural information of the target affects the outcome of the three reconstruction configurations. As is shown in Fig.3.5 and 3.6, with the forward models the same as those in Fig.3.5 and 3.6, the inverse model has integrated spatial *prior* information by assuming a homogeneous target of the accurate size in a homogeneous background. Results of both cases indicate that with the structural *a priori* information, the performances of the three configurations are essentially equivalent to each other.

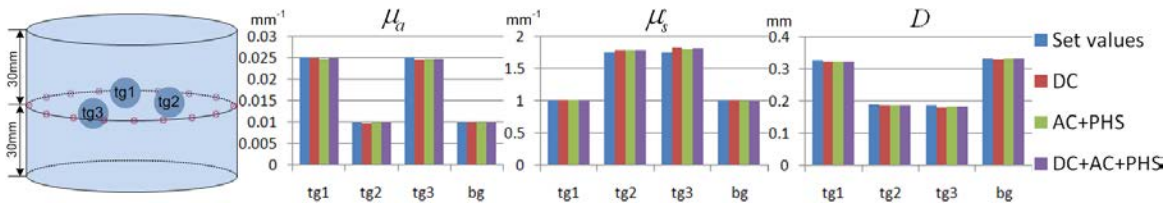

(a) (b)

Fig.3.5. Region-based reconstruction for multiple targets in a 3-dimensional cylindrical geometry with the optodes and targets located on one plane. (a) Imaging geometry and the regions of interest; (b) Comparison of the results for DC, AC+PHS, and DC+AC+PHS.

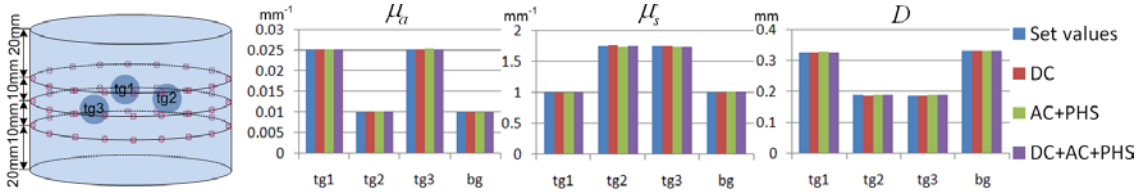

(a) (b)

Fig.3.6. Region-based reconstruction for multiple targets in a 3-dimensional cylindrical geometry with the optodes located on 3 different planes and targets located on the middle plane. (a) Imaging geometry and the regions of interest; (b) Comparison of the results for DC, AC+PHS, and DC+AC+PHS.

3.4 Discussions

Using only the DC information to simultaneously recover the absorption and diffusion (or the reduced scattering) distributions has been controversial. The non-uniqueness that may be inherent to DC-only measurements was described in a seminal study[87]. However, despite the negative predictions in [87] that there could have an infinite number of diffusion & absorption pairs leading to the same surface measurements, Harrach [88] proved that at most one of them consists of a piecewise constant diffusion and piecewise analytic absorption, and if the true medium has these properties as in virtually any practical condition, a reconstruction algorithm favoring these properties will pick the right combination of profiles. Harrach's study theoretically

justified the experiences in many works wherein the absorption and scattering distributions have been separately and uniquely recovered by surface measurement of DC only.

The primary aim of this work is to understand the expectation for DC-based reconstruction in a more systematic approach, thereby to establish certain level of confidence for the recovered information when only DC information can be relied upon. This work, conveyed by a side-by-side comparison of the reconstructions based on DC, AC+PHS, and DC+AC+PHS, does provide direct evidence that DC-based reconstruction is much less-accurate in recovering the absolute optical properties of target-of-interest when no additional spatial information is available to confine the reconstruction, as having been universally recognized by the DOT community. However, apart from these well-expected shortcomings, it seems that DC-based reconstruction may not be completely unfavorable. This study generalized the analytical approach initially proposed in [78] to quantify the level of image artifacts that is expressed by the standard deviation of a parameter over the parameter itself. Parameters representative of tissue measurements are used to evaluate the analytic results and conduct the synthetic studies, in both of which the DC reconstruction produced lower level of relative variation in the optical parameters recovered, and some advantages in the CNR. It may be argued that DC flattens images, leading to a lower standard deviation in the background, and because the background standard deviation is the denominator of CNR, the CNR of DC could become better. But if there were flattening of the image, then the numerator of CNR would also be flattened, and perhaps flattened more strongly owing to the non-linearity of DOT thereby under-estimated at a higher level, that collectively might reduce the CNR rather than increase the CNR. The slight but notable CNR advantage of DC over FD-based reconstruction demonstrated in this study strongly suggest some inherent advantages of DC, but on the other hand, it could be just because DC has lower information content, similar to what one could expect by reducing the amount of data available or increasing the regularization in FD-based reconstructions.

It is worthwhile to note that this study (as well as most other synthetic studies) assumes a step change of the optical properties of the target-of-interest with respect to the background. This is not a faithful representation of the actual tissue-imaging applications, wherein the target-of-interest frequently has a tapered or smooth change of contrast over the background. The stronger cross-talk between absorption and scattering seen for DC-only reconstruction in this study as well as many other studies could have been the outcome of the non-uniqueness revealed by [87] that is pronounced when the target-of-interest has a step contrast over the background. In fact, the DC-based reconstruction of *in vivo* measurements has encountered notably different absorption and scattering patterns of a target-of-interest[89], which may indicate a weaker cross-talk for smoother contrast of the target-of-interest. It is also noted that this study as well as most other synthetic studies assumes a globally homogenous yet locally heterogeneous background. Actual tissue environment could be locally homogenous but globally strongly heterogeneous such as found in prostate [78]. In such conditions a balance or trade-off may exist between the ability of suppressing the background heterogeneity and the likelihood of identifying a target-of-interest of which the contrast is strong locally but weak globally.

This study has also indicated that including DC information in FD-reconstruction can sometimes lead to better images than ignoring it. The expressions of δ and α in equ (3.4) demonstrate that the DC attenuation is not linearly dependent upon the AC attenuation, and the difference between the two attenuation values increases as the modulation frequency increases. The necessity of including DC in order to optimize the frequency-domain reconstruction is made evident by the results in section 3.2.2 and 3.2.3 wherein the DC+AC+PHS results have always been slightly better than the AC+PHS results, on the background artifacts, the target properties, and the cross-coupling between μ_a and μ_s'/D. However the slightly better performance of DC+AC+PHS over AC+PHS diminishes as the total number of measurements goes up, as is shown in the 3-ring case in 3.2.3. When fewer measurements are available in application

situations including the DC information in the limited frequency-domain measurements likely will improve the overall reconstruction outcome.

This study is carried out for the measurements at a single-wavelength. Investigating the PRUL issues in the context of multi-band frequency-domain measurements will be a natural and more practical extension of this work as most optical tomography measurements are conducted with some kind of spectral information. Besides, similar approaches may be extended to other applications wherein the measurement data contains multiple aspects of information, from which the data usage may be optimized for the specific system configuration.

3.5 Summary

In conclusion, the level of variations of recovered optical properties in optical tomography associated with the measurement-uncertainty under three reconstruction configurations of DC-only, the DC-excluded frequency-domain, and the DC-included frequency-domain, is studied by analytic and synthetic means. It is demonstrated that at the same level of measurement uncertainty typical to optical tomography and under pixel-wise reconstruction without spatial *prior*, the standard deviations of μ_a over μ_a reconstructed by DC-only is at least 1.4 times lower than that by frequency-domain methods. The standard deviations of D (or μ_s') over D (or μ_s') reconstructed by DC-only are slightly lower than those by frequency-domain methods. Frequency-domain reconstruction including DC generally outperforms reconstruction excluding DC, but the difference between the two becomes less significant when the total amount of measurements become larger. For frequency-domain reconstruction with no spatial *prior* and less amount of measurements, including DC is recommended. When *a priori* structural information is available, the three reconstruction configurations investigated in this study perform equally well.

CHAPTER IV

SPECTRAL *PRIOR* UTILIZATION AND OPTIMIZATION IN NEAR INFRARED DIFFUSE OPTICAL TOMOGRAPHY

4.1 Introduction

Multi-spectral near infrared optical tomography aims to reconstruct pathologically-relevant optical heterogeneities in biological tissue from information obtained over a spectrum of light [66, 90-93]. The technique utilizes measurements at multiple wavelengths to decompose the spectrally variant tissue optical properties such as absorption and reduced scattering coefficients into spectrally invariant chromophore concentrations and spectrally insensitive scattering properties such as scattering power and scattering amplitude [90]. Although discussions remain over the uniqueness of optical tomography reconstruction by single wavelength Continuous-Wave (CW) or Direct-Current (DC) measurements [87-88], the unique solution to optical tomography reconstruction based on spectrally-constrained DC measurement has been demonstrated by Corlu et al. [90]. Further studies based on DC measurements have been reported for imaging of breast [7, 91, 94], prostate [95], brain function [96], small animal [97], etc., and the spectrally-constrained DC-based reconstruction is shown to be more robust than the spatially-constrained single-wavelength DC-based reconstruction in recovering the and the spectrally-constrained DC-based reconstruction is shown to be more robust than the spatially-constrained single-wavelength DC-based reconstruction in recovering the optical heterogeneities [98].

In recent studies [63, 99], Wang et al. implemented broadband frequency domain (FD) measurements to multispectral optical tomography reconstruction. The studies concluded that increasing the bandwidth of FD measurements improves reconstruction results. In their subsequent studies, Wang et al. integrated the FD detection with DC [100-101] measurements to further expand the effective spectral bandwidth for reconstruction. The successful outcome of such FD/DC complemented approach, nonetheless, underlines a more fundamental enquiry, that is, under the same spectral-constraint, how DC based reconstruction performs with respect to FD based reconstruction. Intuitively, one might expect FD reconstruction to outperform DC reconstruction in all aspects owing to the extra phase information. However, such consideration has neither been confirmed nor negated, for which direct comparison of DC and FD reconstructions under the same context of spectral-constraint is necessary. For non-spectrally-constrained optical tomography, or optical tomography at single-wavelength, our previous study [102] investigated three conditions of reconstruction: 1) DC-only; 2) DC-excluded FD, i.e. utilizing only the modulation amplitude (AC) and phase shift (PHS); and 3) DC-included FD, i.e. including DC, AC and PHS. It is revealed that the DC-only reconstruction, despite the less accurate estimation of the target optical properties, presents higher Contrast-to-Noise-Ratio (CNR) than the FD reconstruction does, thereby potentially better resolves the targets in certain noisy circumferences. It is also demonstrated that with spatial-*prior*, DC-only reconstruction is essentially equivalent to FD reconstructions, and without spatial-*prior*, DC-included FD reconstruction generally outperforms DC-excluded FD reconstruction. Will spectrally-constrained reconstruction have similar outcome?

The study in [102] introduced an analytic model to estimate the translation of uncertainties in the measurements to the uncertainties in the reconstructed images, namely parameter-recovery-uncertainty-level (PRUL). This current study aims to evaluate the PRULs in spectrally-constrained optical tomography reconstruction. Specifically, we explore the PRULs of the concentrations of several important NIR chromophores, including oxygenated hemoglobin

(HbO), deoxygenated hemoglobin (Hb), and water, and scattering parameters such as scattering amplitude and scattering power. The PRUL analyses are for the measurements of DC-only, DC-excluded FD, and DC-included FD, as did with the study in [102], even though other configurations of DC/FD measurements could be employed [81]. The PRUL analyses are, essentially, to quantify the gradients of the chromophore concentrations and scattering components with respect to DC or FD measurement components. This study seeks to derive the wavelength-specific gradients of the chromophore concentrations and scattering components with respect to the optical properties in DC or FD measurements, which are then to be integrated with the gradients of the optical properties with respect to DC or FD measurements previously analyzed in [102] to reach the complete expressions of PRULs in multi-spectral measurements.

A practical issue arises in spectrally-constrained optical tomography is the selection of optimal set of wavelengths given the choices of doing so in the system integration. The optimization approaches demonstrated by Corlu et al. [7] and Eames et al. [103] are similar as both methods compare the residue and condition numbers of numerically approximated sensitivity matrices derived for each set of the wavelength combinations. This current work proposes a novel method of optimizing the wavelength selection for spectrally-constrained optical tomography reconstruction based on the PRUL analyses. As the gradients in PRULs are formatively equivalent to the sensitivity matrices, the new method is shown to optimize the wavelength selection as effectively as Corlu's and Eames' methods do, but at much lower computational load.

The PRUL analyses under spectral-constraint as well as the newly proposed method for spectral-*prior* optimization are examined by synthetic studies in two imaging geometries. One of the imaging geometries is to have the circular applicator enclosing the medium [91, 103]. In such geometry the sensitivity along the depth is considerably homogeneous within its imaging domain. The other geometry is to have the circular applicator enclosed by the medium for transverse or axial imaging, as in endo-rectal NIR tomography scenarios [42, 95]. In such geometry, the

sensitivity decays quite significantly as the depth increases. The synthetic studies are to recover targets each of which possesses only one independent contrast, and to resolve two closely positioned targets of identical studied properties. Evaluation criteria include the recovered target properties and the noise-to-contrast-ratio (NCR). In this study, NCR is defined as, opposed to CNR, the absolute levels of the background artifacts normalized by the target-to-background contrast, therefore a lower NCR is perferred.

It is well-known that multi-spectral optical tomography reconstruction can be implemented in two ways. A conventional "indirect" method firstly reconstructs wavelength-specific absorption and scattering distributions and then deduces the chromophore concentrations and scattering components [94]. While a "direct" spectrally-constraint method integrates the spectral information into the sensitivity matrices to directly recover the chromophore concentrations and scattering parameters [7, 90-92, 98-99, 103-105]. Note that the efficacies of both methods are ultimately bounded by the determination of the gradient of the spectrally variant optical properties with respect to the chromophore concentrations and scattering parameters. However, as the direct method has less unknown values than the indirect method does, the inverse problem in the direct method is better conditioned. Therefore it is well expected [7, 91-92, 98, 104] that the direct method outperforms the indirect method in terms of CNR and inter-parameter cross-talk. In light of this, the "direct" reconstruction method is adopted in the simulations of this study for multi-spectral optical tomography reconstruction.

The rest of the paper is structured to the following sections for the comparison of DC, DC-excluded FD, and DC-included FD measurements under the same spectral-constraint: analytical derivation of the PRULs, numerical implementation of the derived PRULs, ranking of the spectral-*priors* being implemented for the PRUL analyses, and finite-element-based simulation to validate the proceeding numerical evaluations. The simulation study will demonstrate that: 1) the ranking of the wavelength sets given by the analytical approach is correct; 2) for a given set of tissue chromophores and spatially homogenous detection sensitivity,

the DC-only outperforms FD in NCR; however, as the spatial sensitivity becomes significantly non-uniform, the phase information in FD measurement shows robustness for reconstruction versus DC-only reconstruction; 3) including DC in FD reconstruction generally improves the outcome than neglecting it.

4.2 Parameter Recovery Uncertainty Level (PRUL) in Multi-spectral Measurement

4.2.1 General expression of the PRUL

For a field point at a distance d from the source in an infinite homogenous diffusive medium, we define $U_{DC}(d, \lambda)$, $U_{AC}(d, \lambda)$ and $\Phi(d, \lambda)$ as the wavelength-specific DC, AC and phase measurands. For two field points located d_1 and d_2 from the source, the differences in their DC, AC, and phase-shift denoted by $\delta(\lambda)$, $\alpha(\lambda)$ and $\varphi(\lambda)$, respectively, can be expressed as[81, 102] :

$$\delta(\lambda) = \ln\left(\frac{d_2}{d_1}\frac{U_{DC}(d_2,\lambda)}{U_{DC}(d_1,\lambda)}\right) = -\rho\cdot\sqrt{\frac{\mu_a(\lambda)}{D(\lambda)}} \qquad \text{(4.1-DC)}$$

$$\alpha(\lambda_i) = \ln\left(\frac{d_2}{d_1}\frac{U_{AC}(d_2,\lambda)}{U_{AC}(d_1,\lambda)}\right) = -\rho\cdot\sqrt{\frac{\mu_a(\lambda)}{2D(\lambda)}\left(\sqrt{1+\frac{\omega^2}{v^2\mu_a^2(\lambda)}}+1\right)} \qquad \text{(4.1-AC)}$$

$$\phi(\lambda) = \Phi(d_2,\lambda) - \Phi(d_1,\lambda) = \rho\cdot\sqrt{\frac{\mu_a(\lambda)}{2D(\lambda)}\left(\sqrt{1+\frac{\omega^2}{v^2\mu_a^2(\lambda)}}-1\right)} \qquad \text{(4.1-PHS)}$$

where $\rho = |d_1-d_2|$, ω is the angular modulation frequency, v is the speed of light in the medium, and

$$\mu_a(\lambda) = \sum_i \log(10)\varepsilon_i(\lambda)c_i \quad \text{(the "log" denotes the natural logarithm)} \qquad (4.2\text{-}\mu_a)$$

$$\mu_s'(\lambda) = A\lambda^{-b} \qquad (4.2\text{-}\mu_s')$$

$$D(\lambda) = \left\{3[\mu_a(\lambda)+\mu_s'(\lambda)]\right\}^{-1} \qquad (4.2\text{-}D)$$

are the absorption, reduced scattering and diffusion coefficients of the medium, respectively. In equ. (4.2), $\varepsilon_i(\lambda)$ is the extinction coefficient of chromophore i at wavelength λ [106], A is the scattering amplitude and b is the scattering power [7, 91].

The standard deviations, denoted by σ_δ, σ_α and σ_φ, respectively, of the differences of the measurands δ, α and φ, in fact represent the measurement uncertainties [81, 102]. The translation of the measurement uncertainties into variations in the reconstructed spectrally-constrained optical properties may be modeled by

$$\sigma_{x_j} = \sqrt{\left(\frac{\partial x_j}{\partial M(\lambda)}\right)^2 \cdot \sigma^2_{M(\lambda)}} = \left|\frac{\partial x_j}{\partial \mu(\lambda)} \cdot \frac{\partial \mu(\lambda)}{\partial M(\lambda)}\right| \cdot \sigma_{M(\lambda)} = \left|\frac{\partial x_j}{\partial \mu(\lambda)}\right| \cdot \sigma_{\mu(\lambda)} \tag{4.3}$$

where x represents the set of chromophore concentrations, scattering amplitude and scattering power, M represents the set of δ, α and φ, and $\mu(\lambda)$ represents the set of absorption and reduced scattering coefficients. Note that the $\sigma_{\mu(\lambda)}$ has already been given in tables II and IV of [102], so only $\partial x/\partial \mu$ needs to be derived in this study. The following section only show the crtical steps during the derivation, detailed deduction can be found in the appendices.

4.2.2The PRULs of chromophore concentration

By expressing equ. (2-μ_a) in matrix form as following:

$$\begin{bmatrix} \mu_a(\lambda) \\ \mu_a(\lambda) \\ \vdots \\ \mu_a(\lambda) \end{bmatrix}_{m\times 1} = \log(10) \cdot \begin{bmatrix} \varepsilon_1(\lambda_1) & \varepsilon_2(\lambda_1) & \cdots & \varepsilon_n(\lambda_1) \\ \varepsilon_1(\lambda_2) & \varepsilon_2(\lambda_2) & \cdots & \varepsilon_n(\lambda_2) \\ \vdots & \vdots & \ddots & \vdots \\ \varepsilon_1(\lambda_m) & \varepsilon_2(\lambda_m) & \cdots & \varepsilon_n(\lambda_m) \end{bmatrix}_{m\times n} \times \begin{bmatrix} c_1 \\ c_2 \\ \vdots \\ c_n \end{bmatrix}_{n\times 1} \tag{4.4}$$

one has the gradient of chromophore concentration with respect to the absorption coefficients as:

$$\frac{\partial \vec{c}_{n\times 1}}{\partial (\vec{\mu}_a)_{m\times 1}} = \log^{-1}(10) \cdot [(\vec{\varepsilon}^T)_{n\times m} \vec{\varepsilon}_{m\times n}]^{-1} (\vec{\varepsilon}^T)_{n\times m} = \begin{bmatrix} \frac{\partial c_1}{\partial \mu_a(\lambda_1)} & \frac{\partial c_1}{\partial \mu_a(\lambda_2)} & \cdots & \frac{\partial c_1}{\partial \mu_a(\lambda_m)} \\ \frac{\partial c_2}{\partial \mu_a(\lambda_1)} & \frac{\partial c_2}{\partial \mu_a(\lambda_2)} & \cdots & \frac{\partial c_2}{\partial \mu_a(\lambda_m)} \\ \vdots & \vdots & \ddots & \vdots \\ \frac{\partial c_n}{\partial \mu_a(\lambda_1)} & \frac{\partial c_n}{\partial \mu_a(\lambda_2)} & \cdots & \frac{\partial c_n}{\partial \mu_a(\lambda_m)} \end{bmatrix}_{n\times m} \tag{4.5}$$

Combining equ. (4.5) with σ_{μ_a} found in [102], the PRUL of the chromophore concentration becomes:

$$(\bar{\sigma}_c)_{n\times 1} = \left|\frac{\partial \vec{c}_{n\times 1}}{\partial (\vec{\mu}_a)_{m\times 1}}\right|_{n\times m} \cdot (\bar{\sigma}_{\mu_a(\lambda)})_{m\times 1} \tag{4.6}$$

4.2.3 The PRULs of scattering amplitude and scattering power

Take the logarithm of equ. (4.2- μ_s') as

$$\log \mu_s' = \log A + (-b)\log \lambda \tag{4.7}$$

and convert equ.(4.7) to the matrix form of:

$$\begin{bmatrix} \log[\mu_s'(\lambda_1)] \\ \log[\mu_s'(\lambda_2)] \\ \cdots \\ \log[\mu_s'(\lambda_m)] \end{bmatrix}_{m\times 1} = \begin{bmatrix} 1 & \log\lambda_1 \\ 1 & \log\lambda_2 \\ \cdots & \cdots \\ 1 & \log\lambda_m \end{bmatrix}_{m\times 2} \times \begin{bmatrix} \log A \\ (-b) \end{bmatrix}_{2\times 1} \tag{4.8}$$

one has:

$$\left(\frac{\partial \log A}{\partial \log \mu_s'(\lambda_i)}\right)_{1\times m} = \frac{1}{m\sum_{i=1}^{m}\log^2(\lambda_i) - [\sum_{i=1}^{m}\log(\lambda_i)]^2} \cdot \left(\begin{bmatrix} \sum_{i=1}^{m}\log^2(\lambda_i) - \log(\lambda_1)\sum_{i=1}^{m}\log(\lambda_i) \\ \sum_{i=1}^{m}\log^2(\lambda_i) - \log(\lambda_2)\sum_{i=1}^{m}\log(\lambda_i) \\ \cdots \\ \sum_{i=1}^{m}\log^2(\lambda_i) - \log(\lambda_m)\sum_{i=1}^{m}\log(\lambda_i) \end{bmatrix}^T \right)_{1\times m} \tag{4.9}$$

$$\left(\frac{\partial b}{\partial \log \mu_s'(\lambda_i)}\right)_{1\times m} = \frac{1}{m\sum_{i=1}^{n}\log^2(\lambda_i) - [\sum_{i=1}^{n}\log(\lambda_i)]^2} \cdot \left(\begin{bmatrix} \sum_{i=1}^{m}\log(\lambda_i) + m\cdot\log(\lambda_1) \\ \sum_{i=1}^{m}\log(\lambda_i) + m\cdot\log(\lambda_2) \\ \cdots \\ \sum_{i=1}^{m}\log(\lambda_i) + m\cdot\log(\lambda_m) \end{bmatrix}^T \right)_{1\times m} \tag{4.10}$$

The PRULs of scattering amplitude and scattering power are then expressed by:

$$\sigma_A = \left|\frac{\partial A}{\partial \log A}\cdot\frac{\partial \log A}{\partial \log \mu_s'(\lambda)}\cdot\frac{\partial \log \mu_s'(\lambda)}{\partial \mu_s'(\lambda)}\right| \cdot \sigma_{\mu_s'(\lambda)} = A\cdot\left|\frac{\partial \log A}{\partial \log \mu_s'(\lambda)}\right| \cdot \frac{\sigma_{\mu_s'(\lambda)}}{\mu_s'(\lambda)} \tag{4.11}$$

$$\sigma_b = \left|\frac{\partial b}{\partial \log \mu_s'(\lambda)}\cdot\frac{\partial \log \mu_s'(\lambda)}{\partial \mu_s'(\lambda)}\right| \cdot \sigma_{\mu_s'(\lambda)} = \left|\frac{\partial b}{\partial \log \mu_s'(\lambda)}\right| \cdot \frac{\sigma_{\mu_s'(\lambda)}}{\mu_s'(\lambda)} \tag{4.12}$$

where ($\sigma_{\mu s'(\lambda)}/\mu_s'(\lambda)$) was available in [102].

4.2.4 Qualitative evaluation of the PRULs between scattering amplitude and scattering power

A qualitative evaluation of equ.s (4.11) and (4.12) can estimate which one, between scattering amplitude and scattering power, is less prone to measurement uncertainties. Neglecting the common factor $\sigma_{\mu s'(\lambda)}/\mu_s$' in equ.s (4.11) and (4.12) as well as the equal denominators in equ.s (4.9) and (4.10), only the elements in the 1×m matrices in equ.s (4.9) and (4.10) are to be compared. Within the NIR spectral range between 0.6μm and 1μm, i.e, $\lambda \in [0.6,1]$ with the unit of μm, one has $-1 \leqslant \log(\lambda_i) \leqslant 0 \leqslant \log^2(\lambda_i) \leqslant 1$ for the first term in each element and thus

$$\sum \log(\lambda_i) < \sum \log^2(\lambda_i) < 0. \tag{4.13}$$

For the second terms of $-\log(\lambda_m)\cdot\sum\log(\lambda_i)$ and $m\cdot\log(\lambda_m)$, apparently $m > -\sum\log(\lambda_i) > 0$ and thus

$$m\cdot\log(\lambda_m) < -\log(\lambda_m)\cdot\sum\log(\lambda_i) < 0 \tag{4.14}$$

Summing the inequalities (4.13) and (4.14) leads to

$$|\sum\log(\lambda_i) + m\cdot\log(\lambda_m)| > |\sum\log^2(\lambda_i) - \log(\lambda_m)\cdot\sum\log(\lambda_i)| \tag{4.15}$$

which implies that the PRULs of the scattering power should exceed that of scattering amplitude, or the scattering power is more prone to noise than the scattering amplitude is.

4.3 Numerical Evaluation of PRULs in Multi-spectral Measurement

4.3.1 Sets of spectral-prior used for PRUL evaluation

We implemented 3 sets of wavelengths used in [7] for spectral-*prior* for quantitative analyses of PRULs in multi-spectral measurements. Each of the spectral-*prior* sets contains 5 wavelengths as shown in Fig.4.1 and Table 4.1. The set 1 expands 186nm from 740nm to 926nm. The set 2 expands 240nm from 650nm to 890nm. The set 3 expands 280nm from 650nm to 930nm.

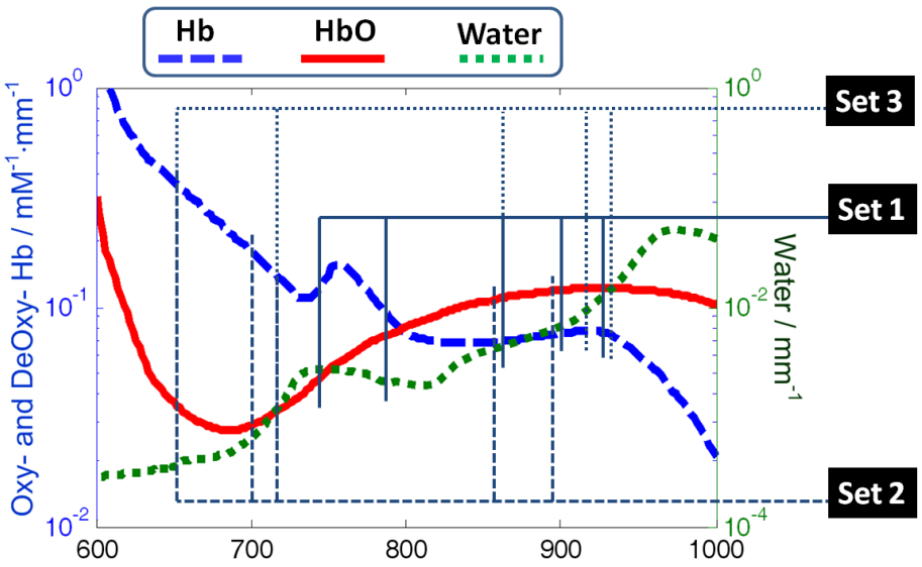

Fig.4.1 Illustration of the wavelength sets

4.3.2 Criteria of wavelength optimization in the context of minimizing PRULs

Wavelength optimization for spectrally-constrained optical tomography would naturally reduce the uncertainties in the reconstruction. One approach to optimize is to have a greater set of denominators in equ.s (4.5), (4.9) and (4.10). For the scattering aspect in equ.s (4.9) and (4.10), several random attempts show that the value of $\left| m\sum_{i=1}^{m}\log^2(\lambda_i) - [\sum_{i=1}^{m}\log(\lambda_i)]^2 \right|$ stays in a narrow range of [0.1, 1]. However, for equ. (4.5), the determinant of $\varepsilon^T\varepsilon$ varies in several orders depending upon the wavelengths, which is however not unexpected because the similarities between the row-vectors in matrix ε could induce rank deficiency. Corlu et al. [7] and Eames et al. [105] indicated such issue of rank deficiency and recommended to construct the sensitivity matrix with small residual numbers. From another perspective, however, one could associate the determinant of a matrix with the area bounded by the row-vector of the matrix. This suggests that maximizing the determinant of the matrix $\varepsilon^T\varepsilon$ will likely decrease the similarities among the row-vectors in the matrix ε and minimize its rank deficiency. The study in [105] also indicates that within the sensitivity matrix, less variation among the sub-matrices with respect to each category of reconstruction parameters (such as chromophore concentrations and scattering parameters)

renders more favorable reconstruction. This study thereby includes the magnitude uniformity of $\partial x/\partial M$ in equ. (3) as one of the criteria of wavelength optimization.

Optimization methods in [7, 103] appraise the residue and condition numbers of sensitivity matrix that includes $n_{source\text{-}detector\text{-}pair} \times n_{measurement\text{-}wavelength} \times n_{nodes}$ terms. The method introduced in this study examines equ.s (4.5), (4.11) and (4.12), and the total evaluation number is $n_{source\text{-}detector\text{-}pair} \times n_{measurement\text{-}wavelength}$, which is n_{nodes} times less in the computation needed than the methods introduced in (8, 20). Table 4.1 illustrates the outcome when applying our criteria to the three sets of spectral-*prior*, after neglecting the common terms $|\partial\mu(\lambda)/\partial M(\lambda)|\cdot\sigma_{M(\lambda)}$ in equ. (4.3). Since the optimization is in favor of large denominator of the determinant and small variation among the gradient values, the set 3 stands out as the best. The set 1 significantly outperforms the set 2 in absorption part, whereas the set 2 moderately outperforms the set 1 in scattering part. The overall ranking among the three sets of spectral *priors* is thus (3, 1, 2), which agrees with the experimental results demonstrated in [7].

Table 4.1 Wavelength sets to be examined and comparison of PRULs evaluation with the analytical solutions

Set	Wavelengths / nm	Absorption Part		Scattering Part	
		Determinant of denominator: ($\varepsilon^T\varepsilon$)	Standard deviation of extinction coefficients dev(ε)	Determinant of denominator	Standard deviation of $\partial x/\partial M(\lambda)$
(2)	650,700,716,860,890	2.58e-7	388.0	0.37	0.67
(1)	740,788,866,902,926	8.18e-7	63.7	0.18	1.03
(3)	650,716,866,914,930	1.30e-5	63.8	0.53	0.45

4.3.3 Quantitative evaluations of relative PRULs

To quantitatively evaluate the PRULs in equ.s (4.6), (4.11) and (4.12), we assign the background chromophore concentrations and scattering parameters as [105]: C_{HbO}=C_{Hb}=0.01mM, C_{H2O}=40% and A=b=1. The preset properties of the anomaly are approximately two-folds of those assigned to the background, as: C_{HbO_anom} =0.023mM, C_{Hb_anom} = 0.023mM, C_{H2O_anom} =80% A_{anom}=2, and b_{anom}=2. The relative uncertainties of all measurement differences are assumed as 1% [81], that is: $\frac{\sigma^2_{\delta(\lambda)}}{\delta^2(\lambda)} = \frac{\sigma^2_{\alpha(\lambda)}}{\alpha^2(\lambda)} = \frac{\sigma^2_{\phi(\lambda)}}{\phi^2(\lambda)} = (1\%)^2$. Besides, for the range of wavelengths and modulation frequency commonly utilized in optical tomography, one could approximate $\frac{\alpha^2(\lambda)+\phi^2(\lambda)}{\alpha^2(\lambda)-\phi^2(\lambda)}$ ($= \sqrt{1+\frac{\omega^2}{v^2\mu_a^2(\lambda)}}$) as 1. With these necessary pre-conditioning, table 4.2 shows the quantitative evaluations of PRULs in equ.s (4.6), (4.11) and (4.12), and normalizes the PRULs by the pre-set contrasts of the anomaly. Such normalized values relate to the Noise-to-Contrast Ratios (NCR) in the reconstruction. In table 4.2, the absolute NCRs are further normalized by those of DC-only in each column, the absorption part is further normalized by NCRs of the hemoglobin in each row, and the scattering part is normalized by NCRs of the scattering amplitude in each row. Such normalizations more explicitly indicate the rankings of NCR among three measurement conditions for each reconstruction parameter.

Table 4.2 Analytical evaluation of parameter reconstruction uncertainty levels normalized by target contrasts (NCRs)

		HbO / mM			Hb / mM			H2O / %			A			b		
Set	Measure-ment	Abs.	Column--wise Norm.	Row-wise Norm.	Abs.	Column-wise Norm.	Row-wise Norm.	Abs.	Column-wise Norm.	Row-wise Norm.	Abs.	Column-wise Norm.	Row-wise Norm.	Abs.	Column-wise Norm.	Row-wise Norm.
(1)	DC	0.04	1	2.0	0.02	1	1	0.03	1	1.4	0.01	1	1	0.05	1	5.2
	AC+PHS	0.06	1.41	2.0	0.03	1.41	1	0.04	1.41	1.4	0.02	1.41	1	0.08	1.41	5.2
	DC+AC+PHS	0.11	2.5	2.0	0.05	2.45	1	0.07	2.45	1.4	0.02	1.41	1	0.08	1.41	5.2
(2)	DC	0.127	1	9.4	0.014	1	1	0.13	1	9.3	0.01	1	1	0.04	1	3.3
	AC+PHS	0.180	1.4	9.4	0.019	1.41	1	0.18	1.41	9.3	0.02	1.41	1	0.05	1.41	3.3
	DC+AC+PHS	0.311	2.5	9.4	0.033	2.45	1	0.31	2.45	9.3	0.02	1.41	1	0.05	1.41	3.3
(3)	DC	0.054	1	5.4	0.010	1	1	0.03	1	3.2	0.01	1	1	0.03	1	3.9
	AC+PHS	0.076	1.4	5.4	0.014	1.41	1	0.05	1.41	3.2	0.01	1.41	1	0.04	1.41	3.9
	DC+AC+PHS	0.132	2.5	5.4	0.025	2.45	1	0.08 -	2.45	3.2	0.01 -	1.41	1	0.04 -	1.41	3.9

From the Row-wise Norm. in table 4.2, one would expect that DC reconstruction has the least NCRs and accordingly, the least relative uncertainties in the reconstruction. One would also expect that including DC measurements in FD at several cases does not necessarily increase the reconstruction NCRs. From the Column-wise Norm. in tables 4.2, one would also expect that for the three sets of wavelength, $NCR_{C\_Hb} < NCR_{C\_H2O} < NCR_{C\_HbO}$ for the absorption aspect and $NCR_A < NCR_b$ for the scattering aspect.

4.4 Simulation Studies

4.4.1 Synthetic model and geometries considered

The synthetic study is based on NIRFAST package [86]. The forward model computes photon diffusion at each wavelength by:

$$\left(-\frac{\mu_a(\vec{r},\lambda)}{D(\vec{r},\lambda)}+\frac{i\omega}{vD(\vec{r},\lambda)}\right)U(\vec{r},\omega,\lambda)+\nabla^2U(\vec{r},\omega,\lambda)=-\frac{S(\vec{r},\omega,\lambda)}{D(\vec{r})} \tag{4.16}$$

where $U(\vec{r},\omega,\lambda)$ is the photon fluence of wavelength λ at frequency ω (for DC simply assigning ω=0) for position $\vec{r}$, and $S(\vec{r},\omega,\lambda)$ is the source term. The Robin type boundary condition is assigned as:

$$U(\vec{r}_0,\omega)-2DA\hat{n}_0\cdot\nabla U(\vec{r}_0,\omega)=0 \tag{4.17}$$

where $\vec{r}_0$ denotes the boundary node; A is the coefficient accounting for the refractive index mismatch; and $\hat{n}_0$ is the outgoing normal vector. The sensitivity or Jacobian matrix is constructed according to the measurands [102] as:

$$J=\begin{bmatrix} DC \\ AC \\ PHS \end{bmatrix}=\begin{bmatrix} \frac{\partial \ln U_{DC}(\lambda_1)}{\partial x} & \frac{\partial \ln U_{DC}(\lambda_2)}{\partial x} & \cdots & \frac{\partial \ln U_{DC}(\lambda_m)}{\partial x} \\ \frac{\partial \ln |U_{AC}(\lambda_1)|}{\partial x} & \frac{\partial \ln |U_{AC}(\lambda_2)|}{\partial x} & \cdots & \frac{\partial \ln |U_{AC}(\lambda_m)|}{\partial x} \\ \frac{\partial \Phi_{AC}(\lambda_1)}{\partial x} & \frac{\partial \Phi_{AC}(\lambda_2)}{\partial x} & \cdots & \frac{\partial \Phi_{AC}(\lambda_m)}{\partial x} \end{bmatrix} \tag{4.18}$$

where *x* represents the parameters to be reconstructed, including chromophore concentrations and scattering amplitude and scattering power.

Two imaging geometries are evaluated as shown in Fig.4.2. Fig.4.2(a) shows a circular geometry with the medium enclosed by a ring-applicator of 86mm in diameter [91, 103, 105]. Fig.4.2(b) includes a circular applicator array of 20mm in diameter that is enclosed by the medium, and the medium is bounded within a circle of 40mm from the applicator surface. In both geometries, 16 optodes are evenly distributed along the circumference, and each optode functions sequentially as the source with the other 15 optodes being the detection channels. The imaging geometry in Fig.4.2(a) is discretized into 3418 finite-elements with 1785 nodes. The imaging geometry in Fig.4.2(b) is segmented to 3748 elements with 1968 nodes. The two geometries have

noticeably different sensitivity distributions along the depth from the applicator surface into the medium, as shown in Fig.4.2(c). It will be shown that such difference in sensitivity affects the outcome of reconstruction.

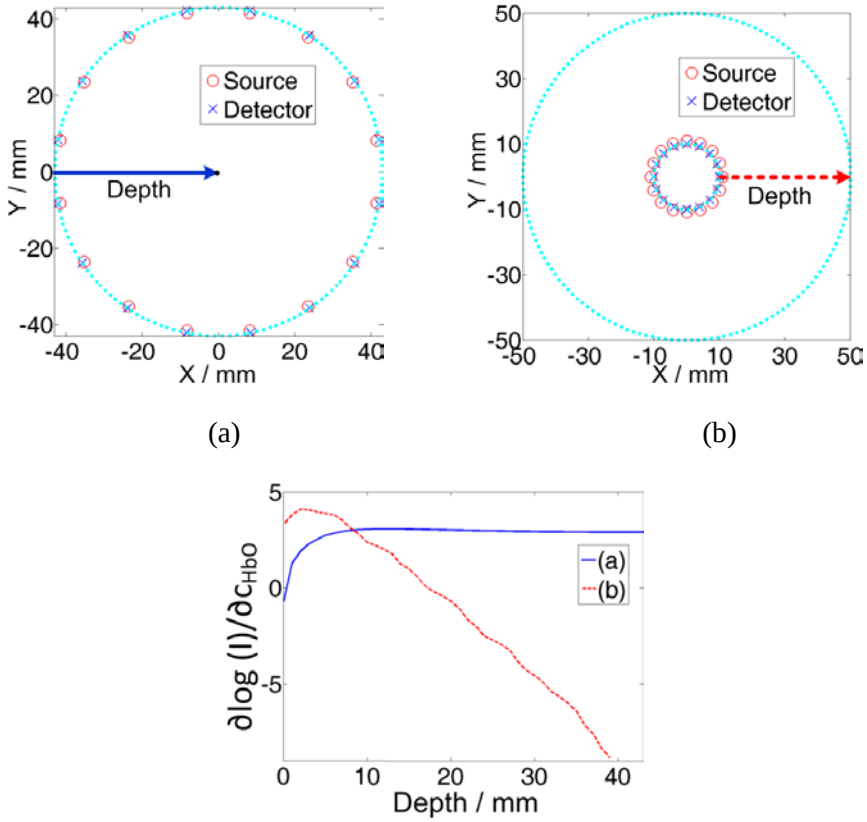

Fig.4.2 Simulation geometries (a) Large applicator enclosing the imaging volume. The FEM mesh has a radius of 43mm and includes 1785 nodes and 3418 elements (b) Small applicator enclosed by the imaging volume. The geometry has an inner radius of 10mm. The FEM mesh includes 1968 nodes and 3748 elements. (c) Sensitivity plot ($\partial \ln I/\partial c_{HbO}$) along the depth direction into the medium. Spatial sensitivity decay in (a) is less significant than that in (b).

The optical properties employed in the simulations are identical to those used for tables 4.2, and ananomaly could have one or multiple contrasts of the properties. Two sets of simulations are conducted on both imaging geometries. One set simulates five targets with

independent contrasts, and the other set studies two closely positioned targets of identical properties. White noise at 1% is added to the forward data before applying the Levernberg-Marquardt algorithm as the inverse solver.

4.4.2 Simulation Results

4.4.2.1 Exterior imaging geometry—reconstructing targets with independent contrasts

The set targets are five 8mm-radius contrast-regions located 25 mm away from the center of the geometry with 0.4π angular separation, as shown in the column set of Fig.4.3. Each of the five regions differs from the rest in its contrast. Fig.4.3 shows the reconstruction results for the three sets of spectral-*prior*s, and Table 4.4 demonstrates the maximum values of each variable within the target regions and the percentage error of the contrast. In terms of the overall reliability of quantitative reconstruction, the set 3 show in in Fig.4.3(c) outperforms the other two. Next to the set 3 is the set 1 shown in Fig.4.3(a), which in DC reconstruction underestimates HbO and Hb yet overestimates A and b due to cross-coupling. The set 2 shown in Fig.4.3(b) is the least accurate as it has the highest level of cross-coupling between the HbO and H_2O concentrations in FD reconstruction. For most cases shown in Fig.4.3 and table 4.3, one could notice that DC reconstruction outperforms the other two methods in resolving the targets.

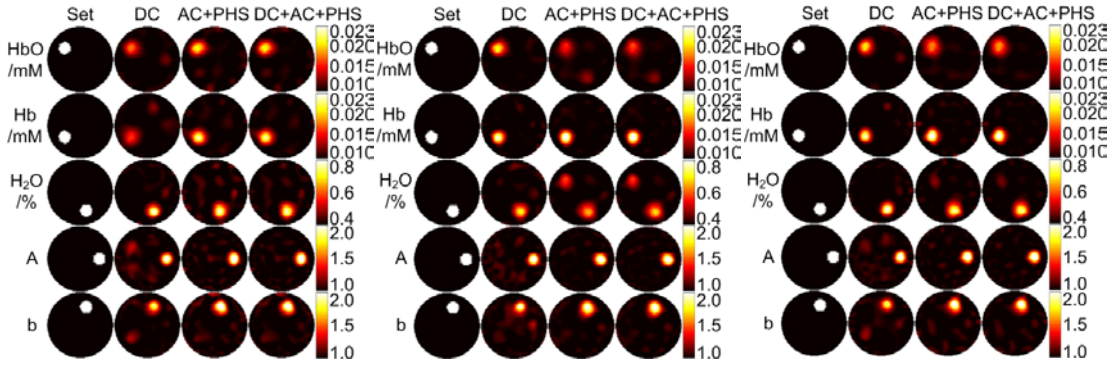

(a) (b) (c)

Fig.4.3 Synthetic study on five targets with independent contrasts in image geometry (a) in Fig.4.2. (a)(b)(c) are the results for the wavelength set (1)(2)(3)

in table I, respectively. (a) Second best: slight cross-coupling between HbO/A and between Hb/b recovery in column DC. (b) Worst: Severe cross-coupling between HbO and H_2O. (c) Best: minimal cross-coupling and target underestimation. Note: target overestimation is not visible because of uniform color bars. Look for absolute values in table 4.3.

Table 4.3 Target accuracy in Fig.4.3

	Data	HbO / mM		Hb / mM		H2O / %		A		b	
		Abs.	Err. / %	Abs.	Err. / %	Abs.	Err. / %	Abs.	Err. / %	Abs.	Err. / %
	Set Values	2.3e-2		2.3e-2		0.80		2.0		2.0	
(1)	DC	1.7e-2	-46	1.6e-2	-55	0.82	5	2.2	21	1.9	-9
	AC+PHS	2.0e-2	-23	2.3e-2	-2	0.81	2	2.4	39	2.3	30
	DC+AC+PHS	2.0e-2	-24	2.2e-2	-6	0.80	0.4	2.3	34	2.2	23
(2)	DC	2.0e-2	-21	2.4e-2	4	0.72	-21	2.4	40	2.1	7
	AC+PHS	1.6e-2	-56	2.6e-2	24	0.67	-33	2.3	26	2.1	6
	DC+AC+PHS	1.7e-2	-48	2.7e-2	27	0.69	-27	2.2	23	2.1	10
(3)	DC	2.0e-2	-25	2.3e-2	1	0.83	8	2.3	33	1.9	-11
	AC+PHS	1.8e-2	-42	2.5e-2	16	0.78	-6	2.4	45	2.2	19
	DC+AC+PHS	1.8e-2	-39	2.5e-2	18	0.77	-8	2.4	39	2.2	17

Table 4.4 lists the NCRs of the reconstruction results in Fig.4.3, that is, the standard deviations (σ_x) of the reconstructed background values normalized by the maximum target contrasts. The σ_x values are calculated by excluding the areas co-centric to the targets but with the radii twice as those of the target regions. Similar to those in table II, the NCRs in Table 4.4 are normalized by those of DC-only in each column. Similarly in each row of Table 4.4, the absorption part is normalized by NCRs of the Hb and the scattering part is normalized by NCRs of the A. The row-wisely normalized NCRs in Table 4.4 unanimously show $NCR_{C\_Hb} < NCR_{C\_H2O} < NCR_{C\_HbO}$ for the absorption part and $NCR_A < NCR_b$ for the scattering part, which

agree with those in table II. For column-wisely normalized NCRs, in the sets 1 and 3, both table II and IV indicate that the ratio of AC+PHS over DC stays within the range of [1, 2]. The artifact levels of DC+AC+PHS reconstruction are shown always lower than those of AC+PHS and sometimes lower than those of DC. Similar observations were reported in [102], and collectively they conclude that DC component is indeed not-redundant in FD measurements, therefore neglecting DC would degrade the accuracy of FD reconstruction. In the set 2, the NCRs are slightly lower in FD than in DC-only. This implies that FD measurement is more robust in the case of less desirable spectral *prior*.

Table 4.4 Absolute and normalized NCRs of the images in Fig.4.3

Set	Measure-ment	HbO / mM			Hb / mM			H2O / %			A			b		
		Abs.	Column -wise Norm	Row -wise Norm	Abs.	Column -wise Norm.	Row -wise Norm	Abs.	Column -wise Norm	Row -wise Norm	Abs.	Column -wise Norm	Row -wise Norm	Abs.	Column -wise Norm.	Row -wise Norm
(1)	DC	0.066	1	1.3	0.052	1	1	0.039	1	0.7	0.022	1	1	0.051	1	2.3
	AC+PHS	0.072	1.6	2.1	0.035	1.4	1	0.066	1.7	1.9	0.038	2.0	1	0.057	1.6	1.5
	DC+AC+PHS	0.058	1.2	1.8	0.033	1.3	1	0.049	1.2	1.5	0.032	1.6	1	0.047	1.3	1.4
(2)	DC	0.048	1	1.4	0.033	1	1	0.063	1	1.9	0.028	1	1	0.043	1	1.5
	AC+PHS	0.054	0.6	2.2	0.025	0.9	1	0.049	0.7	2.0	0.025	0.8	1	0.037	0.9	1.5
	DC+AC+PHS	0.049	0.7	2.1	0.023	0.9	1	0.047	0.7	2.0	0.027	0.8	1	0.036	0.9	1.3
(3)	DC	0.049	1	1.9	0.026	1	1	0.040	1	1.5	0.026	1	1	0.038	1	1.5
	AC+PHS	0.072	1.1	1.6	0.044	2.0	1	0.047	1.0	1.1	0.024	1.0	1	0.050	1.8	2.1
	DC+AC+PHS	0.052	0.9	1.6	0.033	1.5	1	0.037	0.8	1.1	0.020	0.8	1	0.040	1.4	2.0

4.4.2.2 Exterior imaging geometry—resolving two closely positioned identical targets

In Fig.4.4, two identical targets of 8-mm in radius are embedded 25mm from the center and the angular separation between the targets is $\pi/4$. Each target has all five contrast properties as previously defined. Fig.4.4 indicates that cross-coupling is more severe in DC as it underestimates the concentration of Hb and H_2O. To explicitly compare how well the targets are

resolved, the parameter contours along the concentric circle of the imaging geometry and across the targets (marked with gold dotted loops in Fig.4.4) are plotted in Fig.4.5. Figures 4 and 5 show that the absolute target properties are the least accurate in DC reconstruction. However, the two targets are always better resolved in DC than in FD. Table 4.5 lists the ratios of target-to-valley contrast over target-to-background contrast (both contrasts are illustrated in the upper-left subFig.4.of Fig.4.5). Larger ratios indicate better identification of the targets. It is shown that in most cases the targets are resolved the clearest in DC.

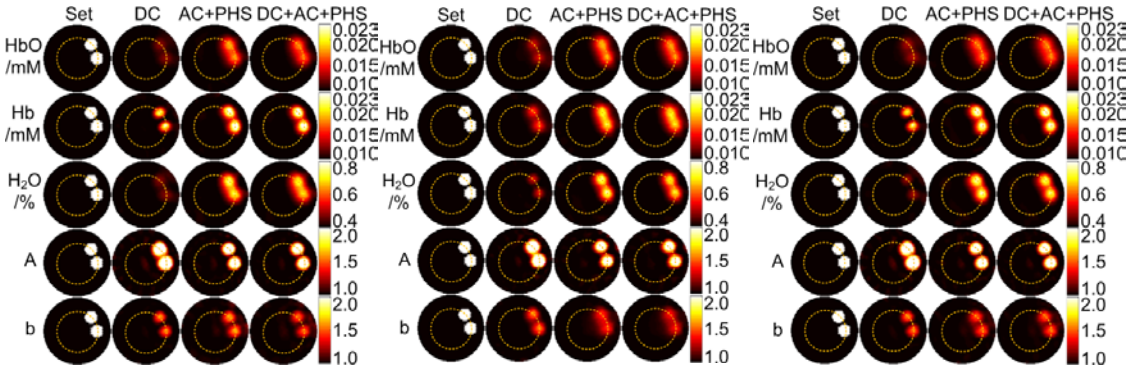

(a) (b) (c)

Fig.4.4 Synthetic study on two targets with all five parameter contrasts in image geometry (a) in Fig.4.2. (a)(b)(c) are the results for the wavelength set (1)(2)(3) in table I, respectively. Cross-coupling are severe in all reconstructed parameters. (a) Second best: targets are inseparable in H_2O distribution recovery by FD reconstructions. (b) Worst: targets are inseparable in Hb and b distribution recovery by FD reconstructions. (c) Best: targets are separated in all cases.

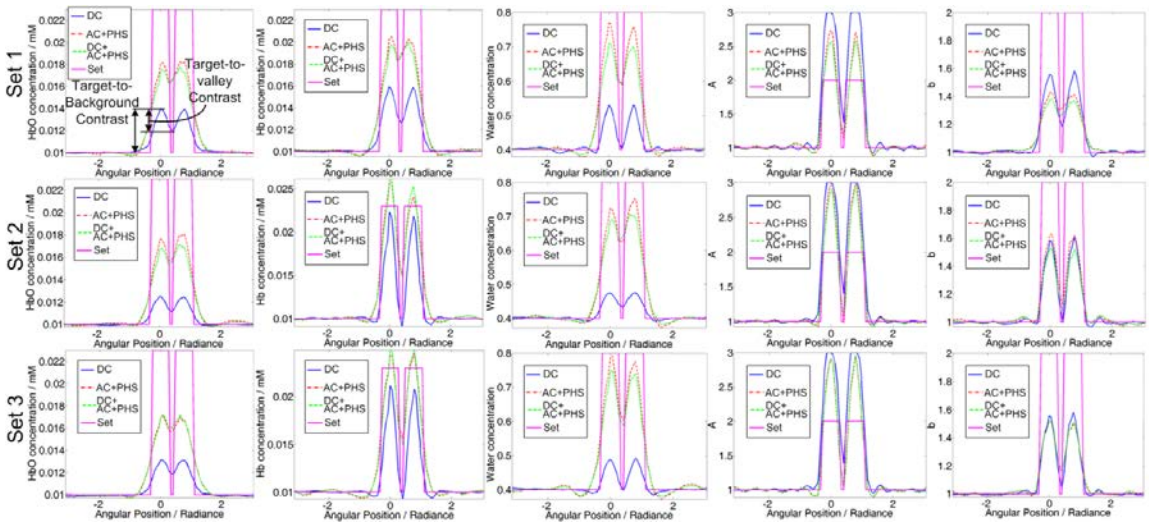

Fig.4.5 Parameter contour plots along the gold dash lines in Fig.4.4. The upper left subfigure denotes the target-to-valley contrast and target-to-background contrast. DC reconstruction shows relatively deeper contrast valleys between the targets for most cases.

Table 4.5 Comparison of target separation in Fig.4.5

Note: Data are calculated as the ratio of the contrast of the valley between the two targets over the target contrast

	Data	HbO	Hb	H_2O	A	b
(1)	DC	0.76	0.56	0.98	0.81	0.68
	AC+PHS	0.15	0.18	0.47	0.93	0.27
	DC+AC+PHS	0.36	0.15	0.35	0.87	0.30
(2)	DC	0.54	1.07	0.57	0.80	1.01
	AC+PHS	0.25	0.65	0.31	1.01	0.80
	DC+AC+PHS	0.20	0.67	0.21	0.97	0.85
(3)	DC	0.42	1.06	1.01	0.81	0.93
	AC+PHS	0.19	0.61	0.46	0.99	0.67
	DC+AC+PHS	0.18	0.66	0.52	0.99	0.70

4.4.2.3 Interior imaging geometry—reconstructing targets with independent contrasts

The five targets of 8mm in radius are evenly distributed in the azimuthal direction and placed 10 mm away from the inner boundary of the imaging geometry, as is shown in the column Set of Fig.4.6. The contrasts of the targets are identical to those in Fig.4.3. The recovered images for the 3 sets of spectral priors are displayed in Fig.4.6(a), (b), and (c), respectively. The target recovery accuracy and NCRs are compared in Table 4.6 and 4.7. Fig.4.6 shows that all targets are recovered at regions shallower than the set regions, due to the significantly depth-dependent sensitivity distribution that peaks in the proximity of the applicator as shown in Fig.4.2(c). The performance ranking of the three wavelength set as [3, 1, 2] again agrees with the analytical prediction. Table 4.6 further demonstrated that FD reconstruction outperforms DC as phase information improves target recovery in imaging geometries with noticeable variation of the spatial sensitivity. The NCR rankings in Table 4.8 are in most cases similar to that in Table 4.5, as $NCR_{C\_Hb} < NCR_{C\_H2O} < NCR_{C\_HbO}$ and $NCR_A < NCR_b$.

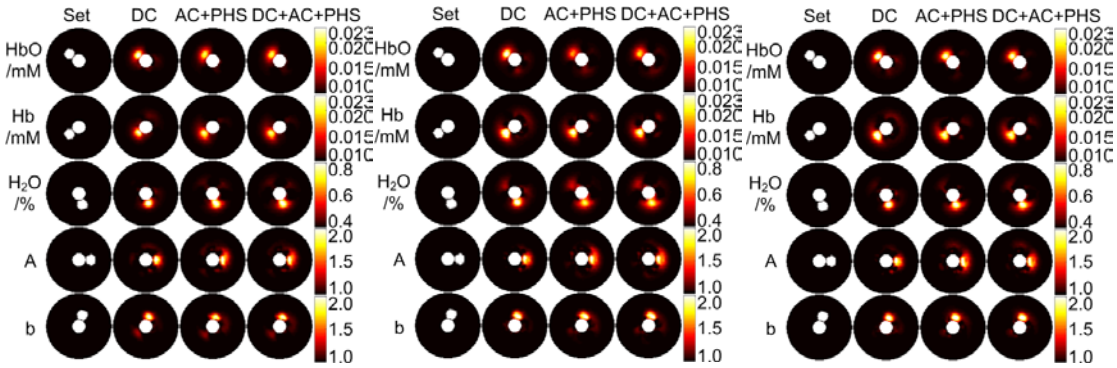

Fig.4.6 Synthetic study on five targets with independent parameter contrasts in image geometry (b) in Fig.4.2. (a)(b)(c) are the results for the wavelength set (1)(2)(3) in table I, respectively. (a) Second Best: slight cross-coupling between Hb and b. (b) Worst: severe cross-coupling between HbO and H_2O. (c) Best: barely any cross-coupling.

Table 4.6 Target accuracy in Fig.4.6

	Data	HbO / mM		Hb / mM		H_2O / %		A		b	
		Abs.	Err. / %	Abs.	Err. / %	Abs.	Err. / %	Abs.	Err. / %	Abs.	Err. / %
	Set Values	2.3e-2		2.3e-2		0.80		2.0		2.0	
(1)	DC	1.3e-2	-76	1.3e-02	-74	0.58	-56	2.1	14	1.4	-63
	AC+PHS	1.9e-2	-29	2.1e-02	-19	0.82	6	2.3	34	1.9	-11
	DC+AC+PHS	1.5e-2	-60	1.7e-02	-48	0.67	-32	2.1	5	1.4	-61
(2)	DC	1.2e-2	-86	1.7e-02	-46	0.51	-71	2.1	14	1.6	-37
	AC+PHS	1.5e-2	-65	2.4e-02	5	0.64	-41	2.2	19	1.8	-16
	DC+AC+PHS	1.4e-2	-71	2.2e-02	-7	0.60	-49	2.1	10	1.7	-28
(3)	DC	1.3e-2	-76	1.6e-02	-54	0.60	-49	2.2	15	1.6	-36
	AC+PHS	1.6e-2	-52	2.4e-02	6	0.74	-14	2.2	22	1.9	-12
	DC+AC+PHS	1.6e-2	-52	2.4e-02	5	0.74	-16	2.2	21	2.0	-4

Table 4.7 Absolute and normalized NCRs of the images in Fig.4.6

Set	Measurement	HbO / mM			Hb / mM			H2O / %			A			b		
		Abs.	Column -wise Norm.	Row - wise Norm.	Abs.	Column -wise Norm.	Row - wise Norm.	Abs.	Column -wise Norm.	Row - wise Norm.	Abs.	Column -wise Norm.	Row - wise Norm.	Abs.	Column -wise Norm.	Row - wise Norm.
(1)	DC	0.102	1	1.0	0.097	1	1	0.083	1	0.9	0.031	1	1	0.066	1	2.2
	AC+PHS	0.071	2.1	1.1	0.063	2.0	1	0.046	1.3	0.7	0.032	1.2	1	0.035	1.3	1.1
	DC+AC+PHS	0.100	1.6	1.1	0.091	1.9	1	0.069	1.3	0.8	0.032	1.0	1	0.062	1.0	1.9
(2)	DC	0.118	1	2.1	0.056	1	1	0.098	1	1.8	0.032	1	1	0.038	1	1.2
	AC+PHS	0.085	1.9	2.1	0.042	1.5	1	0.079	1.7	1.9	0.034	1.1	1	0.032	1.1	0.9
	DC+AC+PHS	0.102	1.9	2.2	0.047	1.4	1	0.092	1.7	2.0	0.032	1.0	1	0.036	1.1	1.1
(3)	DC	0.105	1	1.7	0.060	1	1	0.068	1	1.1	0.030	1	1	0.035	1	1.2
	AC+PHS	0.093	1.8	2.5	0.038	1.4	1	0.059	1.5	1.6	0.029	1.0	1	0.032	1.2	1.1
	DC+AC+PHS	0.095	1.8	2.4	0.039	1.5	1	0.057	1.4	1.5	0.027	0.9	1	0.029	1.2	1.1

4.4.2.4 Interior imaging geometry—resolving two closely positioned identical targets

Two identical targets of 8mm in radius are embedded 10mm away from the internal boundary of the imaging geometry with angular separation of 0.4π, as is shown in the column Set of Fig.4.7.

In Fig.4.7(b), the set 2 does not resolve the two targets in water concentration as clear as the other two sets do. The set 1 (Fig.4.7 (a)) and the set 3 (Fig.4.7(c)) are similar. Cross-sectional plots along the gold dotted lines are displayed in Fig.4.8. Note that since the non-uniform sensitivity of the geometry tends to reconstruct the targets in positions closer to the inner boundary, the radius of the dotted circles for reconstructed images is slightly smaller than those for the plots of set values. The upper target is recovered with less contrast compared with the lower one is, due to the configuration that the lower target coincidently is located in the same angular position of an optode and thereby reconstructed with enhanced sensitivity. Table 4.8 lists the target-to-valley contrast and target-to-background contrast ratios, comparable to those in Table 4.5. Table 4.8 indicates slight advantage of DC reconstruction over FD. The sets 1 and 3 separate targets better than the set 2 does in water concentration distribution, however, no significant difference between the two sets of 1 and 3 can be observed.

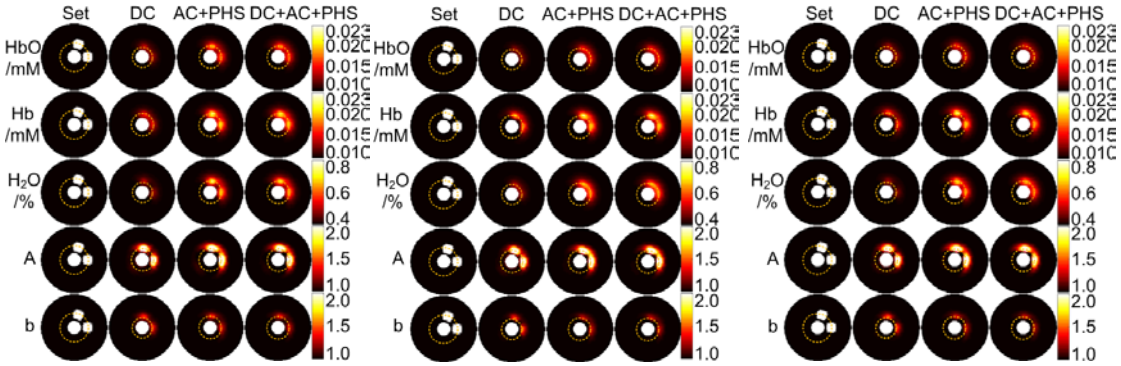

(a) (b) (c)

Fig.4.7 Synthetic study on two targets with all five parameter contrasts in image geometry (b) in Fig.4.2. (a)(b)(c) are the results for the wavelength set (1)(2)(3) in table I, respectively. (a)(c) Targets are separable in all cases. (b) Targets are inseparable in HbO, H_2O and b distribution recovery by FD measurements.

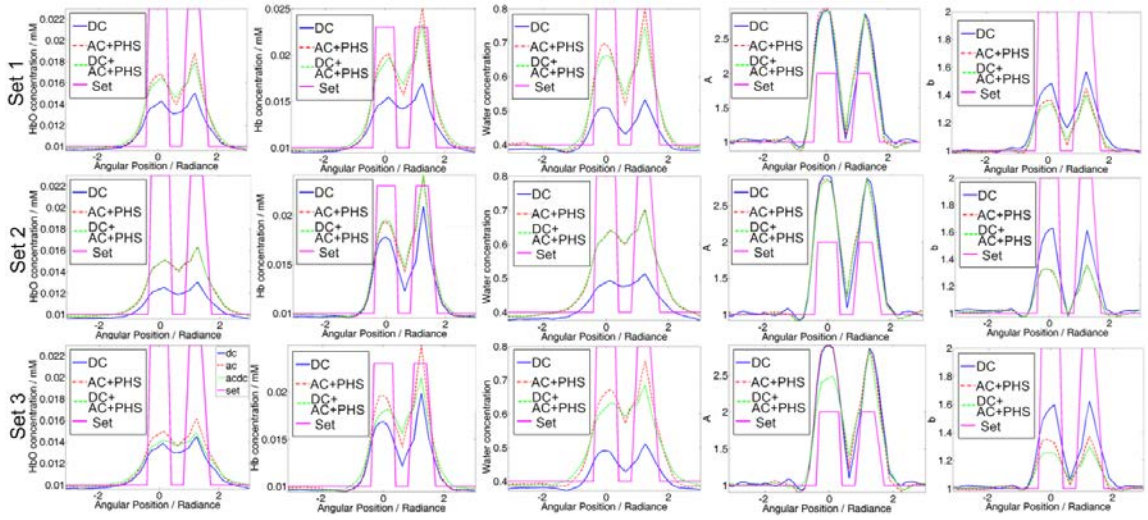

Fig.4.8 Parameter contour plot along the gold dash lines in Fig.4.7. DC reconstruction shows slight advantage over FD in most cases.

Table 4.8 Comparison of target separation in Fig.4.5

	Data	HbO	Hb	H_2O	A	b
(1)	DC	0.28	0.23	0.72	0.98	0.66
	AC+PHS	0.43	0.44	0.61	0.95	0.89
	DC+AC+PHS	0.30	0.29	0.45	0.91	0.78
(2)	DC	0.26	0.76	0.18	0.95	1.03
	AC+PHS	0.20	0.46	0.17	0.87	1.05
	DC+AC+PHS	0.19	0.51	0.15	0.87	1.03
(3)	DC	0.24	0.69	0.69	0.95	0.78
	AC+PHS	0.27	0.57	0.37	0.88	0.93
	DC+AC+PHS	0.13	0.31	0.18	0.78	0.81

4.4.3 Comparison of $\mu_a(\lambda)$ and $\mu_s'(\lambda)$

Since the sensitivity matrices of multi-spectral NIR tomography are derived from that of single-wavelength optical tomography, the reconstruction results of $\mu_a(\lambda)$ and $\mu_s'(\lambda)$ could also be insightful to evaluating the reconstruction performance. In this section, the analytical model of

$\sigma_{\mu a(\lambda)}$ and $\sigma_{\mu s'(\lambda)}$ will be compared to $\sigma_{\mu a(\lambda)}$ and $\sigma_{\mu s'(\lambda)}$ derived from synthetic studies. However, there is difference between the PRUL calculations of $\sigma_{\mu a(\lambda)}$ and $\sigma_{\mu s'(\lambda)}$ in analytical model and in simulation. For analytical model, the calculations of $\sigma_{\mu a(\lambda)}$ and $\sigma_{\mu s'(\lambda)}$ involve evaluating $\mu_a(\lambda)$ and $\mu_s'(\lambda)$ in equation (4.2) with the preset simulation parameters and substituting $\mu_a(\lambda)$ and $\mu_s'(\lambda)$ values into table II and IV in [102]. Whereas for simulation, $\mu_a(\lambda)$ and $\mu_s'(\lambda)$ values are not recovered explicitly in the reconstruction under spectral-prior, therefore, the PRULs of the recovered parameters need to be reversely projected to $\sigma_{\mu a(\lambda)}$ and $\sigma_{\mu s'(\lambda)}$, by equ.s(4.19) and (4.20):

$$\left(\vec{\sigma}_{\vec{\mu}_a(\lambda)}\right)_{m\times 1} = \left|\frac{\partial \vec{\mu}_a(\lambda)_{m\times 1}}{\partial(\vec{c})_{n\times 1}}\right|_{m\times n} \times \left(\vec{\sigma}_c\right)_{n\times 1} = \log(10)\cdot(\vec{\varepsilon})_{m\times n} \times \left(\vec{\sigma}_c\right)_{n\times 1} \tag{4.19}$$

$$\left(\sigma_{\mu_s'(\lambda)}\right)_{m\times 1} = \sqrt{\left(\frac{\partial \mu_s'(\lambda)}{\partial A}\right)^2_{m\times 1}\cdot\sigma_A^2 + \left(\frac{\partial \mu_s'(\lambda)}{\partial b}\right)^2_{m\times 1}\cdot\sigma_b^2} = \left(\sqrt{(\lambda^{-b}\cdot\sigma_A)^2 + (-A\lambda^{-b}\cdot\log\lambda\cdot\sigma_b)^2}\right)_{m\times 1} \tag{4.20}$$

Analytical and simulated values of $\sigma\mu_a(\lambda)$ and $\sigma\mu_s'(\lambda)$ are plotted verses the wavelengths in Fig.4.9 (a) and (b) respectively. The curve shapes agree between the analytical predictions and reconstruction results, yet the relative magnitudes of the curves differ slightly. In the analytical prediction, the uncertainties always follow the relationship of $\sigma_{DC}<\sigma_{AC+PHS}\leqslant\sigma_{DC+AC+PHS}$ for both $\mu_a(\lambda)$ and $\mu_s'(\lambda)$. In simulation study, one has $\sigma_{\mu a(\lambda)\_DC}< \sigma_{\mu a(\lambda)\_DC+AC+PHS}\leqslant\sigma_{\mu a(\lambda)\_AC+PHS}$. However, for $\sigma\mu_s'(\lambda)$, DC reconstruction is not definitely advantageous over FD, even though $\sigma_{\mu s'(\lambda)\_DC+AC+PHS}<\sigma_{\mu s'(\lambda)\_AC+PHS}$ stands for all cases.

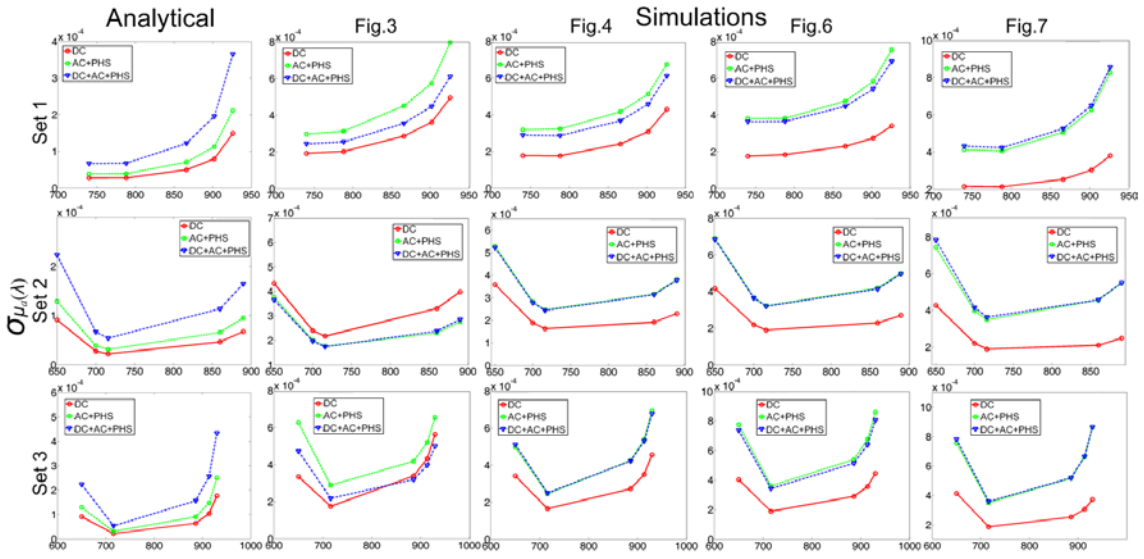

(a)

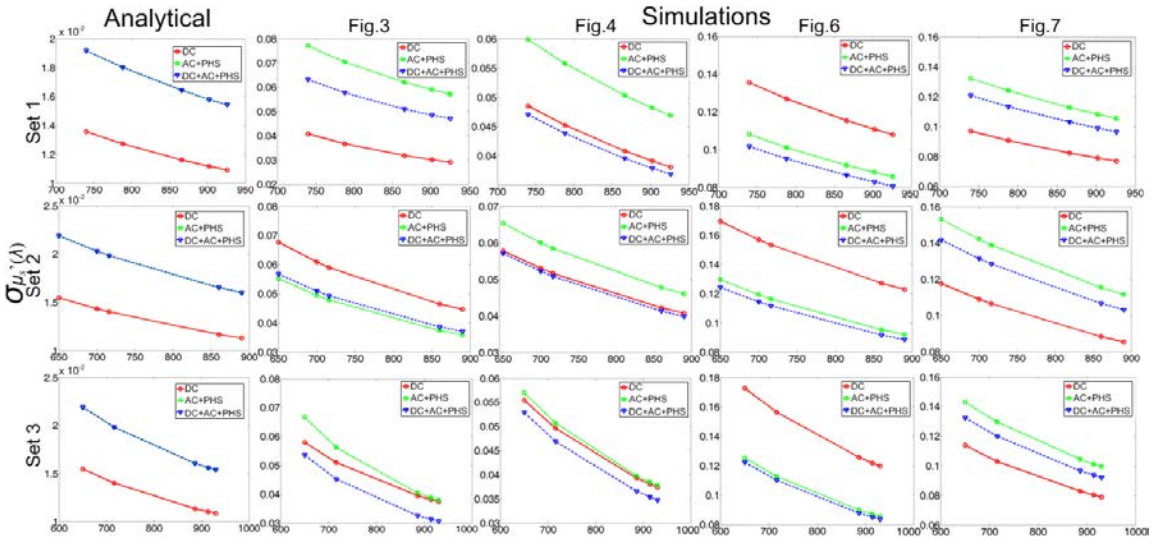

(b)

Fig.4.9 Comparison between the artifact levels in absorption and scattering coefficients at each wavelength. Curve shapes of analytical model and synthetic studies agree in all cases. (a) Absorption coefficients comparison. DC reconstructions show least background artifact levels. DC+AC+PHS for most cases outperforms AC+PHS. (b) Scattering coefficients comparison. DC

reconstructions does not necessarily show least background artifact levels. DC+AC+PHS at most cases outperforms AC+PHS.

4.5 Discussions

The analytical model is derived for an infinite homogenous medium, but the outcomes are apparently applicable to geometries with boundary and with anomaly as those in the simulations. The PRUL analyses introduced in [102] actually implicated the uniqueness of the solutions of DC only reconstruction in multi-spectral NIR tomography. Previous studies [83-84] suggested that in a homogenous medium, the product of $\mu_a(\lambda)$ and $D(\lambda)$ can be considered as a constant function of the surface diffuse reflectance of the medium as:

$$[\mu_a \cdot D] = K(R_\infty) \tag{4.21}$$

Taking equation (4.21) into consideration, $\mu_a(\lambda)$, $D(\lambda)$ and $\mu_s'(\lambda)$ can be independently expressed as [102]:

$$\mu_a(\lambda)\big|_{DC} = \sqrt{K(R_\infty(\lambda))} \cdot \frac{\delta(\lambda)}{\rho} \tag{4.22.1}$$

$$D(\lambda)\big|_{DC} = \sqrt{K(R_\infty(\lambda))} \cdot \frac{\rho}{\delta(\lambda)} \tag{4.22.2}$$

$$\mu_s'(\lambda)\big|_{DC} = \frac{1}{3D}(\lambda) - \mu_a(\lambda)\Big|_{DC} = \left(\frac{1}{3\sqrt{K(R_\infty(\lambda))}} - \sqrt{K(R_\infty(\lambda))}\right) \cdot \frac{\delta(\lambda)}{\rho} \tag{4.22.3}$$

If the DC optical tomography measurement lacks $K(R_\infty)$, equation (4.22) may become under-determined and thereby inter-parameter cross-coupling may exist. Under spectral *prior*, however, the $\sqrt{K(R_\infty(\lambda))}$ term could be eliminated and subsequently the cross-coupling be reduced. By combining equations (4.22.1) and (4.22.3) and substituting into equations (4.2.1) and (4.2.2), the DC measurement becomes the function of only the absorption chromophore concentrations and scattering parameters as:

$$\frac{\delta^2(\lambda)}{\rho^2} = 3\mu_a(\lambda)(\mu_a(\lambda) + \mu_s'(\lambda)) = 3 \cdot \sum_i \varepsilon_i(\lambda) c_i \cdot \left(\sum_i \varepsilon_i(\lambda) c_i + A\lambda^{-b}\right) \tag{4.23}$$

Therefore one can decouple the unknown values once measurements at sufficient number of wavelengths are available. This agrees with the observation in this and several previous studies that DC reconstruction with spectral *prior* successfully resolves the tarter, as evidenced in figures 3 and 6. Interestingly, as is shown in figures 4 and 7, even in the FD reconstruction the intrinsic cross-coupling problem becomes significant when multiple contrasts are assigned to the same location [104]. As fewer measurement components in DC reconstruction facilitate less system noise in the inverse problem, the level of background artifacts are actually lower in DC reconstruction.

The method of ranking the spectral-*prior* sets conforms to the recommendation by [7] at desirably less computation load. Nonetheless, the optimized wavelength set depends upon a reliable sensitivity distribution for the optimal outcome. For example, the set 3 clearly outperforms the set 1 in Fig.4.4 but not as clearly in Fig.4.7. Therefore, the choice of spectral *prior* for a given number of wavelengths is to be associated with the sensitivity distribution in the imaging domain.

The PRUL analyses of both multi-spectral reconstruction parameters and the optical properties have been shown reliable. However, there is still disagreement between the analytical prediction and simulation results due to the approximation in analytic modeling and smoothing effect in synthetic studies. For example, since the analytical model only accounts for the perturbations in the measurement, it is predicted that DC-excluded FD will outperform DC-included FD, yet the simulation shows the contrary. Such aberrations actually explain that extra information in DC components has balanced the excessive reconstruction uncertainties and made DC+AC+PHS a better choice than AC+PHS for FD reconstruction.

4.6 Summary

A PRUL analysis model has been applied to multispectral optical tomography and used to evaluate the sets of wavelength for spectrally-constrained optical tomography reconstruction. The analytical predictions are generally supported by simulations. In imaging geometries where

reliable sensitivity distribution is available, DC-only reconstruction outperforms FD reconstruction. The advantage of the extra phase information in FD measurement becomes prominent under significantly non-uniform spatial sensitivity distribution. It is also found that including DC component in FD reconstruction improves the overall reconstruction results in multi-spectral optical tomography, which is similar to that demonstrated in single-wavelength NIR tomography reconstruction.

CHAPTER V

INSTRUMENTATION OF A RAPID NEAR-INFRARED DIFFUSE OPTICAL TOMOGRAPHY SYSTEM WITH WAVELENGTH SWEPT LIGHT SOURCE

5.1 Introduction

Near-infrared tomography has demonstrated high functional contrast in areas such as cancer imaging[5, 11, 13, 107-109], extremity imaging[77, 110] brain functional imaging [111-113] and small animal imaging[114-116]. However, compared to other imaging modalities such as X-ray and ultrasound imaging, the relatively low frame rate of NIR tomography is desired to be improved, especially in brain function imaging, which requests video rate image acquisition for capturing rapid brain activities.

Most of traditional NIR tomography system utilizes single light source and delivers the source light to each source channel by mechanical/fiber switching [13, 107-108, 110, 117], which ensures the intensity uniformity of each source channel but the time delay between channels restricts the data acquisition speed.

Several rapid, video rate imaging acquisition system structures have been investigated during the past few years, including temperature controlled multiple laser diodes [118-119] and spectral encoding of broad band light source[14]. Temperature controlled multiple Laser diodes system demonstrates higher acquisition rate (approximately 3Hz) but the intensity of the laser diodes are subject to fluctuation and for imaging scenarios with large source arrays such as

Brain functional imaging, the CCD dimension might not be able to cover all the source channels dispersed by the spectrometer. Broad-band spectral encoding system possesses the advantage of acquiring signals simultaneously from all detector channels by splitting the broadband source light with diffraction grating and coupling the light power into linearly arranged source channels. However, since continuous spectrum of the broadband light source includes the coupling of multiple wavelengths into each source channel, signals from detector channels are cross-coupled, which involves a de-convolution process for the distinct separation of the signals from each detector channel[14].

Swept-wavelength light source is widely utilized in optical coherent tomography for its flexibility in the manipulation of detection depth[120-122], and is recently reported to have been utilized in optical topology[123]. Considering the rapid wavelength scanning speed and program-controllable characteristics of the wavelength swept light source, a novel optical tomography setup have been designed and constructed. Several advantages have been demonstrated by phantom experiments: 1) The spectrally and temporally encoded source light of such system facilitates rapid channel switching rate compared to mechanical switching; 2) accurate single wavelength source light delivery to each source fiber eliminated cross coupling problem in broadband spectral encoding systems; and 3) independent source illumination fundamentally extends CCD capacity on the source-channel coverage, which allows more source channels on the imaging applicator within a given CCD dimension.

In addition, it is commonly agreed that the calibration is critical to the reliable measurement and reconstruction results for all imaging systems. In the NIR tomography area, most of the system calibration includes 2 steps: fitting analytical and numerical light propagation model to the experimental measurements. Although the latter is well investigated and generally based on iterative solution of the optical properties of a homogeneous medium, the analytical model fitting is less concerned. For most of contemporary studies, researchers utilize the analytical planar semi-infinite photon diffusion model solved by Fantini et al [81], which

approximates the signal intensity attenuation in log scale and phase shift of the measurements to a linear model. Such approach demonstrates robustness in many frequency domain systems, in which only the gradients of the measurement components are considered in the analytical fitting process. However, as to the continuous wave systems, since multiple optical properties cannot be strictly decoupled by merely utilizing the attenuation of light signal intensity, the absolute values fitting is also required. Therefore, more accurate analytical models specified for the applicator geometry of each imaging system are desired, which, for the particular case of this study, is derived and reported by Zhang et al[124]. Validated by experiments, the analytical model for photon diffusion in cylindrical geometry provides more reliable and accurate on the estimation optical properties of homogeneous medium, which ensures that the numerical fitting process converges to the optimum solutions for measurement-to-numerical-model offset determination.

In this paper, the structure of the system will be discussed and experimental results based on phantom data will be shown for the performance of system assessment and the novel calibration method for imaging applicator in cylindrical geometry is demonstrated in detail.

5.2 Review of previous system structures

Before the presentation of our innovative system structure for rapid FDOT system, DOT system structure presented by previous studies are briefly reviewed as the basis of our design for a CW measurement based, rapid DOT/FDOT system.

Time multiplexing by mechanical switching is the most commonly implemented structure for multi channel DOT systems. As is shown in Fig. 5.1, the fiber switch couples a narrow band light source sequentially to each of the source channels. The system is readily extendable to FDOT because the excitation and emission band fluorescence signals are independent in time with respect to each source channel. However, the data acquisition rate of such system is limited by the switching intervals.

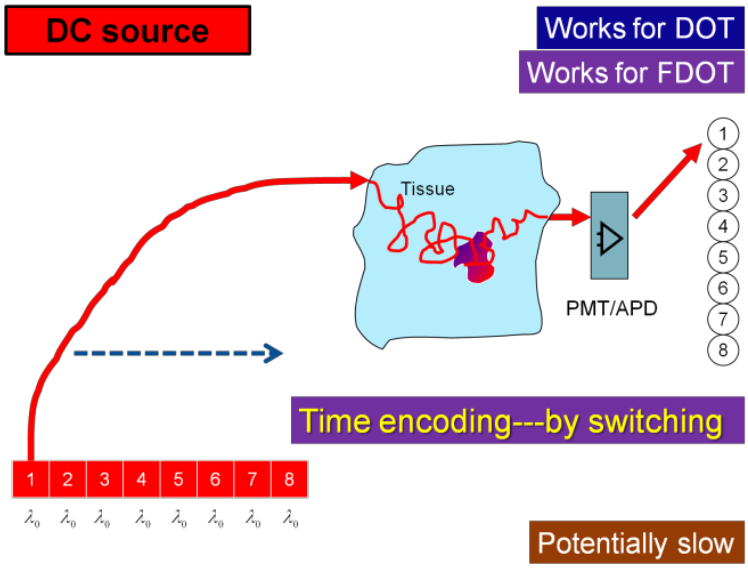

Fig. 5.1 Illustration of mechanical switching

Spectral encoding of the source channels method can facilitate the simultaneous illumination of all source channels and improve the data acquisition rate. As is shown in Fig.2 the system structure either uses parallel discrete laser sources with closely located wavelengths or by using a narrow-band light source after splitting the light with a grating. At the detection end, the diffused light signals are separated with respect to the wavelength of each source channel by a spectrometer and captured by a CCD camera. None the less, such system structure does not support fluorescence emission signal acquisition as the fluorescence emission spectrum does not vary corresponding to the excitation wavelength. The identification of the fluorescence emission signal with respect the the source channels is thereby not possible by a spectrometer and CCD system.

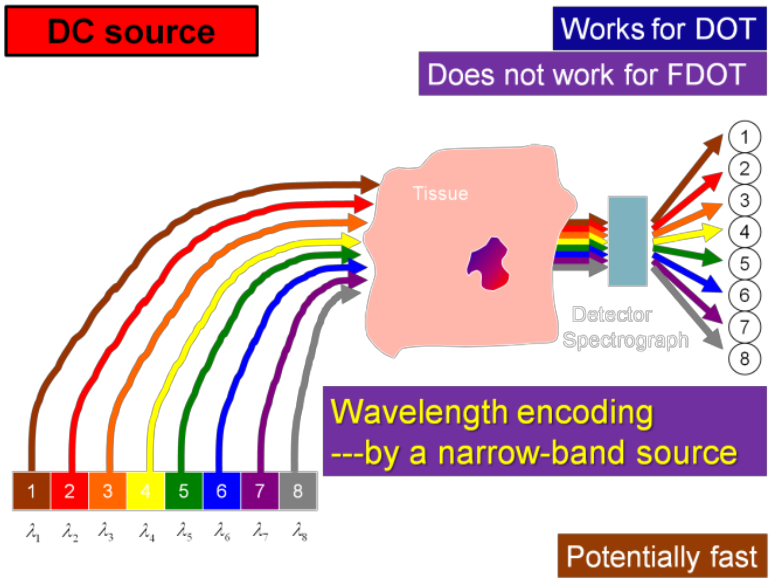

Fig. 5.2 Illustration of spectral encoding

The simultaneous source channel illumination can be achieved by frequency modulating method. As is shown in Fig.5.3, each source channel is modulated by a unique frequency. The fluorescence emission signals can thereby be separated with respect to the source channel with frequency lock amplifiers. However, such system structure exceeded our scope of developing CW measurement based system. The instrumentation complexity would be significantly elevated and the computational modeling would include the phase shift of the light signals.

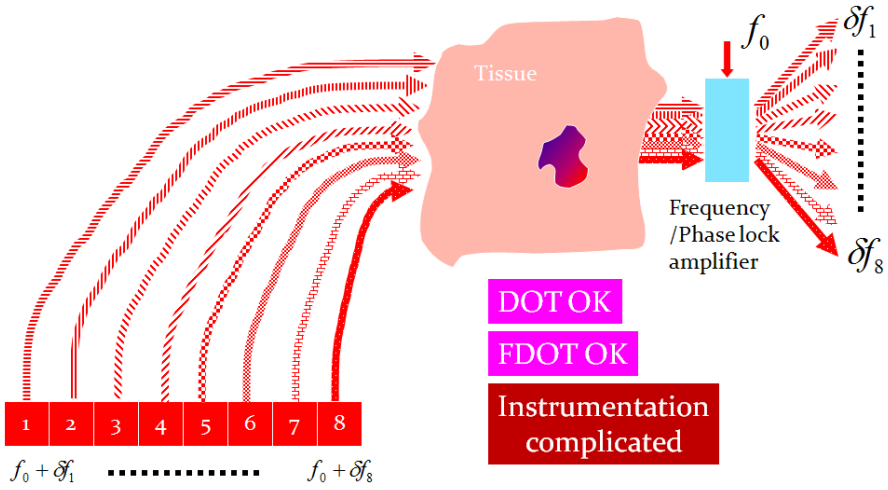

Fig. 5.3 Illustration of frequency multiplexing

Summarizing the system structures shown above, we came to the idea of a wavelength swept light source based DOT and FDOT system structure. The structure enables the spectral encoding of the source channels and sequential yet rapid switching source channel illumination.

5.3 Principles

The initial idea of the system structure is to separate wavelengths by utilizing the difference in diffraction angle and capture detection signals from all channels with sufficient exposure time for one cycle of wavelength sweeping. As is shown in Fig.5.4, the source light with varied wavelengths is dispersed by spectrometer one and sequentially coupled to the source channels linearly arranged at the output plane of spectrometer 1. Therefore, the rapidly sweeping source light be appears similar to a broadband light, and a spectral source light encoding similar to the one reported in [14] is achieved. At the detection end, spectrometer two decodes the light signals by dispersion angles and the CCD camera, as is shown in Fig.5.5 (a) (with 1200 groove/mm grating) and (b) (with 600 groove/mm grating).

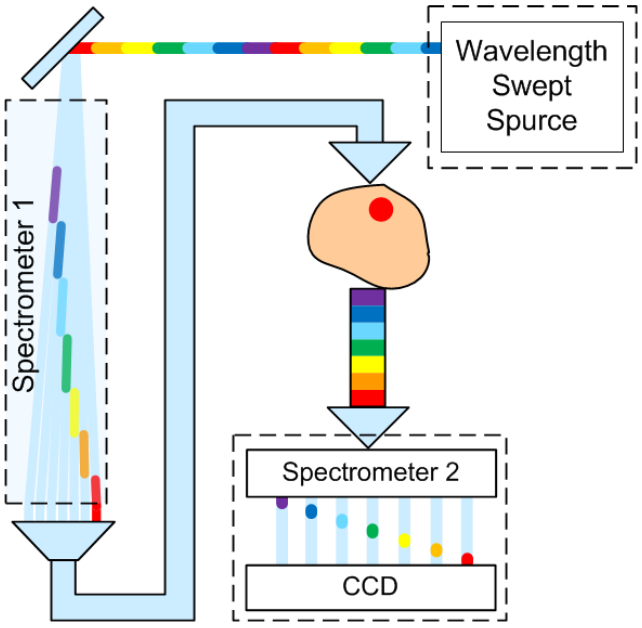

Fig.5.4 Principle Illustration of a wavelength-swept

However, challenges exist in this system scheme as is demonstrated in Fig.5.5: 1. cross coupling between the source channels caused by the continuous wavelength swept, which is

identical to that in spread-spectral-encoding system; 2. minimization of source channel cross coupling with larger grooves per mm gratings exceeds the CCD coverage range; 3. synchronization of the source sweep and camera exposure is difficult because of the rapid sweeping.

The source channel cross coupling can be minimized by accurate collimation and appropriate source fiber separation. However, for the detection end, the signal overlapping and the CCD dimension is contradictory, because CCD cannot cover all the source channel wavelengths if the light signal spots are clearly separated (Fig.5.5(a)) and vice versa(Fig.5.5(b)).

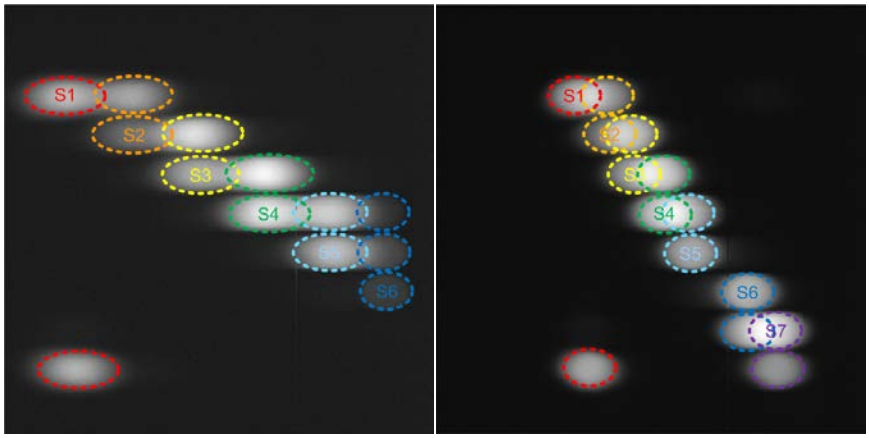

(a) (b)

Fig.5.5 drawbacks of free sweeping mode. (a) image captured with 1200 grooves/mm grating; (b) image captured with 600 grooves/mm grating

One solution to such problems is to capture the detection signal from each source channel independently in time, *per se*, by temporal encoding. Mathematically, The spectral and temporal encoding can be combined and represented by equ(5.1):

$$\mathbf{Loop}(t=1{:}m)\mathbf{:}\ \{\boldsymbol{D}(t)_{n\times 1}=(\boldsymbol{W}_{m\times n})^{T}\times\boldsymbol{T}(t)_{m\times m}\times\boldsymbol{Spec}_{m\times m}\times\boldsymbol{S}_{m\times 1}\} \tag{5.1}$$

Where t is wavelength-swept time slot controlled by PC; $D(t)$ is the detector signal at time t, W is the weight matrix or sensitivity matrix of the imaging geometry; $T(t)$ is the diagonal

matrix representing the time-encoding, $\boldsymbol{T(t)(i,i)}=\begin{cases}1 & i=t\\ 0 & i\neq t\end{cases}$;$\boldsymbol{Spec}=\begin{bmatrix}\lambda_1 & \lambda_2 & \cdots & \lambda_3\\ \lambda_1 & \lambda_2 & \cdots & \lambda_3\\ \vdots & \vdots & \ddots & \vdots\\ \lambda_1 & \lambda_2 & \cdots & \lambda_3\end{bmatrix}$ is the spectral encoding matrix.

According to the theoretical hypothesis, system schematics are shown in Fig.5.6. Controlled by the PC, the source light swept stops when maximum source power is coupled to each source channel, followed by the CCD exposure. Therefore, for one imaging cycle, image acquisition number equals to the number of source channels, instead of one and a spectral-temporal source light encoding is achieved. Such design facilities the temporal separation of the light spots at the detection end despite the spatial overlapping. With all the concerns mentioned, the system is constructed. Specifications are detailed in the next section.

5.4 Instrumentation

As is shown in Fig.5.6, Superlum BS-840-02 tunable semiconductor light source is controlled by Labview to generate spectral encoding source light. The light source provides light power up to 4mW and scans in the range of 838nm to 858nmat increment of 0.05nm. The wavelength stability is ±2.5pm per five hours.

The source light is lead out by a 5-μm-diameter fiber with numerical aperture of 0.14 and collimated by Thorlabs C230TME-B (focal length 5.51mm), producing a 0.08 mm-diameter light beam cross section, which is significantly smaller that of the source channel fiber optics(1mm diameter), indicating that the cross coupling effect can be minimized if the light beam is projected to the center of the source fiber crossection.

The collimated source light is fiber coupled to a SpectroPro 500i spectrometer by Princeton Instrument, the spectrum center of which is set at 850nm. The 1200 groove per mm grating and 500mm path length of the spectrometer expand the 20nm-range source light beam with incident angle of 20^o to approximately 15mm at the output plane of the spectrometer, where

the 1mm diameter source fibers are linearly arrange for the sequential coupling of the source light. With such setup, 1mm separation on the output plane can be traced back to the split angle of two is approx. 0.11 degree, and accordingly the wavelength difference between two neighboring channel is approximately 1.5nm.

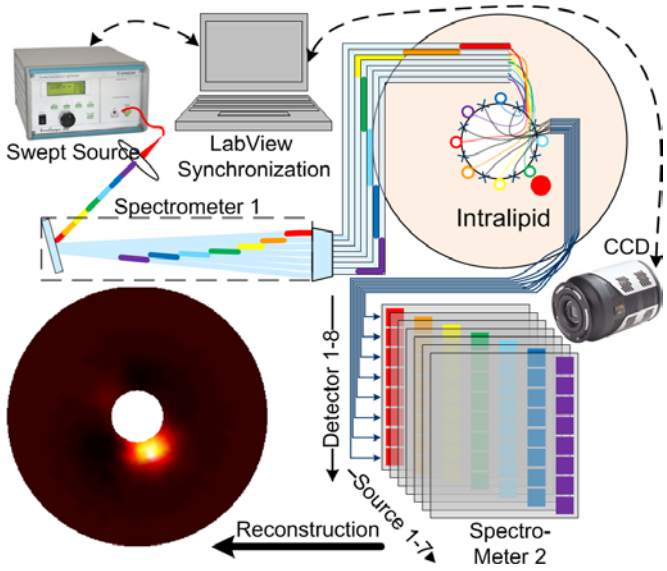

Fig.5.6 System Schematics

At the detection end, PIXIS 512 CCD camera with 12.3mm×12.3mm imaging area and SpectroPro 2300i with 300mm focal length by Princeton instrument are integrated for signal acquisition. Source-detector synchronization is achieved by DAQ card by National Instrument and PC serial port, both program controlled by LabView (National Instrument). For each imaging cycle, the PC first sends command to tune the source light to the predetermined wavelength at which maximum light power is coupled. Afterwards, an external trigger signal is send to the CCD camera to capture detection signals. Limited by the source power, a minimum exposure time of 170ms is required and an extra 150ms CCD readout time has to be added to the total time delay before tuning the source light to the next source channel. Therefore for each channel, omitting the commands transferring time, approximately 320ms is required, which is equivalent to approximately 0.5 per second frame rate. However such acquisition duration can be reduced by increasing source and video rate CCD camera.

A two dimensional circular endoscopic imaging geometry previously presented by our group[42] is used in this study. As is shown in Fig.5.7, the 8 source channels and 8 detector channels are fabricated evenly interspersed around the perimeter of the 20mm-diameter probe cross-section. However, one source channel (marked in Fig.5.7(c)) is discarded because of its significantly low coupling efficiency due to fabrication defect.

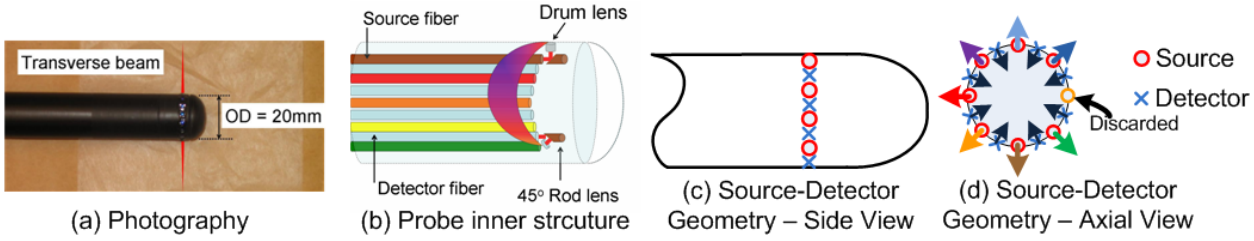

Fig.5.7 A circular endoscopic imaging geometry

The actual experimental system constructed under the considerations described above is shown in Fig.5.8.

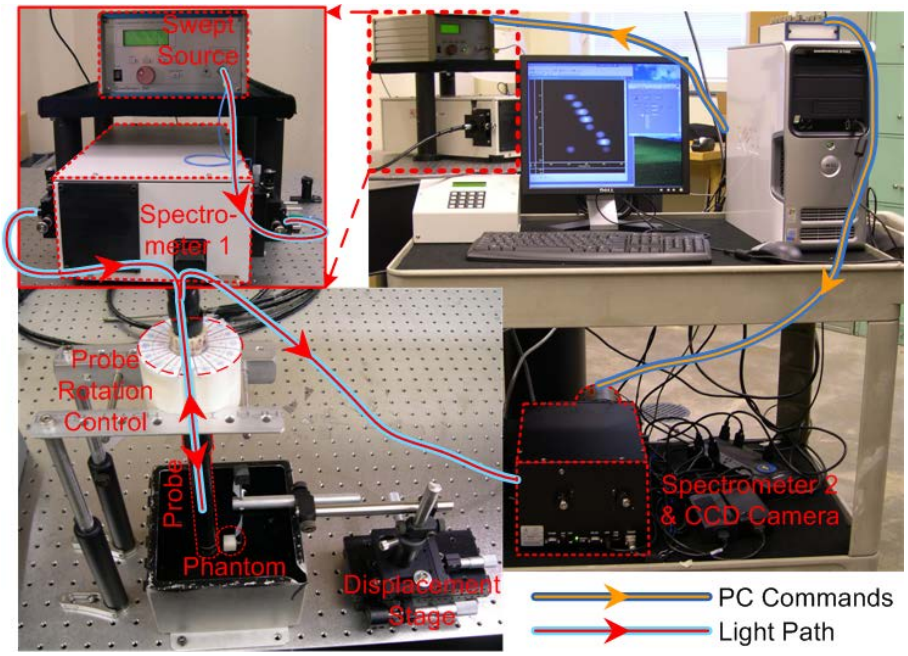

Fig.5.8 Experimental system constructed

5.5 System performances

With the exposure time and source power introduced above, intensity detected by the 64bit CCD camera can reach the maximum of 60000 and minimum of 1000, which is above the background noise level of the system is approximately 700 unit value of the CCD.

One set of images captured by submerging the probe into 1% intralipid solution, Fig.5.9(a) shows the images acquired after subtracting dark background. Fig.5.9(b) shows the summation of the pixel values along each column of the image. Narrow coupling bands can be obviously observed, indicating the minimization of channel cross coupling. By averaging through the center part (marked with red squares in Fig.5.9(c)), of each light spots the data points are extracted for calibration and reconstruction(Fig.5.9(d)).

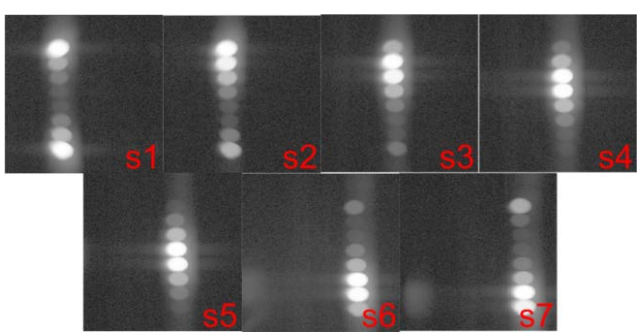

(a) Data spots captured by CCD camera

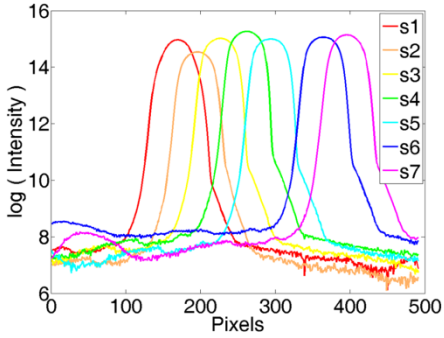

(b) Sources Separation

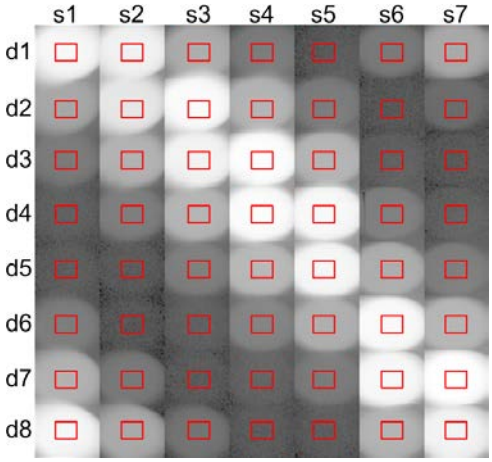

(b) Cropped data spots and center average

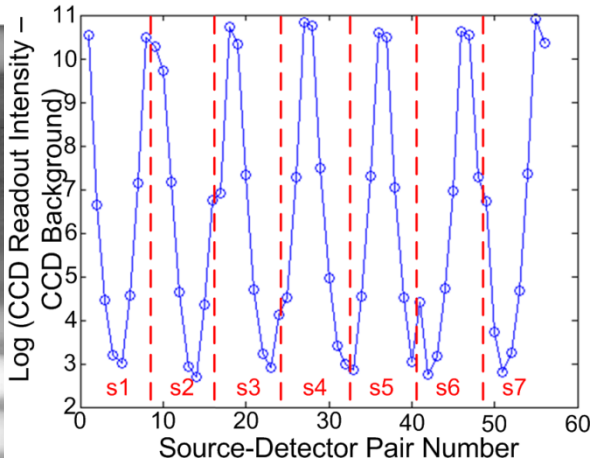

(c) Extracted measurement intensities

Fig.5.9 Raw data processing

It can be observed from the extracted data points that the source intensities are relatively uniform because of the constant output power of the light source at all wavelengths as expected, which is another advantage of using swept source over broadband light source.

5.6 Calibration

In this study, the calibration algorithm is designed to search for the offset values between the experimental data, analytical and numerical model in log scale. 1% intralipid with μ_a= 0.0023 mm^{-1} and μ_s'=1mm^{-1} is used in the calibration process. The calibration involves 2 stages: 1) estimation of the homogeneous properties with analytical model and; 2) experimental data offset determination with numerical model.

For the analytical fitting process, most of previous studies use the linear model for semi-infinite homogenous turbid media reported by Fantini et al[81], which is derived under the condition that the measurement surface is planar:

$$\frac{\partial[\ln(d\cdot I_{DC})]}{\partial d}=-\sqrt{\frac{\mu_a}{D}},\ \frac{\partial[\ln(d\cdot I_{AC})]}{\partial d}=-\sqrt{\frac{\mu_a}{2D}\left(\sqrt{1+\frac{\omega^2}{v^2\mu_a{}^2}}+1\right)}\ (1),\ \frac{\partial\phi}{\partial d}=\sqrt{\frac{\mu_a}{2D}\left(\sqrt{1+\frac{\omega^2}{v^2\mu_a{}^2}}-1\right)}$$

(5.2)

Where d is the source-detector distance, I is the light intensity, subscript AC and DC denotes continuous wave and frequency domain measurement. μ_a is absorption coefficient and D is diffusion coefficient. ω is angular modulation frequency and v is the speed of light in the measured media.

However, experiments shows that such model does not accurately represent the light transportation pattern in cylindrical semi-infinite geometry, as is shown in Fig.5.10(a). Zhang et al [124] have analytically derived steady-state photon diffusion model for such cylindrical geometry and validated their conclusion by experiment:

$$\Psi=\frac{S}{2\pi^2 D}\int_0^\infty dk\left\{\sum_{m=0}^{\infty}\varepsilon_m I_m(k_{eff}R_0)K_m[k_{eff}(R_0+R_a)]\left\langle 1-\frac{K_m(k_{eff}R_0)}{I_m(k_{eff}R_0)}\frac{I_m[k_{eff}(R_0-R_b)]}{K_m[k_{eff}(R_0-R_b)]}\right\rangle\cos[m(\varphi-\varphi')]\right\}$$

(5.3)

Where S is the source intensity; D=1/(3(μ_a+μ_s')) is diffusion coefficient; R_0 is the probe radius; R_a=1/ μ_s',is the scattering distance of the imaged medium; ε_m is 2 for m≠0 and 1 for m=0; I_m and K_m are Henkel function of the first and second kind; k_{eff} is the attenuation coefficient; φ and φ' are the angular coordinate of detector and source, respectively.

Therefore, instead of using the conventional linear model, the cylindrical analytical model is implemented in the first stage of the calibration. For the evaluation of the model, since Henkel function consists of infinite series, approximation is applied by cutting off the series at the 60^{th} terms. Such approximation is computationally efficient but introduces discontinuity in the function evaluation, which is not allowed in the commonly used gradient based fitting algorithms. A heuristic random optimization approach [125] is thus integrated into the analytical calibration process. It should also be noted that instead of fitting only gradient of the measurement values with respect to the source detector distance as in conventional method, this study fits the absolute value of the data points because: 1) Only continuous wave measurement is available; 2) the non-linear function in analytical model cannot be simply represented by slope and intersection of a linear model as in the conventional calibration process.

Since 1) the absolute values are fitted; 2) the duration of the analytical model evaluation increases proportionally to the number of sampling points; and 3) calibration process bases on homogeneous media, only the analytical model is evaluated only at possible source-detector separation in the experimental geometry shown in Fig.5.7. Therefore, only 4 data points are evaluated in each analytical fitting iteration.

It can be observed that S value is independent of the integral in Equ. (5.3), and in log scale, it is an amplitude bias of the analytical model, which is found to bring in large projection error in the fitting process and might destabilize the searching for other parameters. To suppress such instability, the algorithm first minimizes the log(S) value and starts the overall parametric search, the result (Fig.5.10(a) red curve) of which is assign to the FEM model as initial guess of the second calibration stage. It can be clearly observed from Fig.5.10(a) that the algorithm

recognized the larger light intensity attenuation in a nonlinear pattern by correcting the μ_a initial guess of 0.005mm^{-1} to 0.0029 mm^{-1}.

For the numerical fitting stage, finite element method is used. A finite element mesh with the ring geometry shown in Fig.5.6 is generated with 872 nodes and 1620 elements uniformly distributed in the imaging domain. The numerical calibration also starts from searching for the optimum amplitude bias, which is subsequently optimized along with the optical properties of numerical model. Similar to the conventional image reconstruction process, the optical properties of all finite element nodes are uniformly and iteratively updated and the difference between finalized model and the measurement data are determined as the offset values. And the final model fitting converged to the optical properties of μ_a=0.0023mm^{-1} and μ_s'=0.8982, of which the μ_s' part could be more accurate if analytical model and measuremenst in frequency domain are available.

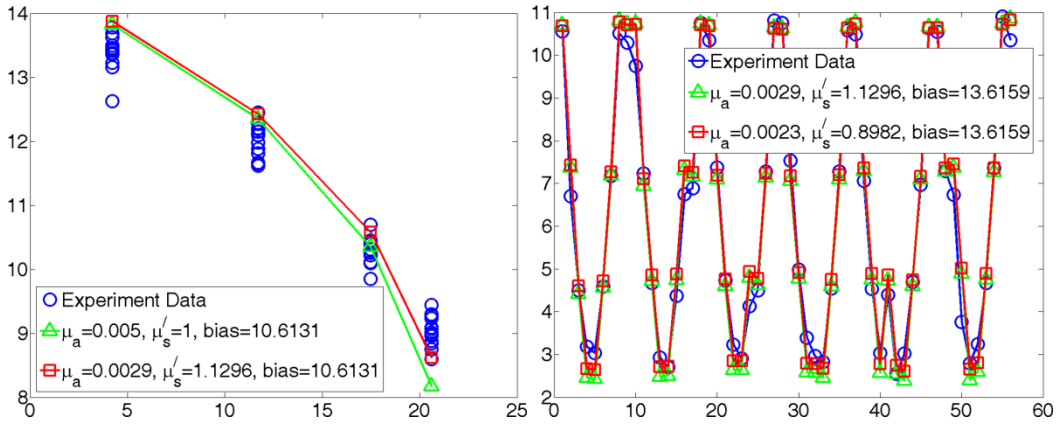

(a)Analytical model calibration (b) Numerical model calibration

Fig.5.10 Data calibration

5.7 Experiments

To examine the performance of the novel system configuration, a series of experiments are conducted with liquid and solid phantoms.

5.7.1 Experiments setup

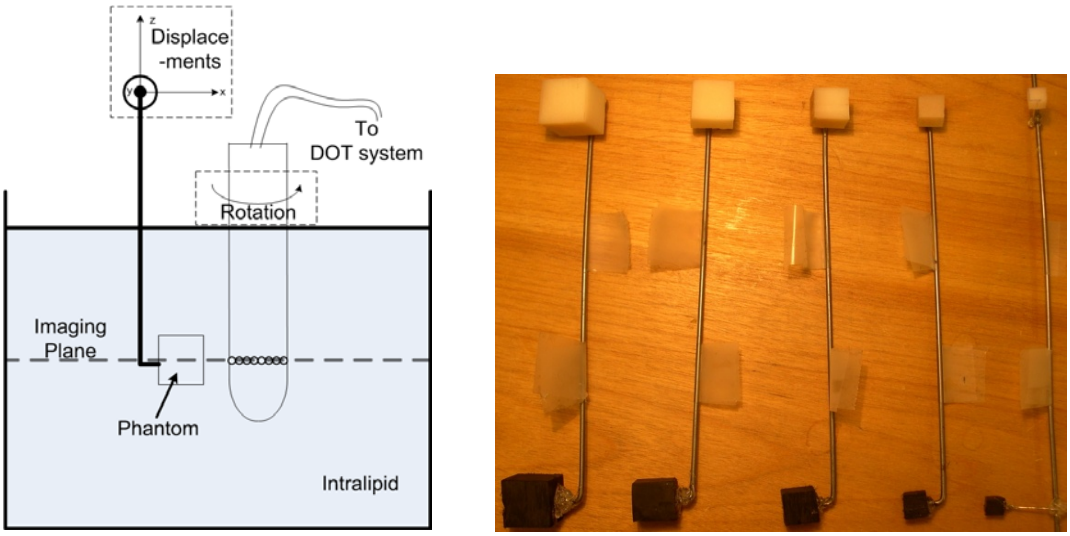

(a) Experiment setup illustration (b) Solid phantom targets

Fig.5.11 Experiment setup and materials

As is shown in Fig.5.11(a), the probe is submerged in a 10in×10in×5inch tank filled with intralipid. The inner walls of the tank are painted black to minimize the reflection. The solid phantom targets to be imaged are fabricated with black plastic with infinite absorption contrast to the background intralipid and synthetic phantom with μ_a= 0.0056 mm^{-1} and μ_s'=1.03 mm^{-1}. As is shown in Fig.5.1(b), side lengths of the cubic shape solid phantom range from 5mm to 15 mm. The centers of the targets are placed at the imaging plane of the probe and the Horizontal stages are used to accurately control the displacement of the targets. Further, the probe is rotated with respect of the targets to examine the azimuthal sensitivity of the system.

5.7.2 Experiment results

According to the experimental setup, four sets of experiments are conducted to examine system sensitivity on 1) inclusion size (Fig.5.12(a)); 2) radial direction (Fig.5.13(a)); 3) azimuthal direction (Fig.5.11(a)); and 4) multiple inclusions (Fig.5.12(a));.

The first set of results is derived from experiments with varied target sizes and target materials. Cubic targets shown in Fig.5.11(b) are sequentially embedded in the imaging plane at side-to-probe distance of 5mm.

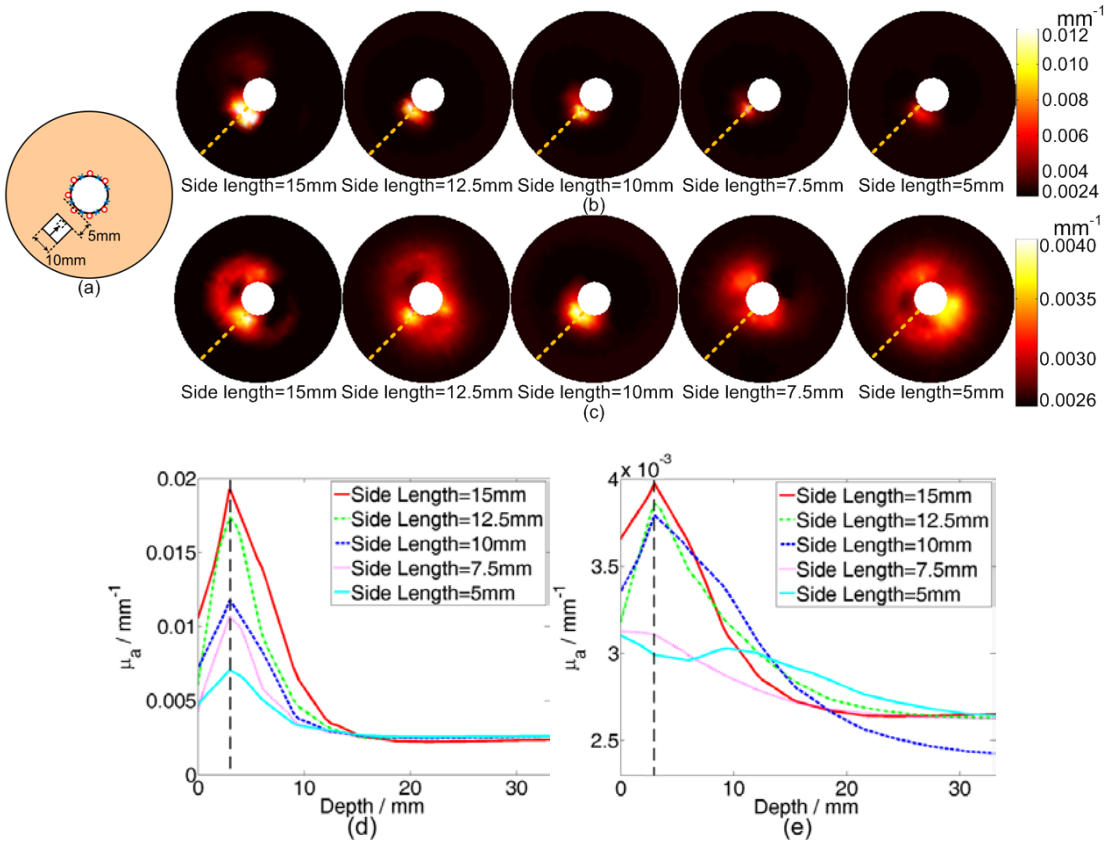

Fig.5.12 Experiment on system resolution on inclusion size. (a) Target location and size illustration (b) Reconstruction results on black plastic targets (c) Reconstruction results on synthetic phantom targets (d) Absorption coefficients plot along the dash lines in (b); (e) Absorption coefficients plot along the dash lines in (c)

As is expected and demonstrated by the results in Fig.5.12(b), black plastic materials are reconstructed with obviously higher optical absorption properties compared to the synthetic tissue phantoms. For all five target sizes, the targets made with black plastic are recovered at the same azimuthal location although the recovered volumes decrease with respect to those of the actual targets. For the targets fabricated from synthetic phantom, the absolute absorption values are close to the actual ones when the cubic volume is sufficiently large. However, targets with volumes less than $10\times10\times10$ mm^3 are overwhelmed by background artifacts.

To compare the absolute values of the recovered inclusions, the absorption values are plotted along the yellow dash line in Fig.5.12(b), as is shown in Fig.5.12(c). Fig.5.12(a) indicates that the target side to probe distance should be 5mm. However, as can be observed in the cross section plot, for targets made of both materials, the target centers are recovered at the depth of approximately 3mm. And the maximum absorption values decreases with the volume of the cubic phantoms, which should relate to the non-uniform sensitivity of the imaging geometry.

The second set of experiments examines the system sensitivity along the radial direction. A 10×10×10 mm^3 cube fabricated from black plastic is imaged at side-to-probe distances from 0mm to 15mm (equivalent center depths of 5mm to 20mm).

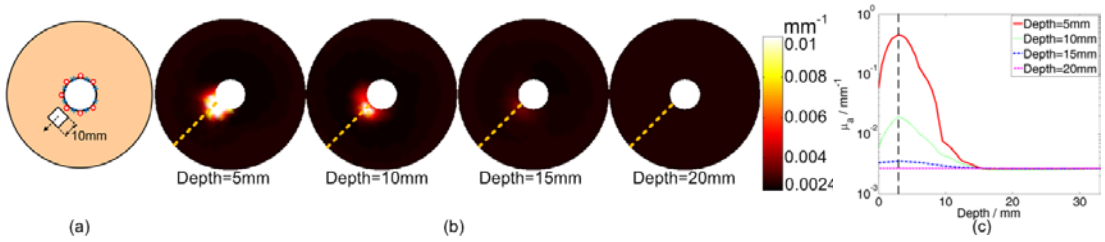

Fig.5.13 Experiment on system sensitivity along radial direction. (a) Target location and size illustration; (b) Reconstruction results on 10×10×10mm^3 black plastic targets; (c) Absorption coefficients plot along the dash lines in (b)

Recovered absorption distributions are shown in Fig.5.13(b) and the absorption values are again plotted along the probe radial direction. Results show that 1) the target cannot be recover beyond 15mm center depth; 2) the recover volume decrease as the depth increases; and 3) similar to experiment shown in Fig.5.12, all of the target centers are recovered closer to the probe at the depth of approximately 3mm instead of the actual varied depth up to 15mm.

However, it is expected that the reconstruction sensitivity should be uniform along the azimuthal direction of the probe in the image plane. Therefore, in the third set of experiments, the 10×10×10 mm^3 target is embedded 3mm away from the probe and rotated along the azimuthal direction, as is shown in Fig.5.14(a).

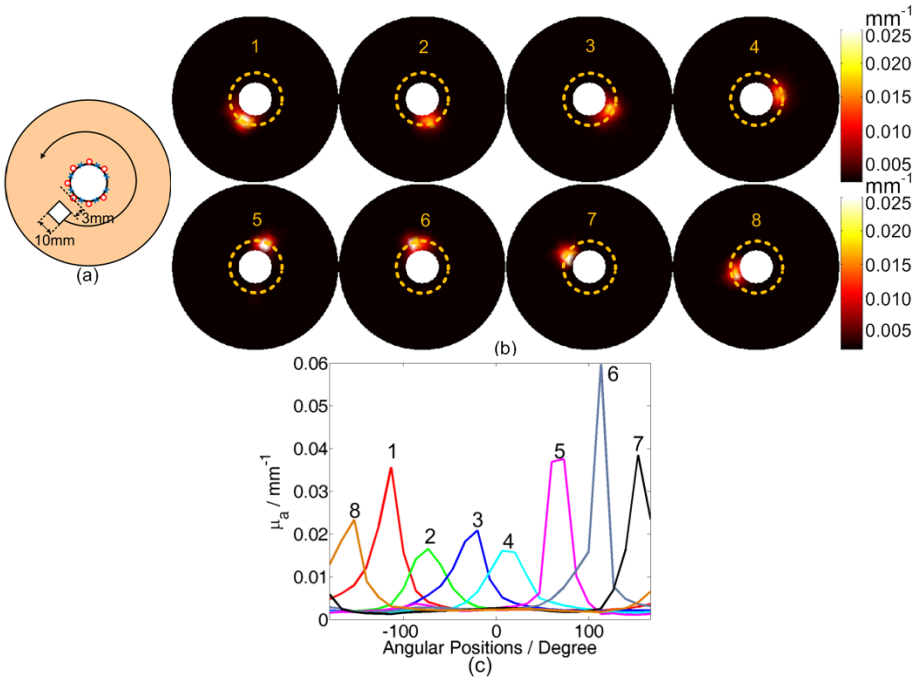

Fig.5.14 Experiment on system sensitivity along azimuthal direction. (a) Target location and size illustration (b) Reconstruction results; (c) Absorption coefficients plot along the dash lines in (b)

Approximately constant target volume and optical properties can be observed in Fig.5.14(b) as expected, and since the targets are located at the most sensitive region of the imaging geometry, the target depths are desirably recovered.

Absorption values are plotted along the 3mm deep circle off the probe (Fig.5.14(c)), as is delineated in Fig.5.14(b) by gold dash lines. Although the values fall into the same order, a maximum of 4 times absolute values difference is demonstrated. Factors such as the imperfection in probe fabrication, positioning error of the experiment system or calibration inaccuracy could contribute to such inconsistency.

The last set of experiments is designed to examine the system capacity of recovering multiple targets simultaneously. Two 7.5×7.5×7.5 mm^3 black cubes are used in this case in consideration that the center separation of larger targets is limited by their dimension and smaller targets are more difficult to be recovered. The two targets are both embedded 2mm away from the

probe (center depth = 2+7.5/2= 5.75 mm) at different angular positions with respect to the probe, as is shown in the Fig.5.15(a). Reconstruction results are shown in Fig.5.15(b).

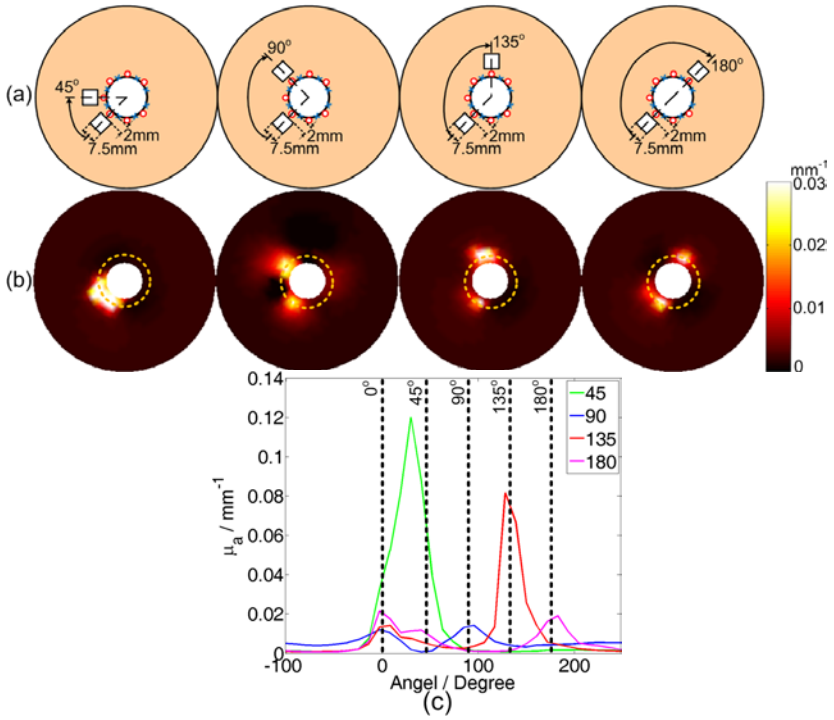

Fig.5.15 Experiment on recovery of multiple targets. (a) Target location and size illustration; (b) Reconstruction results; (c) Absorption coefficients plot along the dash lines in (b)

It can be observed that for the predetermined depth, angular separation beyond 90 degrees can be recovered accurately by the system. However, at 45 degree separation, the system cannot resolve the gap between the targets and indicates a large light absorbing blob at the correct location. Such result is expected, because the minimum angular separation of two neighboring sources is 45 degree and the signal intensity received by the detector between the two source channels could be substantially reduced by the two targets located in the dominant light propagation path tracing to the detector channel. Hence for the limited source-detector pair in this imaging geometry, reconstruction algorithm recognize the two sources and one detector channel within the 45 degree range as being blocked by one large light absorbing blob, as is shown by the first image in Fig.5.15(b) and the green curve in Fig.5.15(b). It should also be noticed that in the

135 degree separation case, the absorption value of the top target located at the same location as target 6 in Fig.5.14 is again overestimated.

5.8 Discussion & Future Work

All the four sets of experiments justified the feasibility of the system structure in recovering optical property contrast. By meticulous examinations of the reconstructed images, the system in most cases recovered the rectangular contour of the phantoms. Although the explanation to such phenomenon could intuitively relate to the element geometries of the finite element mesh used in reconstruction algorithm, it cannot be discovered in our previously reported studies [42] with almost identical mesh. Therefore, it can be inferred that the temporal and spectral encoding of the source light fundamentally reduces the source channel crosstalk between source channels, improving the imaging resolution of a predetermined imaging geometry.

Moreover, with the 4mW source power and 170ms exposure time, targets with center depth up to 20mm (Fig.5.13) can be detected. Although the previously reported broad-band spectral encoding system possesses higher total power level (20mW), the average power coupled to each source channel could be on the same level as or even lower than the system constructed in this study. The 0.5 frame per second data requisition rate could be dramatically raised by increasing the source power and but the source-by-source exposure pattern will become the ultimate upper limit to the frame rate. Further investigations will be conducted to explore the trade-off point between the broadband and swept source systems.

Temporal encoding of the novel system schematics can potentially extend the number of sources channel for a system with predetermined imaging sensor dimension. As is shown in Fig.5.5(a), for the 12.5mm×12.5mm sensor dimension utilized in this study, only 7 source channels with spectrally discernable displacement can be covered simultaneously. However, temporal encoding of the source light enables independent signal detection (Fig.5.9(a)) even though the source channels spectrally overlap (Fig.5.5(b)). Therefore, with rapid, temporally encoded wavelength swept, the identical system can acquire light signals from 14 channels (or

more by using low grooves per mm gratings) in a short time expansion. Such feature is especially beneficial for imaging scenarios with numerous source locations but require high signal acquisition frequency, for instance brain functional imaging[111], as is previously mentioned.

Calibration with analytical model is proved to be effective and accurate in the circular geometries, although fitting experimental data to the approximately evaluated model could be computationally intensive and impracticable with the gradient based algorithms. The more exhaustive heuristic random optimization approach [125] is implemented in two stages to the calibration process, which is validated by the experimental results. However, the analytical model utilized in this study cannot solve phase shift of light propagation in a cylindrical geometry, and the continuous wave measurement system also induces the less accurate scattering part calibration. It is expected that with frequency domain measurements and appropriate models, system calibration reliability can be improved, which contributes to more accurate estimation of the absolute optical property values.

Prospectively, the system structure can also substantially increase the data acquisition rate of fluorescence optical tomography [126-128]. Although simultaneous excitation of the fluorophor is achievable in multiple laser diodes and broadband spectral encoding systems, varied excitation wavelengths produces the same emission spectrum except the difference in fluorescence yield ratio, which is infeasible to separate by the CCD-spectrometer system at the detection end. Therefore, spectral encoding in optical tomography alone does not work in fluorescence tomography cases, and the prominent superiority in data acquisition rate of the novel temporal-spectral encoding combined system over the mechanical switching indicates the potentially implementation of such system structure in the immediate future work of this study.

5.9 Summary

A novel near infrared tomography system based on wavelength swept light source is constructed. 0.5 frame per second data acquisition rate is achieved, which can be potentially improved with more powerful light source and shorter CCD readout time. The system is

calibrated with analytical cylindrical photon diffusion model and the phantom experiment demonstrates that, the system with circular geometry can image targets with minimum target size of 5×5×5 mm^3, target-to-probe distance of 15mm and target angular separation of 45 degrees. The system scheme can be readily transformed for fluorescence optical tomography with appropriate source sweeping range.

The depth recovery inaccuracy problem shown by Fig.5.12 and Fig.5.13 will be further discussed and improved in the next chapter.

CHAPTER VI

A GEOMETRIC-DIFFERENTIAL-SENSITIVITY BASED ALGORITHM FOR DIFFUSE OPTICAL TOMOGRAPHY IN REFLECTANCE IMAGING GEOMETRY

6.1 Introduction

Diffuse Optical Tomography (DOT) is well-known for its unique functional imaging characteristics, as well as its complexity in terms of the quality dependence of image reconstruction upon a number of factors [57]. As the photon propagation through scattering-dominant regime is governed by a non-linear photon diffusion process, the sensitivity distribution of DOT, namely the change of boundary measurement in response to a change in medium optical properties, plays a dominating role in defining how well the heterogeneity of interest in the medium is to be recovered. A spectrally non-uniform sensitivity is preferred as it is what makes DOT functional. A spatially non-uniform sensitivity, however, is unfavorable due to the resulted non-uniformity in contrast, resolution, and particularly the biased localization of an occlusion toward the position of local sensitivity maxima [6, 8-11].

In DOT, the non-uniformity of the spatial sensitivity is also associated with the interfacing geometry between the array of optodes and the medium being interrogated. Usually the medium-array interface has one- or two-dimensional symmetry, e.g. azimuthal symmetry for evenly distributed optodes on a circular array, or lateral symmetries along two orthogonal directions on a near-planar surface with orderly distributed optodes. Along the direction of the symmetry,

the spatial sensitivity is uniform except at locations near the optodes; however, orthogonal to the direction of the symmetry, specifically along the depth into the medium, the spatial sensitivity varies, usually with the maxima at several steps of transport scattering from the medium-array interface. Such depth-dependent sensitivity distribution is particularly relevant to brain imaging [9, 129], breast imaging using planar remission geometry [10], and prostate imaging via endo-rectal probing for sagittal [11] or axial [42] imaging, etc.

Several studies have demonstrated image reconstruction strategies to mitigate the negative yield of spatially-variant sensitivity in DOT. For a circular-array geometry wherein the spatial sensitivity is azimuthlly uniform but radially variant, Pogue et al. applied radially variant regularization that corrected the radial variation in contrast and resolution and improved the depth localization as indicated by the centroid location of the target [8]. For a near-planar geometry of which the spatial sensitivity was more depth-dependent than that of circular-array concave-geometry, Culver et al. employed spatially-variant contras-to-noise-ratio weighting to the reconstruction, after the data was corrected for optode miss-positioning, to improve both the point-spread-function and the positioning in depth [129]. For similar near-planar geometry, Huang et al. [10], Niu et al. [6], and Zhao et al. [130] adjusted the magnitude of the sensitivity with respect to depth by introducing a weighting matrix to counterbalance the degradation of the spatial sensitivity in depth.

In this chapter, we demonstrate to our knowledge a novel image reconstruction method that has the potential to substantially improve the depth-localization in axial-translumenal imaging geometry, which arguably has the strongest degradation of sensitivity in depth among DOT geometries. This method, in lieu of modifying the penalty term of regularization versus depth or directly compensating the sensitivity matrix in depth, converts the conventional sensitivity profile that could be significantly depth-dependent to a surrogate sensitivity profile that is relatively depth-independent, by taking the differentiation of the sensitivities associated with multiple source-detector pairs to the same heterogeneity of interest.

6.2 Principles of Geometrical Differential Sensitivity reconstruction method

The principle of this method is illustrated conceptually in Fig. 6.1, for an axial-translumenal geometry with 8 sources and 8 detectors evenly interspersed along the array-medium interface as shown in (a). In this geometry, the sensitivity to an optical heterogeneity (e.g, of absorption) versus the depth is represented by the dashed curve shown in (b), with a near-boundary maximum followed by nearly-exponential decay in depth. When the image reconstruction is based upon such spatially-variant sensitivity, a target located at a greater depth (hence a smaller sensitivity) is either not to be recovered at all or to be reconstructed incorrectly in a near-boundary location. Alternatively for an optical heterogeneity at a fixed depth, the shown sensitivity profile resembles the sensitivity of a series of detectors along the circumference, with respect to the same source that is azimuthally closest to the heterogeneity of interest. A differentiation between the sensitivities of two neighboring and source-sharing source-detector pairs to the same heterogeneity carries the same information as the non-differentiated sensitivity does, however with the variation over the depth significantly reduced, as is shown by the solid curve in (b).

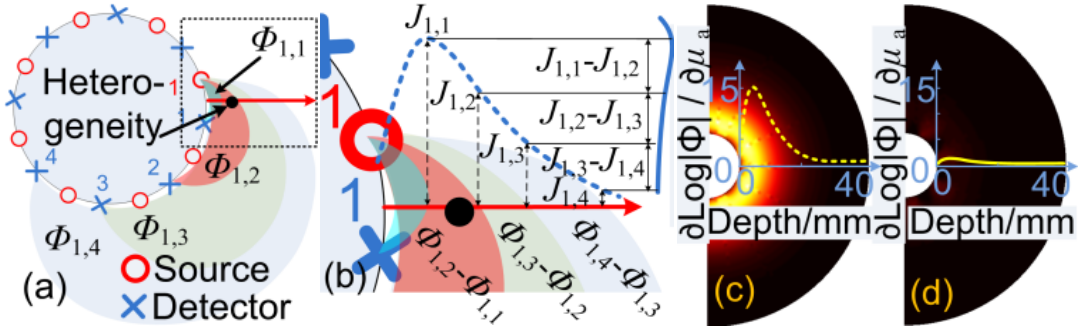

Fig.6.1. Conceptual illustration of the principle. (a) Imaging geometry; (b) Magnified area of the dotted box in (a); Depth-dependences of the conventional (c) and geometric-differential (d) sensitivity profiles, respectively.

Analytically, the conventional objective function to be minimized during DOT image reconstruction for a pair of source i and detector j, denoted by $\{i, j\}$, can be expressed as

$$\Delta\Psi^{\{i,j\}} = \left\| \Phi_c^{\{i,j\}} - \Phi_m^{\{i,j\}} \right\|^2 = \left\| J_{1\times 2N}^{\{i,j\}} \cdot \delta\mu_{2N\times 1} \right\|^2 \tag{6.1}$$

where $\Phi_c^{\{i,j\}}$ and $\Phi_m^{\{i,j\}}$ are the calculated and measured photon fluence rates, respectively, $\delta\mu_{2N\times 1}$ is the updates of the optical properties (assuming absorption coefficient μ_a and reduced scattering coefficient μ_s' only) at the total N nodes, and $J_{1\times 2N}^{\{i,j\}}$ is the conventional sensitivity matrix associated with source-detector pair $\{i, j\}$. We now construct a surrogate sensitivity matrix,

$$\tilde{J}_{1\times 2N}^{\{i,j,k\}} = \left(\tilde{J}_{1\times 2N}^{\{i,j\}} - \tilde{J}_{1\times 2N}^{\{i,j+k\}} \right)_{i=1:Nos,\ k=1:Nod-1,\ j=1:Nod-k} \tag{6.2}$$

where k is the difference between the serial numbers of the detectors, "*Nos*" is the number of source channels, and "*Nod*" is the number of detector channels. We call this method a geometric-differential sensitivity (GDS) approach. The image reconstruction is then to optimize a surrogate objective function, as expressed by

$$\Delta\tilde{\Psi}^{\{i,j,k\}} = \left\| \tilde{\Phi}_c^{\{i,j,k\}} - \tilde{\Phi}_m^{\{i,j,k\}} \right\|^2 = \left\| \tilde{J}_{1\times 2N}^{\{i,j,k\}} \cdot \delta\mu_{2N\times 1} \right\|^2 \tag{6.3}$$

Note that in equ (6.2) a sign change of the resulted term $\tilde{J}^{\{i,j,k\}}$, represented by $\tilde{J}^{\{i,j,k\}} \Leftarrow -\tilde{J}^{\{i,j,k\}}$, is necessary if

$$\{k>Nod/2\} \text{ or } \{k= Nod/2 \ \&\ i<k \ \&\ j<i\}$$
$$\text{or } \{k= Nod/2 \ \&\ i>k \ \&\ j+k\geq i\}\}. \tag{6.4}$$

The profile of the rearranged surrogate sensitivity $\tilde{J}$, after column-wise summation, is like the one shown in Fig. 6.1(d) versus the profile of the conventional sensitivity J in (c).

The sensitivity profiles in Fig. 6.1(c) and (d) are calculated using NIRFAST [86]. The imaging geometry has an array radius of 10mm and a domain radius of 50mm. The finite element mesh representing the imaging domain includes 7708 evenly distributed nodes and 15040 elements with the Robin-type boundary condition. The dynamic range of the introduced GDS profile over the depth is approximately 1/10 of that of the conventional sensitivity profile over the same depth. The nearly depth-independence of the surrogate sensitivity profile is expected to lead to much improved depth localization when compared to the substantial depth-degradation of the

conventional sensitivity profile. However, due to the increase in the matrix size the expected improvement in depth-localization by GDS approach is to be accompanied by an increased demand in computation time.

6.3 Simulation and experiment validations

6.3.1 Validations in an endoscopic circular geometry

The GDS image reconstruction is first evaluated by both simulation and experimental studies in the geometry for shown in Fig. 6.1 and Fig. 6.2(a). The 20-mm diameter applicator [42] has 16 evenly distributed channels for 8 sources interspersing with 8 detectors. However, due to poor-coupling of micro-optical elements in one source channel (marked in Fig. 6.2(c)), 7 source channels and 8 detector channels are implemented for the study.

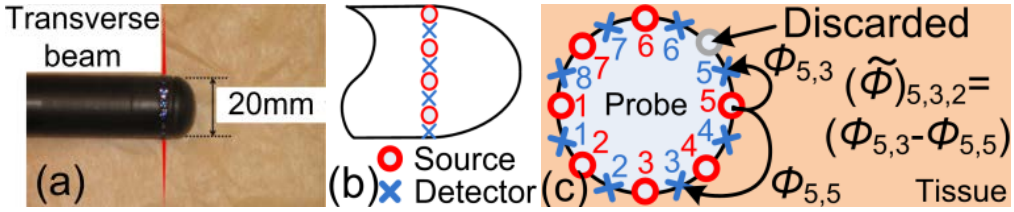

Fig.6.2. Imaging geometry. (a) Probe Photography; (b) Side-view of source-detector layout; (c) Axial view and illustration of $\tilde{\Phi}^{\{i,j,k\}}$ in equ. (6.3).

The optical parameters employed for the simulation were chosen based on experimental studies. Specifically, the background had μ_a=0.0023 mm^{-1} and μ_s'=1mm^{-1} corresponding to 1% bulk intralipid solution at 840nm. Optical heterogeneity was introduced by use of one or two black-plastic cubes, whose sharp and strong contrast over the background medium was necessary to evaluating the edge-spread-function for depth-localization. The cube-heterogeneity was treated as having μ_a= 0.0115 mm^{-1}, or five times of absorption contrast over the back-ground, and μ_s'= 1.1mm^{-1}. A small scattering contrast was assigned to mitigate the potential cross-coupling between μ_a and μ_s'. A 1% white noise was added to all forward data.

The results of reconstructing a single cube-target of 12mm edge-length as parameterized above are shown in Fig. 6.3. The array-facing-edge of the cube was located 0, 5, and 10mm away

from the optical array, or equivalently with the center depths of 6, 11, and 16 mm, respectively. The results of the conventional and GDS methods on simulated and experimental data are displayed column-wisely, with the actual location of the cube marked with dotted square. In addition, the radial profiles along the green dotted lines crossing the cube location are compared for each row in logarithmic scale, as is shown in the "Contour Plots".

It is observed in simulation that both conventional and GDS methods are capable of recovering targets at depths of 10mm. However, GDS has much better localization of the depth of the target. In the experimental study, the recovering of the target at edge-depths of 0 and 5 mm by the two methods is comparable to that shown by simulations, whereas the GDS has noticeably better depth-localization of the array-facing edge of the cube. At edge-depth of 10mm, neither of the methods could identify the target at the correct location, however, the artifact by GDS method is negligible comparing to that by the conventional method.

The contour plots in Fig. 6.3 imply that in both simulation and experiment, the absorption values recovered by GDS method for different target-depths are all in an interval between e^{-6} to e^{-5}, whereas the absorption values recovered by the conventional method vary in a much greater range. The narrow range of absorption contrast demonstrates an additional aspect of improvements by the GDS method.

The better estimation of the target location by the GDS method over the conventional sensitivity method is also expected to result in better estimation of target volume when multiple targets are to be resolved. Fig. 6.4 demonstrates simulation and experimental studies of resolving two black-plastic cubes of 10mm edge-length. The array-facing edges of the cube targets are placed 1mm away from the probe (corresponding to a center depth of 6mm), and the angular separation between the two targets was approximately 90 degrees. The medium conditions and the optical properties assumed for the two cube-targets are the same as those in Fig. 6.3. The actual target locations are marked by blue dotted line in Fig. 6.4(a)-(d). Along the azimuthal cross section of the imaging geometry as is marked with green dotted circles, the recovered absorption

coefficient profiles are displayed in Fig. 6.4(a)-(d), after normalization to the peak of the extracted profile as plotted in Fig. 6.4(e). Simulation results indicate that even though both conventional and GDS methods are able to resolve the two targets, GDS method separates the targets more distinctly. The conventional method based on the experimental data, however, failed to clearly discern the targets due to the affinity of the two peaks, yet the GDS method resolves the two targets at the correct locations with good contrast over the background medium.

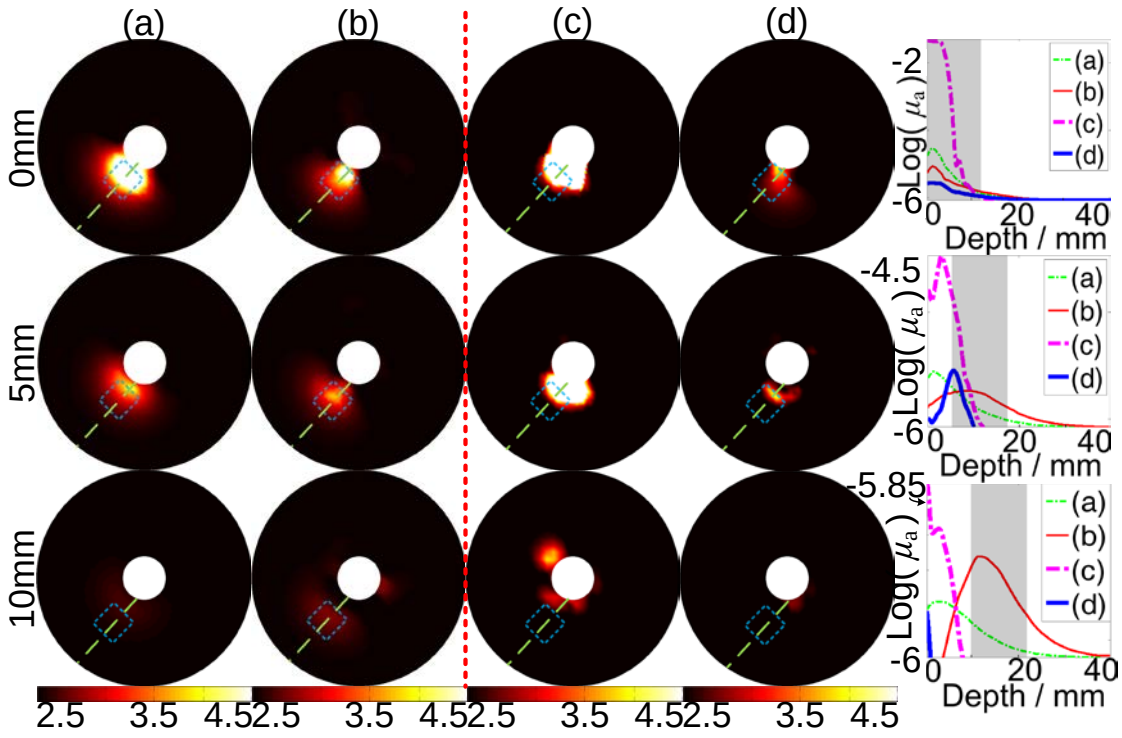

Fig.6.3 Simulations and phantom experiments examining target depth recovery (Unit:10^{-3}·mm^{-1}). Columns (a) and (b): simulation results by conventional and GDS methods,respectively. Columns (c) and (d): experiement results by conventional and GDS methods, respectively.Blue dotted squares indicate target positions. Contour plots are absorption profiles along the green dotted lines in the reconstruction images. Shaded area in Contour Plots indicates the target locations. GDS shows clear improvement in target depth localiazation and volume estimation.

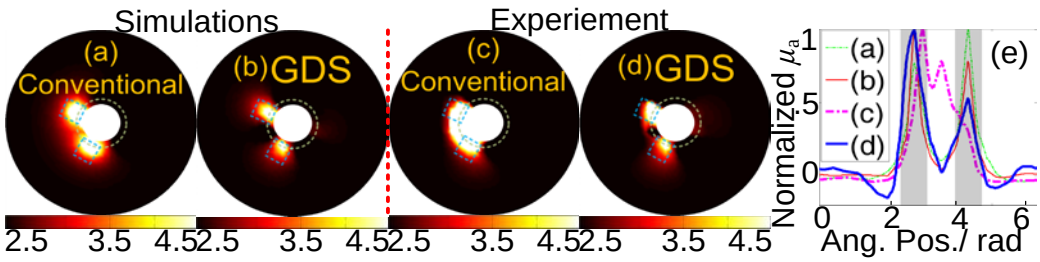

Fig.6.4 Simluation and phantom studies on resolving two targets. (Unit:10^{-3}·mm^{-1}). (a)-(d) reconstruction images; Blue dotted square indicate the target positions; (e) Absorption contour plotted along the green dotted lines in (a)-(d), shaded area indicating the targets.

6.3.2 Validations in an planar imaging geometry

The image reconstruction based on the GDS approach is also evaluated by simulation in a planar imaging geometry as is shown in Fig. 6.5. As is shown in Fig.6.5, the optical array has a dimension of 50mm by 50mm, with 18 sources and 18 detectors evenly interspersed in a plane with minimum source-detector distance of 10mm. Imaging depth of half the extension of the imaging geometry, 25mm, is expected in the simulation study.

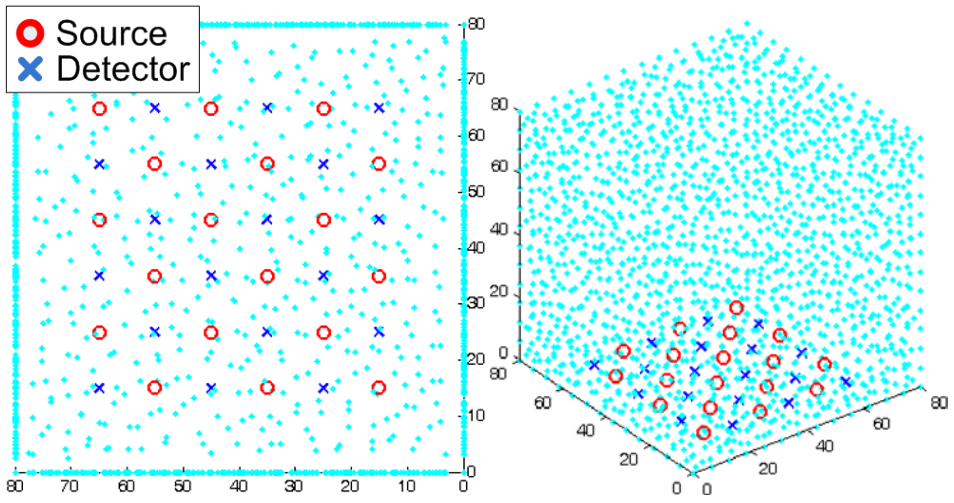

(a) (b)

Fig. 6.5 A planar imaging geometry.

(a) optode array (b) simulation geometry

As is shown in Fig. 6.5(b), the optical array is assigned at the bottom of an $80\times80\times80mm^3$ volume. Simulations examines the depth recovery of single target is shown in Fig. 6.6. The optical properties of the background are set as: μ_a=0.0023 mm^{-1} and μ_s'=1mm^{-1}. The targets are 5 mm radius blobs with μ_a=0.006 mm^{-1} and μ_s'=2mm^{-1}. In the single target cases, the targets are embedded at center-depths of 5mm to 25mm at the step size of 5mm.

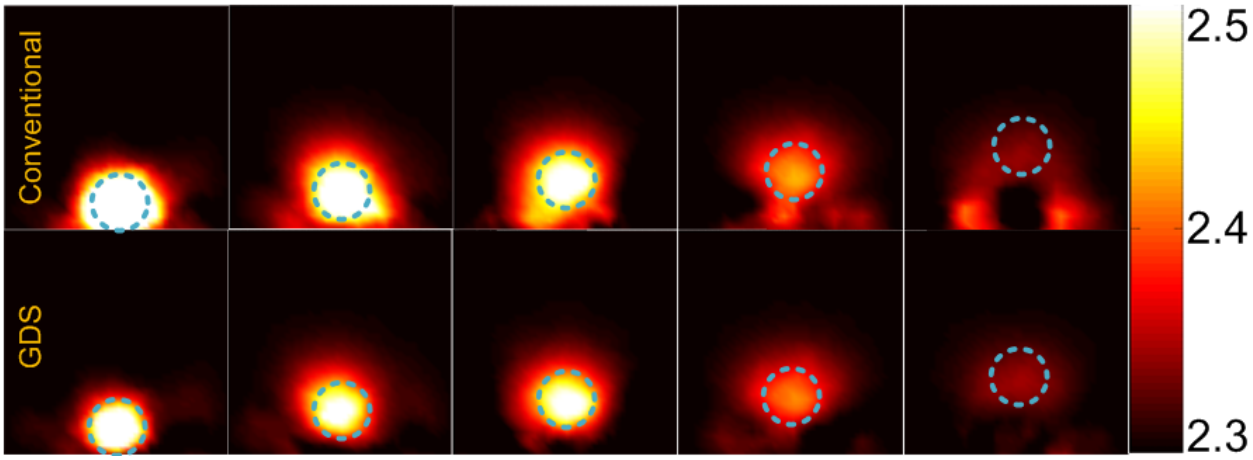

Fig.6.6 Simulation validation of GDS in the geometry shown in Fig.6.5

Fig.6.6 demonstrates without sacrificing the recovered target contrast, GDS methods can identify the target depths up to 25mm.

6.4 Summary

This chapter introduced a geometric-differential sensitivity approach for DOT image reconstruction. The method employs a surrogate objective function [131] that rescales the solution domain of the inverse problem while maintaining the solutions of the original objective function. The rescaled inverse problem produces minimal spatial sensitivity variation and consequently more accurate depth-localization and volume-estimation of the target. The advantage of GDS approach over reconstruction based on conventional sensitivity profile was demonstrated by simulations and phantom studies of localizing and resolving one or two sharp-contrast targets. The better suppression of artifacts by the GDS approach is also likely related to

the cancellation of common uncertainty factors in measurements, similar to that demonstrated in a spectral-derivative algorithm [132].

Because of the structural similarity of the sensitivity matrix, this algorithm could also be extended to fluorescence-enhanced diffuse optical tomography in geometries suffering significant depth-degrading sensitivity. The transformation of the conventional sensitivity matrix to the GDS approach, however, is accompanied by an increase in the element number in the objective function due to the increase of the number of row vectors in sensitivity matrix from m×n to m×n×(n-1)/2. It is found in this study that the total computation time of executing the GDS method is approximately 40% more than using the conventional method.

CHAPTER VII

ENHANCING DIFFUSE OPTICAL TOMOGRAPHY FOR PROSTATE CANCER IMAGING WITH ZINC-SPECIFIC FLUORESCENCE BIOMARKER

7.1 Introduction ---Zinc as a cancer biomarker for prostate imaging

As is introduced in the first chapter of this report, the optical contrast and localization can be substantially increased by the administration of fluorescence emitting agent, which can be followed by trans-rectal imaging, allowing oncologists or urologists seeing the position and extent of the adenocarcinomas of the prostate, and both diagnosis and the planning of surgery could be dramatically improved over the present methods.

Zinc is actually well established as a metabolic biomarker for prostate cancer, with changes of at least an order of magnitude in the marker concentration accompanying adenocarcinoma of the prostate. The prostate gland secretes about 10 mM of zinc into prostatic fluid, which is the second-highest concentration found in nature. The zinc secretion of the epithelial cells is biologically analogous to zinc secretion by neurons [133], Paneth cells [134], salivary cells [135] and breast epithelial cells [136], with similar transporters sequestering the zinc in the secretory granules [137]. The biological function of the zinc secreted by the prostate epithelial cells is, in short, controlling the time-release of the spermatozoa from the coagulum, in vivo. It is also known that a 10-fold molar excess of citrate is co-secreted with the zinc, thus keeping the zinc in solution as $Zn_3Citrate_2$.

The fact that zinc sequestering and secretion are suppressed in adenocarcinomas was first suggested in 1952 [138] and has been consistently documented in more than a score of studies since then. Probably the most thorough study to date of the secretory granule sequestration of zinc has shown that the transporter (ZnT-4) is suppressed up to 2-4 mm from the margin of adenocarcinoma, in otherwise histologically normal acini [139]. It is important to note that the average level of zinc in ejaculate and prostate fluid is reduced by 5- to 10-fold in cancer[140]. Zinc functions as a specific bio-marker to the prostate cancer.

By implementing trans-rectal NIR imaging of prostate cancer biomarker such as the zinc using fluorescence tomography measurement, the detection can be made much more specific. There are few of the fluorescent zinc indicator systems excitable in the infrared, except by multi-photon excitation. NeuroBioTex has demonstrated zinc determination using carbonic anhydrase (CA)-based system using infrared two-photon excitation [141], but the millimeter penetration depth of two-photon excitation (due to pulse spreading, not absorption) as well as the poor transmission of the visible fluorescence will be insufficient for the centimeter-range thickness of the prostate.

The major challenge of zinc-based prostate fluorescence tomography lies in the fact that the condition of the detection is to image a fluorescence - weak target within fluorescence - strong environment. This is an inverse-uptake FDOT problem, because the normal or benign prostate tissue, being zinc-rich, will have higher fluorophore concentration compared to the zinc-poor cancerous tissue if the fluorophore is specific to free-zinc. This research will become the first quantitative study of such unique FDOT conditions. Theoretically, the sensitivity distribution of an imaging system is not subject to the optical contrast (either positive or negative) of the inclusions. But if considering that the measurement fluctuation produced by a fluorescence emitting background will definitely succeed that produced by a small blob-like fluorescence target, larger PRUL are expected in the imaging scenario of negative uptake fluorescence optical tomography.

7.2 Simulation studies

The simulation study utilized 2-dimensional finite element method for steady state photon diffusion and fluorescence emission:

$$\nabla^2 U_x(\vec{r}) - \frac{\mu_{ax}}{D_x} U_x(\vec{r}) = -\frac{S(\vec{r})}{\nu D_x}, \quad \nabla^2 U_m(\vec{r}) - \frac{\mu_{am}}{D_m} U_m(\vec{r},\omega) = -\frac{U_x(\vec{r}) \cdot \eta \mu_{af}}{\nu D_m} \tag{7.1}$$

where subscripts "x" denotes excitation and "m" denotes emission. The diffusion coefficient $D_{x,m}=1/[3(\mu_{ax,m}+ \mu_s'_{x,m})]$, where $\mu_{ax,m}$ and $\mu_s'_{x,m}$ are absorption and scattering coefficients for excitation and emission band, respectively. The η and μ_{af} are the quantum efficiency and the absorption coefficient of the fluorophore respectively, the product of which is defined as the fluorescence yield. The forward solver implements the Robin type boundary condition as:

$$U_{x,m}(\vec{r}_0) + 2D_{x,m} A \hat{n}_0 \cdot \nabla U_{x,m}(\vec{r}_0) = 0 \tag{7.2}$$

where $\vec{r}_0$ is the boundary nodes, $\hat{n}_0$ is the outward normal vector of the boundary and A is the refractive index mismatch coefficient. The Levernberg-Marquart algorithm is implemented as the inverse solver as:

$$x_{k+1} = x_k + \alpha \cdot [J^T(x_k) J(x_k) + \lambda I]^{-1} J^T(x_k) \Delta v(x_k) \tag{7.3}$$

where α in the range of [0,1] is a damping factor , J is the sensitivity matrix and Δv is the forward projection error. When only the contrast of florescence yield is considered, the unknown values x represents the $\eta_{\mu af}$ term in equ.(7.1).

7.2.1 Feasibility of recovering only reverse fluorohpore uptake in endoscopic imaging geometry

In this section, only the contrast of fluorescence yield is considered, by setting η=0.1, μ_{af}=0.005 for the target and η=0.1, μ_{af}=0.01 for the background. Other parameters are set as: $\mu_{ax,m}$=0.01mm-1, $\mu_s'_{x,m}$=1mm^{-1} and A=2.82. 1% Gaussian noise is added to the simulated forward data.

7.2.1.1 Region-wise reconstruction

The region-wise reconstruction is first simulated to assess the accuracy of recovering a "reverse-uptake" fluorescence target with accurate *prior* knowledge of the target spatial information, including shape, size, and depth. Supposing that the accurate profile of the structures within the imaging volume can be accurately extracted from the complementary imaging modality such as TRUS and MRI, and assuming homogeneity of optical properties and fluorescence yield within each segmented region, the so called "hard" *a priori* reconstruction algorithm [11] is modified for FDOT.

Simulation approaches are shown in Fig.7.1. Targets with the radius shown in Fig.7.1 (a) and (c) are set at a depth from the source-detector array at an increment of 5mm (Fig.7.1(a)). Notice that for r>5mm, the round target at 5mm depth is interfered by the inner boundary of the imaging volume, therefore the target shape must be modified at that specific depth. The comparison of the recovered fluorescence yield within the target region is given in Fig.7.1(c).

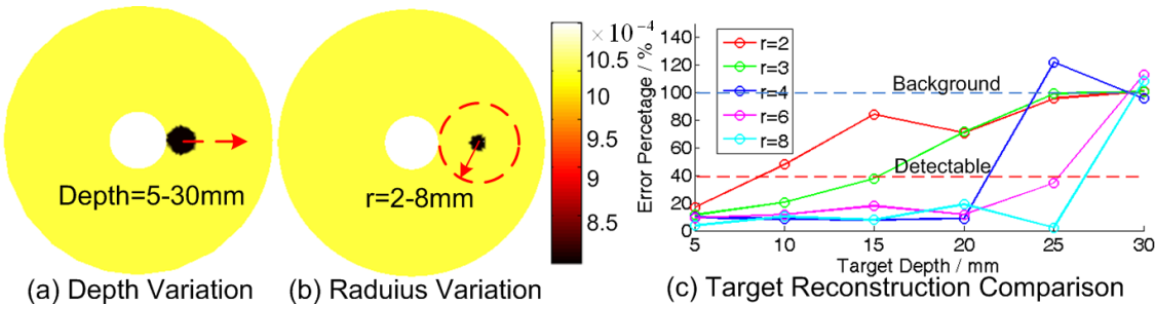

Fig.7.1 Region-wise reconstruction

40% error tolerance is set as the threshold for the target recovery. It is observed that, (1) The detectable depth increases as the target size increases; (2) the imaging depth of 15-20mm is attainable for this imaging geometry for most of the target sizes; (3) the recovered fluorescence yields of all targets converge to the background ((0.001-0.0005)/0.0005=100%) values at 30mm depth, which is the detection limit.

7.2.1.2 Piece-wise reconstruction

The above region-wise reconstruction is only an ideal case. Piecewise reconstruction is more practical because of the lack of accurate target information when TRUS is used to visualize

the prostate morphology. When no spatial *prior* information of the target can be implemented, the axial trans-rectal imaging will be challenged by the depth-dependent sensitivity inherent to the side-firing reflective imaging geometry. To compensate the sensitivity distribution, an adaptive mesh is implemented [142]. As is shown in Fig.7.2(a)(c), with the notion that the uniformity of the product of relative sensitivity value and the element size within the imaging volume contributes to the correction of depth dependent sensitivity [13], the element sizes are adjusted according to the depth-sensitivity. Further, since in this axial-imaging geometry, when there is only one target, the approximate azimuthal location and dimension may be indicated by the change of the signal with respect to the baseline, the approximate target area can be segmented into denser elements. Fig.7.2 shows the meshes generated with: (b) uniform element size (c) depth-adapted elements, and (d) depth and azimuth adapted elements.

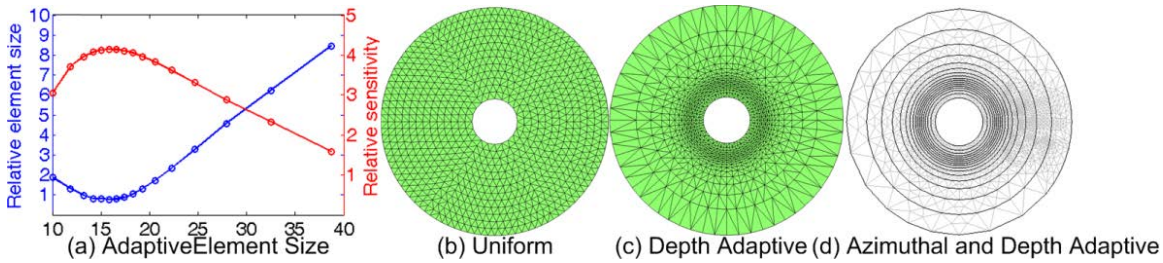

Fig.7.2 Adaptive meshes (a) element-size vs. depth-sensitivity; (b) uniform mesh;

(c) depth-adapted elements; (d) depth and azimuth-adapted elements

A target located close to the array boundary is simulated to assess the efficacy of the adaptive mesh elements shown in Fig.7.2. Fig.7.3 (a) shown a 5mm radius target with η=0.1 and μ_{af}=0.01 at x=5mm,y=0mm. The results in Fig.7.3 (b)-(d) demonstrate that the depth-and-azimuth adapted mesh slightly outperforms the depth-adapted mesh, and the depth-adapted meth significantly outperforms the uniform mesh, but all methods are associated with artifacts.

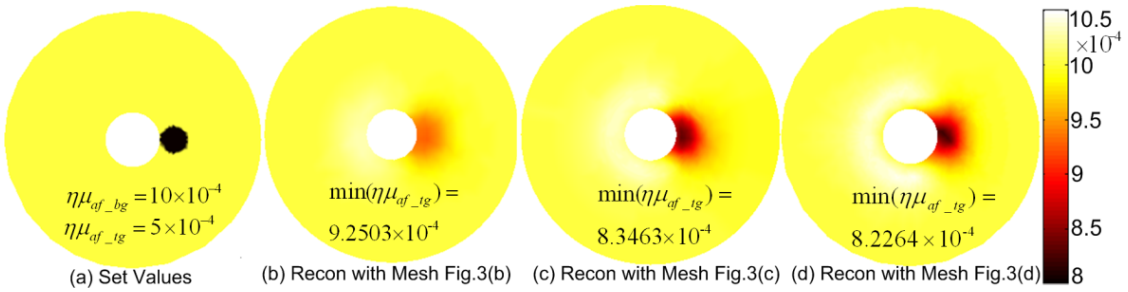

Fig.7.3 Piece-wise reconstruction. (a) Target setting (b) uniform mesh; (c) depth-adapted mesh; (d) depth and azimuth-adapted mesh

7.2.2 Piecewise reconstruction in prostate imaging geometry

7.2.2.1 Reconstructing only the fluorescence uptake

Trans-rectal prostate optical imaging, either absorption based or fluorescence based, is challenged by image reconstruction in a multiply -nested tissue domain.

Previous studies on diffuse optical tomography have shown that the piecewise reconstruction of such nested structure may be prone to artifacts and non-unique solution for the optical property values. The hierarchical reconstruction routine based on hard *prior* method has been modified for initial investigation on fluorophor absorption contrast in the imaging volume. The imaging geometries are directly adopted from the ones used in previous works [2, 11] and the results are shown in Fig.7.4. Only the fluorescence absorption part is shown in the figures because for both the negative and positive contrast cases, the optical properties of the tissue with respect to the excitation and emission bands are set as homogeneous for the entire imaging volume: μ_{ax}= μ_{am}=0.01mm^{-1}, μ_{sx}'= μ_{ax}'=1mm^{-1}. The fluorescence yield for the negative contrast case at the cancer is set at $\eta\mu_{af}$ =4×10^{-5}mm^{-1}, and for the positive case, $\eta\mu_{af}$= 6.4×10^{-4} mm^{-1}. And the fluorescence field of the prostate tissue 1.6×10^{-4}mm^{-1}, for the tissue surrounding prostate, $\eta\mu_{af}$=8×10^{-5}mm^{-1} and for the rectum wall, $\eta\mu_{af}$=1×10^{-4}mm^{-1} At this simulation fluorescence uptake ratio of only 4:1 is used, actually, for the positive contrast case, uptake ratio may range from 2.5:1 to 1000:1 [15]. For the negative contrast cases in this research, the zinc-specific biomarker uptake ratio of background to the target is still unknown, but we could expect the value

to be as high as 200:1 according to the zinc concentration ratio between the normal and malignant tissue, which could be very challenging. Fig.7.4 gives the results of reconstructing the fluorescence-yield using hierarchical spatial *prior* approach providing that the spatial *prior* is accurate. It can be observed from the comparison diagram that steady-state measurements of the fluorescence and hierarchical reconstruction routine, can reliably recover the fluorophore concentrations.

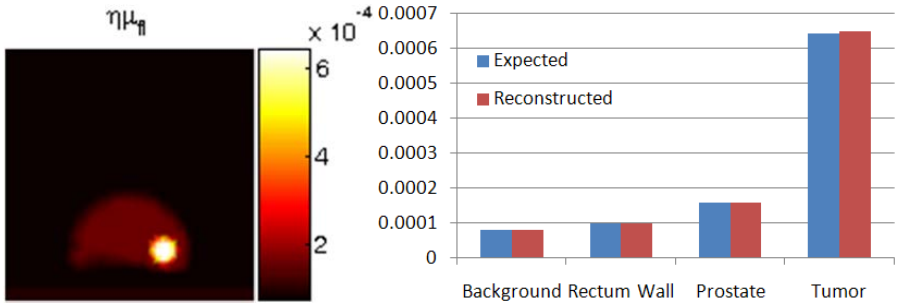

(a) Reconstructed fluorescence yield—positive contrast (b) Bar plot comparison

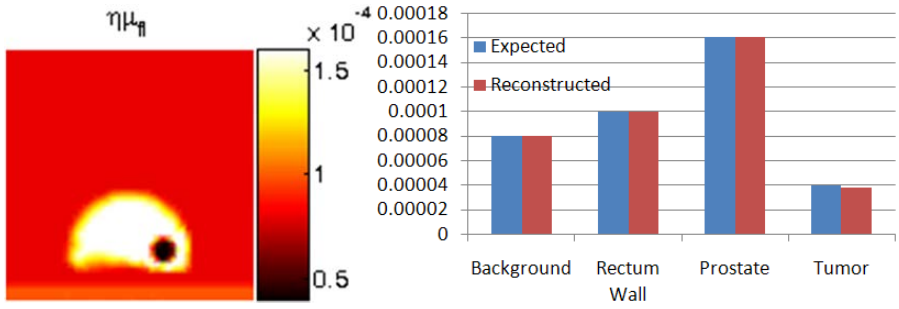

(c) Reconstructed fluorescence yield—negative contrast (d) Bar plot comparison

Fig.7.4 FDOT with hard *a priori* reconstruction

However, for practical experimental examination, the simplest case of imaging one or two occlusion within a homogeneous background is adopted. Piecewise steady state reconstruction algorithm will be coded in MATLAB based on the inverse problem of frequency domain systems. Further, considering the non-uniform sensitivity distribution of FDOT, compensation methods including adaptive mesh and sensitivity normalization will also be attempted for reconstruction accuracy improvement. The preliminary simulation results are shown below.

7.2.2.2 Simultaneous reconstruction of optical properties in emission band and fluorophore uptake contrast with spatial prior

Before presenting the details of our improvement to the region-wise reconstruction algorithm, we would like to review the basis of FDOT reconstruction. Fluorescence optical tomography usually models the propagation of excitation and emission light by

$$\nabla \cdot D_x(\vec{r})\nabla\Phi_x(\vec{r},\omega) + [\mu_{ax}(\vec{r}) + \frac{i\omega}{c}]\Phi_x(\vec{r},\omega) = q_{0,x}(\vec{r},\omega) \tag{7.4}$$

$$\nabla \cdot D_m(\vec{r})\nabla\Phi_m(\vec{r},\omega) + [\mu_{am}(\vec{r}) + \frac{i\omega}{c}]\Phi_m(\vec{r},\omega) = q_{0,m}(\vec{r},\omega) \tag{7.5}$$

$$\nabla \cdot D_m(\vec{r})\nabla\Phi_m(\vec{r},\omega) + [\mu_{am}(\vec{r}) + \frac{i\omega}{c}]\Phi_m(\vec{r},\omega) = \Phi_m(\vec{r},\omega)\eta\mu_{af}(\vec{r})\frac{1 - j\omega\tau(\vec{r})}{1+[\omega\tau(\vec{r})]^2} \tag{7.6}$$

Where subscript "x" and "m" represents excitation and emission, respectively. Φ is the photon fluence rate. D is the diffusion coefficient and μ_a is the absorption coefficient. $\mu_{af} = \varepsilon_{fl} \cdot c_{fl}$ is the fluorophore absorption coefficient, where ε_{fl} and c_{fl} are the extinction molar coefficient and concentration of the fluorophore, respectively. η and τ are the fluorophore quantum efficiency and life time, respectively. q_0 is the source term. $\vec{r}$ and ω are the pixel position vector and modulation frequency of the source light.

Equations (7.4) and (7.5) are usually written together in most literatures, as the differences only existed in the subscripts of "x" or "m". However, more accurate FDOT reconstruction should include the following procedures:

- To implement source light at the excitation band ($q_{0,x}$) and collect diffused light signal at the excitation band (Φ_x at tissue boundaries) and recover absorption and diffusion coefficient distribution (μ_{ax} and D_x) at the excitation band.
- To implement source light at the emission band ($q_{0,m}$) and collect diffused light signal at the emission band (Φ_m at tissue boundaries) and recover absorption and diffusion coefficient distribution (μ_{am} and D_m) at the excitation band.

- To implement source light at the excitation band ($q_{0,x}$) and collect fluorescence emission signal at the emission band (Φ_m at tissue boundaries) and recover fluorescence yield and life time distribution ($\eta\mu_{af}$ and τ) at the excitation band.

Note that the emission band signals in the second step are generated by external source light at the emission band, whereas those in step three are generated by fluorophore. The first two steps can be replace by multi-spectral DOT measurements and reconstruction for more reliable determination of $\mu_{ax,m}$ and $D_{x,m}$ values. However, such arrangement requires external light sources at more wavelengths.

As region-wise reconstruction in FDOT is over-determined at most cases, the unknown parameters in step two (μ_{am}, D_m) can be solved simultaneously with those in step three ($\eta\mu_{af}$ and τ). Such arrangement in image reconstruction actually reduces the complexity of FDOT system, as the external source light at the emission band is no longer necessary. The reconstruction is therefore reduced to two steps:

- Implement source light at the excitation band ($q_{0,x}$) and collect diffused light signal at the excitation band (Φ_x at tissue boundaries) and recover absorption and diffusion coefficient distribution (μ_{ax} and D_x) at the excitation band.
- Implement source light at the excitation band ($q_{0,x}$) and collect fluorescence signal at the emission band (Φ_m at tissue boundaries) and recover absorption/diffusion coefficient distribution (μ_{am} and D_m) and fluorescence yield/life time distribution ($\eta\mu_{af}$ and τ) at the excitation band.

We only utilize DC fluorescence measurements for reconstruction, $\omega=0$ and $\tau=0$ in equ. (7.4)-(6).The Jacobian structure of the first step is constructed following the conventional method and we structured the sensitivity matrix (Jacobian) in the second step following equ. (7.4):

$$\begin{bmatrix} \frac{\partial \ln I_{11}}{\partial \mu_{am}} & \frac{\partial \ln I_{11}}{\partial D_m} & \frac{\partial \ln I_{11}}{\partial \eta \mu_{af}} & \frac{\partial \ln I_{11}}{\partial \tau} \\ \frac{\partial \ln I_{12}}{\partial \mu_{am}} & \ddots & \ddots & \vdots \\ \vdots & \ddots & \ddots & \vdots \\ \frac{\partial \ln I_{77}}{\partial \mu_{am}} & \cdots & \cdots & \frac{\partial \ln I_{77}}{\partial \tau} \end{bmatrix} \tag{7.7}$$

And the sensitivity matrices are substituted into Levernberg-Marquardt method for iteratively solving the unknown values.

$$x_{k+1} = x_k - [J^T(x_k)J(x_k) + \mu I]^{-1} J^T(x_k) v(x_k) \tag{7.8}$$

The region-based reconstruction is simulated in Fig.7.5 for the case of the target haing positive optical contrast over the background but negative-contrast of fluorescence-yield, and in Fig. 7.6 for the case of the target having negative optical contrast over the background and negative-contrast of fluorescence-yield. The imaging domain is a 80mm×80mm×80mm cube. Substructures are segmented according to the presumed spatial *prior*. The optical array includes 7 sources and 7 detectors, arranged in parallel rows at the bottom of the imaging geometry. The (b)-(f) of Fig. 7.5 and 7.6 shows the optical properties assignment of the two cases of medium-target. We assume the optical properties are accurately determined in step one and only the second step is simulated. μ_{ax}=0.006, μ'_{sx}=1. The fluorescence quantum efficiency is set to 0.1 for all regions. The reconstruction initial values are set as: μ_{am} =0.01, μ'_{sm} =1 and $\eta\mu_{af}$ =0.0001. Table 7.1 and 7.2 compares the assigned and the reconstructed values of . Note that the scattering coefficients ($\mu'_{sx,m}$ =1/(3· $D_{x,m}$)- $\mu_{ax,m}$) are shown instead of showing $D_{x,m}$.

In Table 7.1 and 7.2, although the reconstructed values do not agree exactly with the set values, the relative positive or negative contrasts among the regions are accurately identified.

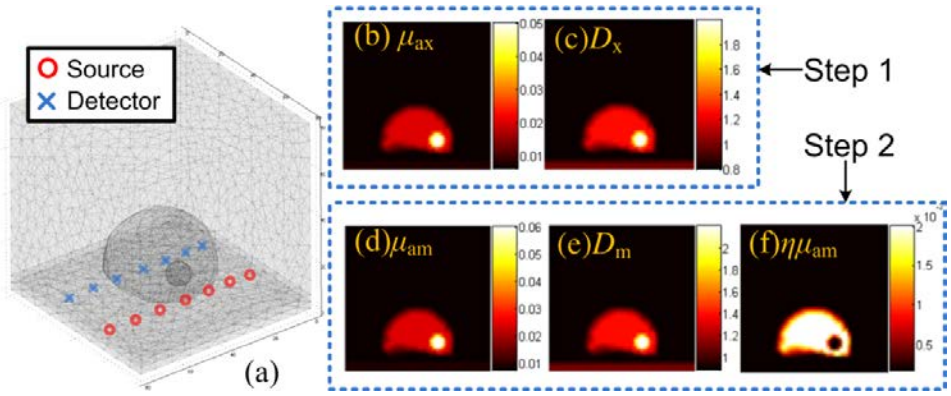

Fig.7.5 Simulation geometry and procedures with region-wise reconstruction algorithm for positive-optical-contrast and negative-fluorescence-yield. (a) Simulation geometry; (b)-(d) μ_{ax} and μ'_{sx} distribution, reconstruction parameters in the step 1; (d)-(f) μ_{am} /μ'_{sm}/$\eta\mu_{af}$ distribution, reconstruction parameters in the step 2.

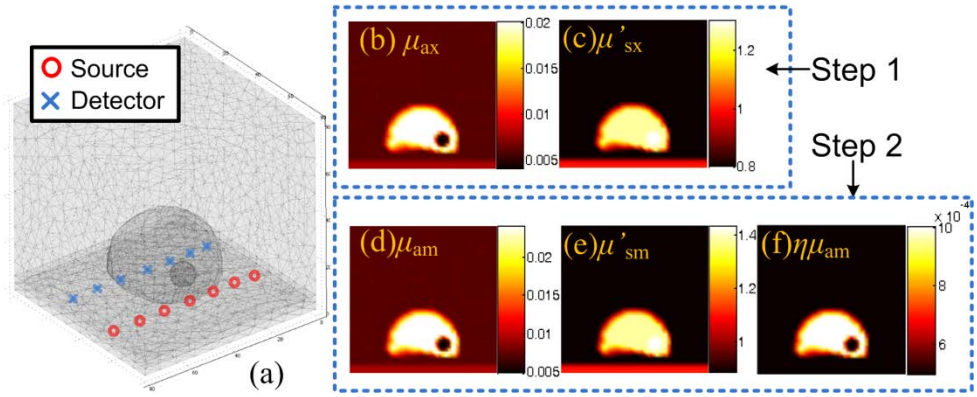

Fig.7.6 Simulation geometry and procedures with region-wise reconstruction algorithm negative-optical-contrast and negative-fluorescence-yield. (a) Simulation geometry; (b)-(d) μ_{ax} and μ'_{sx} distribution, reconstruction parameters in the step 1; (d)-(f) μ_{am} /μ'_{sm}/$\eta\mu_{af}$ distribution, reconstruction parameters in the step 2.

Table 7.1 Comparison between the set values and the reconstruction results given in Fig. 7.5. Note: The optical properties in excitation band is assumed as known, only the unknown parameters in the second step (Fig.7.5 (d)-(f)) are recovered here.

	regions	μ_{am} / mm^{-1}	μ'_{sm} / mm^{-1}	μ_{am} / mm^{-1}	μ'_{sm} / mm^{-1}	μ_{af} / mm^{-1}
Set values	peripheral tissue	0.006	0.8	0.0072	0.88	0.0018
	prostate	0.02	1.25	0.0240	1.375	0.0200
	rectum	0.008	1	0.0096	1.1	0.0018
	tumor	0.05	2.0	0.06	2.2	0.0018
Reconstructed values	peripheral tissue	-	-	0.0070	0.88	0.0018
	prostate	-	-	0.0240	1.444	0.0194
	rectum	-	-	0.0095	1.104	0.0018
	tumor	-	-	0.04	1.465	0.0015

Table 7.2 Comparison between the set values and the reconstruction results given in Fig. 7.6. Note: The optical properties in excitation band is assumed as known, only the unknown parameters in the second step (Fig.7.6 (d)-(f)) are recovered here.

	regions	μ_{am} / mm^{-1}	μ'_{sm} / mm^{-1}	μ_{am} / mm^{-1}	μ'_{sm} / mm^{-1}	μ_{af} / mm^{-1}
Set values	peripheral tissue	0.006	0.8	0.0072	0.88	0.001
	prostate	0.02	1.25	0.0240	1.375	0.002
	rectum	0.008	1	0.0096	1.1	0.001
	tumor	0.004	1.3	0.0048	1.43	0.001
Reconstructed values	peripheral tissue	-	-	0.0072	0.88	0.001
	prostate	-	-	0.0259	1.23	0.0024
	rectum	-	-	0.0094	1.11	0.0010
	tumor	-	-	0.0027	1.22	0.0020

7.3 Design of Experimental validation and preliminary simulation stuides

Immediate future work of this project will be the fabrication of the optical array shown in Fig.7.7 and 7.9(a) and the experimental validation of the simulation results in the previous sections. Instead of using fluorescence materials, the initial investigation of identifying dark inclusions within bright background will utilize phosphorescent materials (specifically Strontium aluminates in this study) for its bright and slow fading emission once excited.

Mixture of intralipid and Strontium aluminates at varied concentrations will be used to simulate the fluorophore uptake in the prostate cancer imaging scenario. Heterogeneities will be

mimicked by glass tubes or cuvettes filled with Strontium aluminates solutions at lower concentrations. Phosphorescent yield contrast between the background and the heterogeneity will vary from 2:1 to infinite in exploration of the imaging sensitivity.

As is shown in Fig.7.7, in the initial examination, ultrasound probe will be placed parallel to the optical array. However, the ultrasound and optical applicator will be combined later, probably as the project aim of the third year. With the spatial *prior* acquired by the ultrasound probe, we will be able to compare sensitivity of region-wise reconstruction and piece-wise reconstruction.

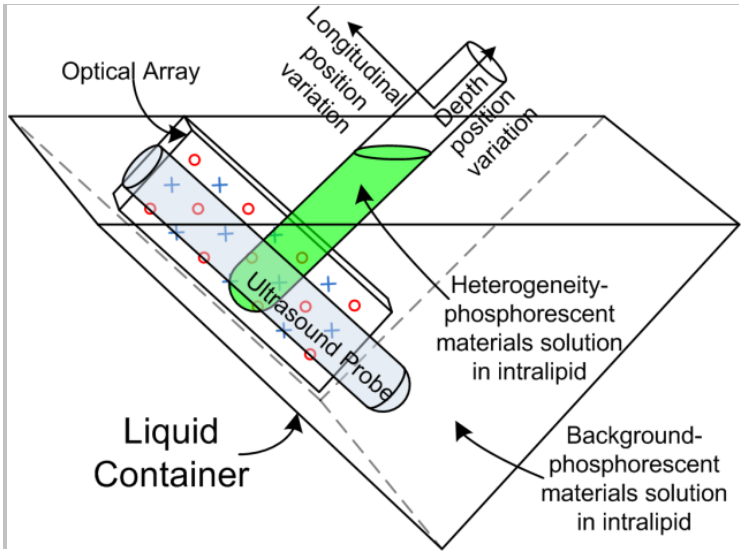

Fig.7.7 Experiment setup for negative fluorophore uptake FDOT

The fluorescence emissions collected by the other 7 detection fibers will be subject to rejection of the excitation light using holographic filter, and passage of the emission light by combined interference and band pass filters, an approach that could reduce the excitation light as much as nine orders of magnitude [143] as is initially shown in Fig.7.6(c). As the filtered emission light could be conveniently focused by a spectrometer for coupling onto a CCD, the filter stack can actually be installed inside the spectrometer. A 16-bit CCD (maximum 48dB dynamic range) with intensifier will have to be used to accommodate the detection of weak fluorescence light originated in the deep tissue, and the large dynamic range associated with the probe dimension. At each fiber switch position, one CCD exposure acquires all corresponding

remission signals, so a complete set of FDOT data is acquired within one complete cycle of fiber-switch or wavelength swept through all source channels.

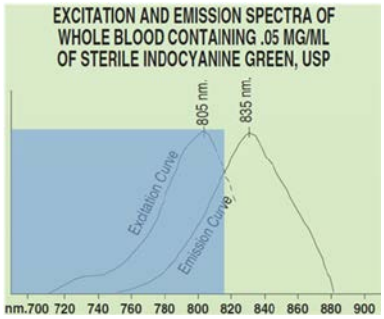

(a)

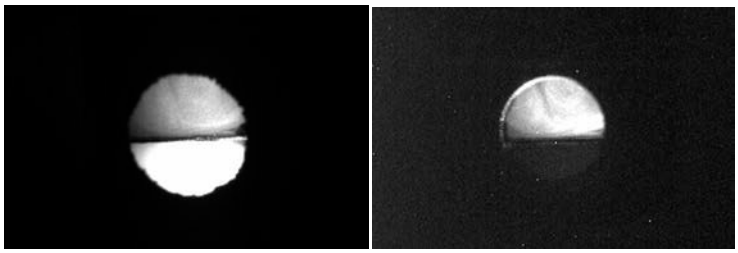

(b) (c)

Fig.7.8 Fluorescence excitation and emission

(a)Excitation and emission spectrum (b) without filter (c) with filter

A few preliminary simulations indicate that the minimum source-detector distance (20mm) of our previous optical array could limit the depth resolution. Therefore, a modified optical array arrangement shown in Fig.7.9(a) will be used in the simulations for future study.

As is shown in Fig.7.9(a), the optical array has eleven sources and ten detectors. The sources and detectors are interspersedly positioned. The minimum source-detector distance in this geometry is thereby 10mm, and the sagittal and lateral extensions of the entire optical array are 60mm and 20mm, respectively.

Simulations include the examinations of the depth and longitudinal sensitivity of the imaging geometries. The FEM mesh includes 6466 nodes and 33591 elements. The background optical properties are assigned as μ_{ax} =0.01, μ'_{sx} =1, μ_{am} =0.012, μ'_{sm} =1.1 and $\eta\mu_{af}$ =10^{-4}. A

7.5mm radius spherical blob is assigned as the heterogeneity. The optical properties of the blob are μ_{ax} =0.02, μ'_{sx} =1.1, μ_{am} =0.264, μ'_{sm} =1.32 and $\eta\mu_{af}$ =10^{-5} (Fluorophore uptake contrast ratio between the background and target is 10:1). In all the following simulations, we assume that the absorption and scattering properties of the targets are accurately determined and only the fluorescence yield is to be recovered.

The first set of simulations compares the target depth localization in image reconstruction with conventional and geometric differential approaches. The target is positioned at the middle of the sagittal plane. The center depth of the target varies from 5mm to 17mm at a step size of 3mm. Fig.7.9(b) shows the reconstruction results with both the conventional method and the GDS method. It can be observed that similar to the endoscopic circular imaging geometry, the GDS method outperforms the conventional method in this planar optical array imaging geometry.

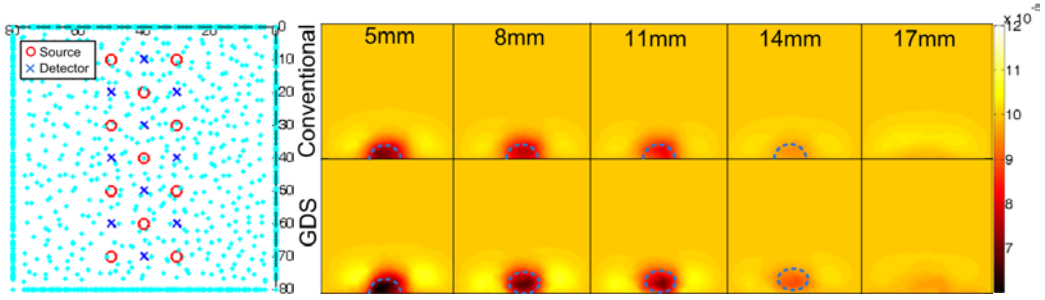

(a) Optical array geometry (b) Simulation results with varied target depth

Fig.7.9 Optical array geometry used in piece-wise simulation study. The numbers at the top of each column in (b) indicated the actual center-to-bottom depths of the targets

The second set of simulations examines the longitudinal target location variation. The target is embedded at the center depth of 14mm and moved along the sagittal middle plane from 15mm to 40mm from the left boundary of the imaging domain at a step size of 5mm. The reconstruction results are shown in Fig.7.10.

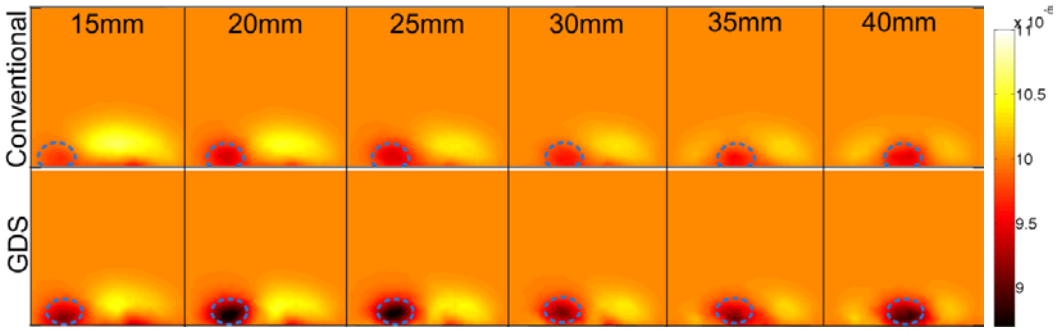

Fig.7.10 Piece-wise simulation results with varied target longitudinal position variation in sagittal-middle plane of the imaging geometry.

Two features can be observed in Fig.7.10: 1) GDS method better recovers the fluorescence yield contrast; 2) the target depth localization is better resolved by the GDS method.

7.4 Summary

Simulation studies has preliminary validated the feasibility of imaging reverse uptake of fluorophore within the trans-rectal prostate imaging geometry. Geometry differential reconstruction methods and adaptive mesh has been implemented to piece-wise reconstruction for accurate target depth localization. The simulation studies also show that region-wise reconstruction can actually facilitate the simultaneous reconstruction of the emission band optical properties and fluorophore uptake, simplifying the measurement procedures. Experiment setup along with a new optical array has been designed. Optical filters will be integrated to the wavelength swept source based imaging system presented in the previous chapter. Liquid phantom containing phosphorence emitting material will be temporarily for the principle validations of the imaging system.

CHAPTER VIII

CONCLUSIONS AND FUTURE WORKS

8.1 Contribution of this work

Improvement in both computational modeling and instrumentation aspects of DOT have been investigated in this study.

An innovative hierarchical reconstruction algorithm for DOT combining the TRUS spatial prior is developed. Simulation and experiments demonstrated that the method is capable of accurately recovery the optical properties within an imaging volume with multiple substructures. The reconstruction algorithm is subsequently implemented to our TRUS-DOT combined trans-rectal prostate imaging geometry for the preliminary evaluation of the system performance. The algorithm is extended to FDOT and validated by simulation studies.

The utilization of a hierarchical spatial *prior* is under the condition that the anatomic information of the prostate tumor is explicit from TRUS. The prostate boundary is well-delineated in TRUS, and the spatial extent of a tumor can be defined if it is shown as hypo-echoic on TRUS. This is when the NIR functional contrast can help determine whether a tissue suspicious on US is malignant or not [45]. However, since as many as 40% of the tumors may be shown as iso-echoic on TRUS, the utility or accuracy of this hierarchical imaging approach is hindered when TRUS images do not specify a suspicious region, or when it is difficult to define

the spatial extent of a suspicion region in TRUS. Under these circumstances, the third step of recovering the tumor lesion in the prostate may proceed by reconstructing the optical properties on every element within the prostate instead of treating the prostate as homogenous other than an inclusion that is also treated as homogenous in the simulation. Such approach is proven effective based on our other investigations, but the accuracy and robustness may be affected by the depth-dependent sensitivity. More dedicated investigations are needed in the future along with the experimental validations of this combined trans-rectal NIR/US approach. Prostate trans-rectal optical imaging is a relatively new area where the initial approach should focus on characterizing the lesions most suspicious to TRUS. Trans-rectal NIR imaging of the lesions marginally suspicious to TRUS or non-suspicious to TRUS is apparently more challenging and should be preceded by trans-rectal NIR/US characterization of a lesion suspicious to US.

A novel arametric recovery uncertainty level (PRUL) models are derived for both single and multiple wavelength DOT system. Analytical analysis on the models provide direct evidence that DC-based reconstruction is much less-accurate in recovering the absolute optical properties of target-of-interest when no additional spatial information is available to confine the reconstruction, as having been universally recognized by the DOT community. However, apart from these well-expected shortcomings, it seems that DC-based reconstruction may not be completely unfavorable. This study generalized the analytical approach initially proposed in [78] to quantify the level of image artifacts that is expressed by the standard deviation of a parameter over the parameter itself. Parameters representative of tissue measurements are used to evaluate the analytic results and conduct the synthetic studies, in both of which the DC reconstruction produced lower level of relative variation in the optical parameters recovered, and some advantages in the CNR. It may be argued that DC flattens images, leading to a lower standard deviation in the background, and because the background standard deviation is the denominator of CNR, the CNR of DC could become better. But if there were flattening of the image, then the numerator of CNR would also be flattened, and perhaps flattened more strongly owing to the non-

linearity of DOT thereby under-estimated at a higher level, that collectively might reduce the CNR rather than increase the CNR. The slight but notable CNR advantage of DC over FD-based reconstruction demonstrated in this study strongly suggest some inherent advantages of DC, but on the other hand, it could be just because DC has lower information content, similar to what one could expect by reducing the amount of data available or increasing the regularization in FD-based reconstructions.

The PRUL model has also been applied to multispectral optical tomography and used to evaluate the sets of wavelength for spectrally-constrained optical tomography reconstruction. The analytical predictions are generally supported by simulations. In imaging geometries where reliable sensitivity distribution is available, DC-only reconstruction outperforms FD reconstruction. The advantage of the extra phase information in FD measurement becomes prominent under significantly non-uniform spatial sensitivity distribution. It is also found that including DC component in FD reconstruction improves the overall reconstruction results in multi-spectral optical tomography, which is similar to that demonstrated in single-wavelength NIR tomography reconstruction.

A novel wavelength-swept light source based DOT for rapid data acquisition is constructed. Source channel encoding and sequential source light delivery are achieved by the utilization of a NI DAQ card and LabView codes.

With the 4mW source power and 170ms exposure time, the system can detect targets with center depth up to 20mm. Although the previously reported broad-band spectral encoding system possesses higher total power level (20mW), the average power coupled to each source channel could be on the same level as or even lower than the system constructed in this study. The 0.5 frame per second data requisition rate could be dramatically raised by increasing the source power and but the source-by-source exposure pattern will become the ultimate upper limit

to the frame rate. Further investigations will be conducted to explore the trade-off point between the broadband and swept source systems.

Temporal encoding of the novel system schematics can potentially extend the number of sources channel for a system with predetermined imaging sensor dimension. For the 12.5mm×12.5mm sensor dimension utilized in this study, only 7 source channels with spectrally discernable displacement can be covered simultaneously. However, temporal encoding of the source light enables independent signal detection (Fig.5.9(a)) even though the source channels spectrally overlap (Fig.5.5(b)). Therefore, with rapid, temporally encoded wavelength swept, the identical system can acquire light signals from 14 channels (or more by using low grooves per mm gratings) in a short time expansion. Such feature is especially beneficial for imaging scenarios with numerous source locations but require high signal acquisition frequency, for instance brain functional imaging[111], as is previously mentioned.

Calibration with analytical model is proved to be effective and accurate in the circular geometries, although fitting experimental data to the approximately evaluated model could be computationally intensive and impracticable with the gradient based algorithms. The more exhaustive heuristic random optimization approach [125] is implemented in two stages to the calibration process, which is validated by the experimental results. However, the analytical model utilized in this study cannot solve phase shift of light propagation in a cylindrical geometry, and the continuous wave measurement system also induces the less accurate scattering part calibration. It is expected that with frequency domain measurements and appropriate models, system calibration reliability can be improved, which contributes to more accurate estimation of the absolute optical property values.

Prospectively, the system structure can also substantially increase the data acquisition rate of fluorescence optical tomography [126-128]. Although simultaneous excitation of the fluorophor is achievable in multiple laser diodes and broadband spectral encoding systems, varied excitation wavelengths produces the same emission spectrum except the difference in

fluorescence yield ratio, which is infeasible to separate by the CCD-spectrometer system at the detection end. Therefore, spectral encoding in optical tomography alone does not work in fluorescence tomography cases, and the prominent superiority in data acquisition rate of the novel temporal-spectral encoding combined system over the mechanical switching indicates the potentially implementation of such system structure in the immediate future work of this study.

Reconstruction algorithm based on geometric differential sensitivity profile is derived under the method of surrogate objective function. The method minimizes the spatial sensitivity variation within the reflectance imaging geometries and improves target depth localization accuracy. The method can be implemented to both multispectral and fluorescence enhanced DOT.

The advantage of GDS approach over reconstruction based on conventional sensitivity profile was demonstrated by simulations and phantom studies of localizing and resolving one or two sharp-contrast targets. The better suppression of artifacts by the GDS approach is also likely related to the cancellation of common uncertainty factors in measurements, similar to that demonstrated in a spectral-derivative algorithm [132].

Because of the structural similarity of the sensitivity matrix, this algorithm could also be extended to fluorescence-enhanced diffuse optical tomography in geometries suffering significant depth-degrading sensitivity. The transformation of the conventional sensitivity matrix to the GDS approach, however, is accompanied by an increase in the element number in the objective function due to the increase of the number of row vectors in sensitivity matrix from $m \times n$ to $m \times n \times (n-1)/2$. It is found in this study that the total computation time of executing the GDS method is approximately 40% more than using the conventional method.

A preliminary FDOT experiment system is designed. Simulation results indicated that region-wise reconstruction in FDOT may recover the optical properties in the emission band and the fluorophore uptake simultaneously, simplifying the measurement procedure of FDOT. Piece-wise reconstruction also indicate that the negative fluorophore uptake can be recovered within the reflectance imaging geometry.

8.2 Future works

For the computation modeling aspect, the PRUL model will be extended to the analysis of spectral differential DOT reconstruction algorithms[132]. Spectral differential reconstruction has shown prominent advantage in noise and system error reduction in multispectral DOT reconstruction. The implementation of PRUL to image reconstruction of DOT can derive critical information such as the effect of integrating phase information in the reconstruction, wavelength selection optimization and differential wavelength interval optimization.

For experimental and instrumentation, the feasibility of imaging reverse fluorophore uptake will be investigate by phantom studies and in vivo experiments. Phosphorescent materials will be preliminarily used for its bright emission and longer life time. Varied uptake ratios will be examined to reveal the sensitivity of FDOT to such imaging scenario. The zinc-specific fluorescence emitting material will be ultimately investigated *in vivo* in validation of our proposed idea of early diagnosis of prostate cancer with such metabolic biomarkers.

REFERENCES

[1] Jacques, S.L. and B.W. Pogue, Tutorial on diffuse light transport. Journal of Biomedical Optics, 2008. 13(4): p. 041302-19.

[2] Li, C., et al., Using a priori structural information from magnetic resonance imaging to investigate the feasibility of prostate diffuse optical tomography and spectroscopy: A simulation study. Medical Physics, 2007. 34(1): p. 266-274.

[3] Brooksby, B.A., et al., Near-infrared (NIR) tomography breast image reconstruction with a priori structural information from MRI: algorithm development for reconstructing heterogeneities. Selected Topics in Quantum Electronics, IEEE Journal of, 2003. 9(2): p. 199-209.

[4] Huang, M., Three dimensional near-infrared optical imaging using ultrasound guidance for breast cancer detection and diagnosis. PhD Dissertation, 2005.

[5] Jiang, Z., et al., Trans-rectal ultrasound-coupled near-infrared optical tomography of the prostate, Part II: Experimental demonstration. Opt. Express, 2008. 16(22): p. 17505-17520.

[6] Niu, H., et al., Development of a compensation algorithm for accurate depth localization in diffuse optical tomography. Opt. Lett., 2010. 35(3): p. 429-431.

[7] Corlu, A., et al., Diffuse optical tomography with spectral constraints and wavelength optimization. Appl. Opt., 2005. 44(11): p. 2082-2093.

[8] Pogue, B.W., et al., Spatially Variant Regularization Improves Diffuse Optical Tomography. Appl. Opt., 1999. 38(13): p. 2950-2961.

[9] Tian, F., G. Alexandrakis, and H. Liu, Optimization of probe geometry for diffuse optical brain imaging based on measurement density and distribution. Appl. Opt., 2009. 48(13): p. 2496-2504.

[10] Huang, M. and Q. Zhu, Dual-Mesh Optical Tomography Reconstruction Method with a Depth Correction that Uses A Priori Ultrasound Information. Appl. Opt., 2004. 43(8): p. 1654-1662.

[11] Xu, G., et al., Trans-rectal ultrasound-coupled near-infrared optical tomography of the prostate, Part I: Simulation. Opt. Express, 2008. 16(22): p. 17484-17504.

[12] Jiang, Z., et al., Trans-rectal Ultrasound-coupled Spectral Optical Tomography of Total Hemoglobin Concentration Enhances Assessment of the Laterality and Progression of a Transmissible Venereal Tumor in Canine Prostate. Urology, 201177(1): 237-242.

[13] Huang, M., et al., Simultaneous Reconstruction of Absorption and Scattering Maps with Ultrasound Localization: Feasibility Study Using Transmission Geometry. Appl. Opt., 2003. 42(19): p. 4102-4114.
[14] Piao, D. and B.W. Pogue, Rapid near-infrared diffuse tomography for hemodynamic imaging using a low-coherence wideband light source. Journal of Biomedical Optics, 2007. 12(1): p. 014016-12.
[15] Anuradha, G. and et al., Fluorescence-enhanced optical imaging in large tissue volumes using a gain-modulated ICCD camera. Physics in Medicine and Biology, 2003. 48(12): p. 1701.
[16] Jemal, A., et al., Cancer Statistics, 2007. CA: A Cancer Journal for Clinicians, 2007. 57(1): p. 43-66.
[17] Polascik, T.J., J.E. Oesterling, and A.W. Partin, Prostate specific antigen: a decade of discovery-what we have learned and where we are going. The Journal of Urology, 1999. 162(2): p. 293-306.
[18] Grossfeld, G.D. and P.R. Carroll, Prostate Cancer Early Detection: a Clinical Perspective. Epidemiologic Reviews, 2001. 23(1): p. 173-180.
[19] Stamey, T.A., et al., The Prostate specific antigen era in the United States is over for prostate cancer: what happened in the last 20 years? The Journal of Urology, 2004. 172(4, Part 1): p. 1297-1301.
[20] Pound, C.R., et al., Natural History of Progression After PSA Elevation Following Radical Prostatectomy. JAMA, 1999. 281(17): p. 1591-1597.
[21] Loch, A., et al., Technical and anatomical essentials for transrectal ultrasound of the prostate. World Journal of Urology, 2007. 25(4): p. 361-366.
[22] Bill-Axelson, A., et al., Radical Prostatectomy versus Watchful Waiting in Early Prostate Cancer. New England Journal of Medicine, 2005. 352(19): p. 1977-1984.
[23] Spajic, B., et al., The Incidence of Hyperechoic Prostate Cancer in Transrectal Ultrasound-Guided Biopsy Specimens. Urology, 2007. 70(4): p. 734-737.
[24] Shinohara, K., T. Wheeler, and P. Scardino, The appearance of prostate cancer on transrectal ultrasonography: correlation of imaging and pathological examinations. J Urol, 1989. 142(1): p. 7.
[25] Porter, C.R., Does the number of prostate biopsies performed affect the nature of the cancer identified? Nat Clin Pract Urol, 2007. 4(3): p. 132-133.
[26] Scattoni, V., et al., Extended and Saturation Prostatic Biopsy in the Diagnosis and Characterisation of Prostate Cancer: A Critical Analysis of the Literature. European Urology, 2007. 52(5): p. 1309-1322.
[27] Tromberg, B.J., et al., Non–invasive measurements of breast tissue optical properties using frequency–domain photon migration. Philosophical Transactions of the Royal Society of London. Series B: Biological Sciences, 1997. 352(1354): p. 661-668.
[28] Pogue, B.W., et al., Quantitative Hemoglobin Tomography with Diffuse Near-Infrared Spectroscopy: Pilot Results in the Breast1. Radiology, 2001. 218(1): p. 261-266.
[29] Ntziachristos, V. and B. Chance, Breast imaging technology: Probing physiology and molecular function using optical imaging - applications to breast cancer. Breast Cancer Res, 2001. 3(1): p. 41 - 46.
[30] Choe, R., et al., Diffuse optical tomography of breast cancer during neoadjuvant

chemotherapy: A case study with comparison to MRI. Medical Physics, 2005. 32(4): p. 1128-1139.
[31] Franceschini, M.A., et al., Frequency-domain techniques enhance optical mammography: Initial clinical results. Proceedings of the National Academy of Sciences of the United States of America, 1997. 94(12): p. 6468-6473.
[32] Zhu, Q., et al., Benign versus Malignant Breast Masses: Optical Differentiation with US-guided Optical Imaging Reconstruction1. Radiology, 2005. 237(1): p. 57-66.
[33] Bigler, S.A., R.E. Deering, and M.K. Brawer, Comparison of microscopic vascularity in benign and malignant prostate tissue. Human Pathology, 1993. 24(2): p. 220-226.
[34] Ali, J.H., et al., Near infrared spectroscopy and imaging to probe differences in water content in normal and cancer human prostate tissues. Cancer Res. Treat., 2004. 3: p. 7.
[35] Arnfield, M.R., et al., OPTICAL PROPERTIES OF EXPERIMENTAL PROSTATE TUMORS in vivo. Photochemistry and Photobiology, 1993. 57(2): p. 306-311.
[36] Zhu, T.C., et al., Optical Properties of Human Prostate at 732 nm Measured In Vivo During Motexafin Lutetium–mediated Photodynamic Therapy¶. Photochemistry and Photobiology, 2005. 81(1): p. 96-105.
[37] Svensson, T., et al., In vivo optical characterization of human prostate tissue using near-infrared time-resolved spectroscopy. Journal of Biomedical Optics, 2007. 12(1): p. 014022-10.
[38] Manan, G., et al. Application of Near Infrared Multi-Spectral CCD Imager System to Determine the Hemodynamic Changes in Prostate Tumor. 2006: Optical Society of America.
[39] Liu, H., et al., Noninvasive Investigation of Blood Oxygenation Dynamics of Tumors by Near-Infrared Spectroscopy. Appl. Opt., 2000. 39(28): p. 5231-5243.
[40] Jacques, S.L. and M. Motamedi. Tomographic needles and catheters for optical imaging of prostatic cancer. 1995. San Jose, CA, USA: SPIE.
[41] Musgrove, C., et al. Computational aspects of endoscopic (trans-rectal) near-infrared optical tomography: initial investigations. 2007. San Jose, CA, USA: SPIE.
[42] Piao, D., et al. Near-infrared optical tomography: endoscopic imaging approach. 2007. San Jose, CA, USA: SPIE.
[43] Dehghani, H., et al. Structural a priori information in near-infrared optical tomography. 2007: SPIE.
[44] Zhu, Q., et al., Imager that combines near-infrared diffusive light and ultrasound. Opt. Lett., 1999. 24(15): p. 1050-1052.
[45] Holboke, M.J., et al., Three-dimensional diffuse optical mammography with ultrasound localization in a human subject. Journal of Biomedical Optics, 2000. 5(2): p. 237-247.
[46] Pogue, B.W., et al., Three-Dimensional Simulation of Near-Infrared Diffusion in Tissue: Boundary Condition and Geometry Analysis for Finite-Element Image Reconstruction. Appl. Opt., 2001. 40(4): p. 588-600.
[47] Schweiger, M., S.R. Arridge, and D.T. Delpy, Application of the finite-element

method for the forward and inverse models in optical tomography. Journal of Mathematical Imaging and Vision, 1993. 3(3): p. 263-283.
[48] Xiao-Hu, Y., C. Guo-An, and C. Shi-Xin, Dynamic learning rate optimization of the backpropagation algorithm. Neural Networks, IEEE Transactions on, 1995. 6(3): p. 669-677.
[49] Schweiger, M., et al., Reconstructing absorption and diffusion shape profiles in optical tomography by a level set technique. Opt. Lett., 2006. 31(4): p. 471-473.
[50] Kolehmainen, V. and et al., Recovery of region boundaries of piecewise constant coefficients of an elliptic PDE from boundary data. Inverse Problems, 1999. 15(5): p. 1375.
[51] Kolehmainen, V., et al., Recovery of piecewise constant coefficients in optical diffusion tomography. Opt. Express, 2000. 7(13): p. 468-480.
[52] Kolehmainen, V. and et al., Simultaneous reconstruction of internal tissue region boundaries and coefficients in optical diffusion tomography. Physics in Medicine and Biology, 2000. 45(11): p. 3267.
[53] Srinivasan, S., et al., Improved quantification of small objects in near-infrared diffuse optical tomography. Journal of Biomedical Optics, 2004. 9(6): p. 1161-1171.
[54] Yalavarthy, P.K., et al., Critical computational aspects of near infrared circular tomographic imaging: Analysis of measurement number, mesh resolution and reconstruction basis. Opt. Express, 2006. 14(13): p. 6113-6127.
[55] Wise, A.M., et al., Morphologic and clinical significance of multifocal prostate cancers in radical prostatectomy specimens. Urology, 2002. 60(2): p. 264-269.
[56] Miller, G. and J. Cygan, Morphology of prostate cancer: the effects of multifocality on histological grade, tumor volume and capsule penetration. J Urol, 1994. 152(5.2): p. 2.
[57] Arridge, S.R., Optical tomography in medical imaging. Inverse Problems, 1999. 15(2): p. R41.
[58] Feng, G. and et al., Optical tomographic mapping of cerebral haemodynamics by means of time-domain detection: methodology and phantom validation. Physics in Medicine and Biology, 2004. 49(6): p. 1055.
[59] Rinneberg, H., et al., Scanning time-domain optical mammography: detection and characterization of breast tumors in vivo. Technol. Cancer Res. Treat., 2005. 4: p. 4.
[60] Tanifuji, T. and M. Hijikata, Finite difference time domain (FDTD) analysis of optical pulse responses in biological tissues for spectroscopic diffused optical tomography. Medical Imaging, IEEE Transactions on, 2002. 21(2): p. 181-184.
[61] Mo, W. and N. Chen, Fast time-domain diffuse optical tomography using pseudorandom bit sequences. Opt. Express, 2008. 16(18): p. 13643-13650.
[62] Pogue, B.W. and et al., Initial assessment of a simple system for frequency domain diffuse optical tomography. Physics in Medicine and Biology, 1995. 40(10): p. 1709.
[63] Wang, J., et al., Broadband frequency-domain near-infrared spectral tomography using a mode-locked Ti:sapphire laser. Appl. Opt., 2009. 48(10): p. D198-D207.
[64] Hueber, D.M. and et al., Non-invasive and quantitative near-infrared haemoglobin spectrometry in the piglet brain during hypoxic stress, using a frequency-domain

multidistance instrument. Physics in Medicine and Biology, 2001. 46(1): p. 41.
[65] Chen, N.G., et al., Portable near-infrared diffusive light imager for breast cancer detection. Journal of Biomedical Optics, 2004. 9(3): p. 504-510.
[66] Tromberg, B.J., et al., Assessing the future of diffuse optical imaging technologies for breast cancer management. Medical Physics, 2008. 35(6): p. 2443-2451.
[67] Gulsen, G., et al., Combined diffuse optical tomography (DOT) and MRI system for cancer imaging in small animals. Technol. Cancer Res. Treat., 2006. 5: p. 3.
[68] Papazoglou, E.S., et al., Near Infrared Diffuse Optical Tomography: Improving the Quality of Care in Chronic Wounds of Patients With Diabetes. Biomedical Instrumentation & Technology, 2007. 41(1): p. 83-87.
[69] Culver, J.P., et al., Three-dimensional diffuse optical tomography in the parallel plane transmission geometry: Evaluation of a hybrid frequency domain/continuous wave clinical system for breast imaging. Medical Physics, 2003. 30(2): p. 235-247.
[70] Kim, H.K., et al., Optimal source-modulation frequencies for transport-theory-based optical tomography of small-tissue volumes. Opt. Express, 2008. 16(22): p. 18082-18101.
[71] Iftimia, N. and H. Jiang, Quantitative Optical Image Reconstruction of Turbid Media by Use of Direct-Current Measurements. Appl. Opt., 2000. 39(28): p. 5256-5261.
[72] Siegel, A., J.J. Marota, and D. Boas, Design and evaluation of a continuous-wavediffuse optical tomography system. Opt. Express, 1999. 4(8): p. 287-298.
[73] Xu, Y., et al., Absorption and Scattering Images of Heterogeneous Scattering Media Can Be Simultaneously Reconstructed by Use of dc Data. Appl. Opt., 2002. 41(25): p. 5427-5437.
[74] Yuan, Z. and H. Jiang, Image reconstruction scheme that combines modified Newton method and efficient initial guess estimation for optical tomography of finger joints. Appl. Opt., 2007. 46(14): p. 2757-2768.
[75] Huabei, J. and et al., Improved continuous light diffusion imaging in single- and multi-target tissue-like phantoms. Physics in Medicine and Biology, 1998. 43(3): p. 675.
[76] Pei, Y., H. Graber, and R. Barbour, Normalized-constraint algorithm for minimizing inter-parameter crosstalk in DC optical tomography. Opt. Express, 2001. 9(2): p. 97-109.
[77] Andreas, H.H. and et al., Sagittal laser optical tomography for imaging of rheumatoid finger joints. Physics in Medicine and Biology, 2004. 49(7): p. 1147.
[78] Wang, K.K.-H. and T.C. Zhu, Reconstruction of in-vivo optical properties for human prostate using interstitial diffuse optical tomography. Opt. Express, 2009. 17(14): p. 11665-11672.
[79] Schweiger, M., et al., Image reconstruction in optical tomography in the presence of coupling errors. Appl. Opt., 2007. 46(14): p. 2743-2756.
[80] Ntziachristos, V., et al., Diffuse optical tomography of highly heterogeneous media. Medical Imaging, IEEE Transactions on, 2001. 20(6): p. 470-478.
[81] Fantini, S., et al., Quantitative determination of the absorption spectra of chromophores in strongly scattering media: a light-emitting-diode based

technique. Appl. Opt., 1994. 33(22): p. 5204-5213.
[82] Boas, D., T. Gaudette, and S. Arridge, Simultaneous imaging and optode calibration with diffuse optical tomography. Opt. Express, 2001. 8(5): p. 263-270.
[83] Jacques, S.L., Reflectance spectroscopy with optical fiber devices and transcutaneous bilirubinometers. Biomedical Optical Instrumentation and Laser-Assisted Biotechnology, 1996: p. 12.
[84] Fabbri, F., M.A. Franceschini, and S. Fantini, Characterization of Spatial and Temporal Variations in the Optical Properties of Tissuelike Media with Diffuse Reflectance Imaging. Appl. Opt., 2003. 42(16): p. 3063-3072.
[85] Dehghani, H., et al., Three-Dimensional Optical Tomography: Resolution in Small-Object Imaging. Appl. Opt., 2003. 42(16): p. 3117-3128.
[86] Dehghani, H., et al., Near infrared optical tomography using NIRFAST: Algorithm for numerical model and image reconstruction. Communications in Numerical Methods in Engineering, 2009. 25(6): p. 711-732.
[87] Arridge, S.R. and W.R.B. Lionheart, Nonuniqueness in diffusion-based optical tomography. Opt. Lett., 1998. 23(11): p. 882-884.
[88] Bastian, H., On uniqueness in diffuse optical tomography. Inverse Problems, 2009. 25(5): p. 055010.
[89] Jiang, Z., et al., In vivo trans-rectal ultrasound--coupled optical tomography of a transmissible venereal tumor model in the canine pelvic canal. Journal of Biomedical Optics, 2009. 14(3): p. 030506-3.
[90] Corlu, A., et al., Uniqueness and wavelength optimization in continuous-wave multispectral diffuse optical tomography. Opt. Lett., 2003. 28(23): p. 2339-2341.
[91] Srinivasan, S., et al., Spectrally constrained chromophore and scattering near-infrared tomography provides quantitative and robust reconstruction. Appl. Opt., 2005. 44(10): p. 1858-1869.
[92] Li, A., et al., Reconstructing chromosphere concentration images directly by continuous-wave diffuse optical tomography. Opt. Lett., 2004. 29(3): p. 256-258.
[93] Jobsis, F.F., Noninvasive, infrared monitoring of cerebral and myocardial oxygen sufficiency and circulatory parameters. Science, 1977. 198(4323): p. 1264-1267.
[94] McBride, T.O., et al., Multispectral near-infrared tomography: a case study in compensating for water and lipid content in hemoglobin imaging of the breast. Journal of Biomedical Optics, 2002. 7(1): p. 72-79.
[95] Jiang, Z., et al., Trans-rectal Ultrasound-coupled Spectral Optical Tomography of Total Hemoglobin Concentration Enhances Assessment of the Laterality and Progression of a Transmissible Venereal Tumor in Canine Prostate. Urology, 2011. 77(1): p. 237-242.
[96] Jones, P.B., et al., Simultaneous multispectral reflectance imaging and laser speckle flowmetry of cerebral blood flow and oxygen metabolism in focal cerebral ischemia. Journal of Biomedical Optics, 2008. 13(4): p. 044007.
[97] Xu, H., et al., Magnetic-resonance-imaging-coupled broadband near-infrared tomography system for small animal brain studies. Appl. Opt., 2005. 44(11): p. 2177-2188.
[98] Brooksby, B., et al., Spectral priors improve near-infrared diffuse tomography more than spatial priors. Opt. Lett., 2005. 30(15): p. 1968-1970.
[99] Wang, J., et al., Spectral tomography with diffuse near-infrared light: inclusion of

broadband frequency domain spectral data. Journal of Biomedical Optics, 2008. 13(4): p. 041305-10.
[100] Wang, J., et al., Near-infrared tomography of breast cancer hemoglobin, water, lipid, and scattering using combined frequency domain and cw measurement. Opt. Lett., 2010. 35(1): p. 82-84.
[101] Wang, J., et al., In vivo quantitative imaging of normal and cancerous breast tissue using broadband diffuse optical tomography. Medical Physics, 2010. 37(7): p. 3715-3724.
[102] Xu, G., et al., Direct-current-based image reconstruction versus direct-current included or excluded frequency-domain reconstruction in diffuse optical tomography. Appl. Opt., 2010. 49(16): p. 3059-3070.
[103] Eames, M.E., et al., Wavelength band optimization in spectral near-infrared optical tomography improves accuracy while reducing data acquisition and computational burden. Journal of Biomedical Optics, 2008. 13(5): p. 054037-9.
[104] Li, C., et al., Multispectral diffuse optical tomography with absorption and scattering spectral constraints. Appl. Opt., 2007. 46(34): p. 8229-8236.
[105] Eames, M.E. and H. Dehghani, Wavelength dependence of sensitivity in spectral diffuse optical imaging: effect of normalization on image reconstruction. Opt. Express, 2008. 16(22): p. 17780-17791.
[106] Prahl, S.A., Optical absorption of hemoglobin. 1999: p. http://omlc.ogi.edu/spectra/hemoglobin/.
[107] Pogue, B., et al., Instrumentation and design of a frequency-domaindiffuse optical tomography imager for breast cancer detection. Opt. Express, 1997. 1(13): p. 391-403.
[108] Zhang, Q., et al., Coregistered tomographic x-ray and optical breast imaging: initial results. Journal of Biomedical Optics, 2005. 10(2): p. 024033-9.
[109] Chengyu Li, R.L., Rex Cheung ,Haesun Choi Using a priori structural information from magnetic resonance imaging to investigate the feasibility of prostate diffuse optical tomography and spectroscopy: A simulation study. Medical Physics, 2007. 34(1): p. 9.
[110] Yuan, Z., et al., Tomographic x-ray--guided three-dimensional diffuse optical tomography of osteoarthritis in the finger joints. Journal of Biomedical Optics, 2008. 13(4): p. 044006-10.
[111] Boas, D.A. and A.M. Dale, Simulation study of magnetic resonance imaging-guided cortically constrained diffuse optical tomography of human brain function. Appl. Opt., 2005. 44(10): p. 1957-1968.
[112] Dehghani, H., et al., Depth sensitivity and image reconstruction analysis of dense imaging arrays for mapping brain function with diffuse optical tomography. Appl. Opt., 2009. 48(10): p. D137-D143.
[113] Strangman, G., et al., A Quantitative Comparison of Simultaneous BOLD fMRI and NIRS Recordings during Functional Brain Activation. NeuroImage, 2002. 17(2): p. 719-731.
[114] Pogue, B.W. and K.D. Paulsen, High-resolution near-infrared tomographic imaging simulations of the rat cranium by use of a priori magnetic resonance imaging structural information. Opt. Lett., 1998. 23(21): p. 1716-1718.
[115] Hielscher, A.H., Optical tomographic imaging of small animals. Current Opinion

in Biotechnology, 2005. 16(1): p. 79-88.
[116] Schmitz, C.H., et al., Dynamic studies of small animals with a four-color diffuse optical tomography imager. Review of Scientific Instruments, 2005. 76(9): p. 094302.
[117] Schmitz, C.H., et al., Instrumentation for fast functional optical tomography. Review of Scientific Instruments, 2002. 73(2): p. 429.
[118] Piao, D., et al., Video-rate near-infrared optical tomography using spectrally encoded parallel light delivery. Opt. Lett., 2005. 30(19): p. 2593-2595.
[119] Li, Z., et al., Video-rate near infrared tomography to image pulsatile absorption properties in thick tissue. Opt. Express, 2009. 17(14): p. 12043-12056.
[120] Choma, M., et al., Sensitivity advantage of swept source and Fourier domain optical coherence tomography. Opt. Express, 2003. 11(18): p. 2183-2189.
[121] Huber, R., et al., Three-dimensional and C-mode OCT imaging with a compact, frequency swept laser source at 1300 nm. Opt. Express, 2005. 13(26): p. 10523-10538.
[122] Yasuno, Y., et al., Three-dimensional and high-speed swept-source optical coherence tomography for in vivo investigation of human anterior eye segments. Opt. Express, 2005. 13(26): p. 10652-10664.
[123] Strupler, M., et al., Rapid spectrally encoded fluorescence imaging using a wavelength-swept source. Opt. Lett., 2010. 35(11): p. 1737-1739.
[124] Zhang, A., et al., Photon diffusion in a homogeneous medium bounded externally or internally by an infinitely long circular cylindrical applicator. I. Steady-state theory. J. Opt. Soc. Am. A, 2010. 27(3): p. 648-662.
[125] Li, J. and R. Russell Rhinehart, Heuristic random optimization. Computers & Chemical Engineering, 1998. 22(3): p. 427-444.
[126] Davis, S.C., et al., Image-guided diffuse optical fluorescence tomography implemented with Laplacian-type regularization. Opt. Express, 2007. 15(7): p. 4066-4082.
[127] Yuan, B. and Q. Zhu, Separately reconstructing the structural and functional parameters of a fluorescent inclusion embedded in a turbid medium. Opt. Express, 2006. 14(16): p. 7172-7187.
[128] Lee, J. and E.M. Sevick-Muraca, Three-dimensional fluorescence enhanced optical tomography using referenced frequency-domain photon migration measurements at emission and excitation wavelengths. J. Opt. Soc. Am. A, 2002. 19(4): p. 759-771.
[129] Culver, J.P., et al., Volumetric diffuse optical tomography of brain activity. Opt. Lett., 2003. 28(21): p. 2061-2063.
[130] Zhao, Q., L. Ji, and T. Jiang, Improving depth resolution of diffuse optical tomography with a layer-based sigmoid adjustment method. Opt. Express, 2007. 15(7): p. 4018-4029.
[131] Lange, K., D.R. Hunter, and Y. Ilsoon, Optimization Transfer Using Surrogate Objective Functions. Journal of Computational and Graphical Statistics, 2000. 9(1): p. 1-20.
[132] Xu, H., et al., Spectral derivative based image reconstruction provides inherent insensitivity to coupling and geometric errors. Opt. Lett., 2005. 30(21): p. 2912-2914.

[133] Frederickson, C.J., J.-Y. Koh, and A.I. Bush, The neurobiology of zinc in health and disease. Nat Rev Neurosci, 2005. 6(6): p. 449-462.
[134] Giblin, L.J., et al., Zinc-secreting Paneth Cells Studied by ZP Fluorescence. J. Histochem. Cytochem., 2006. 54(3): p. 311-316.
[135] Frederickson, C., J. Perez-Clausell, and G. Danscher, Zinc-containing 7S-NGF complex. Evidence from zinc histochemistry for localization in salivary secretory granules. J. Histochem. Cytochem., 1987. 35(5): p. 579-583.
[136] Taylor, K.M., A distinct role in breast cancer for two LIV-1 family zinc transporters. Biochemical Society Transactions, 2008. 036(6): p. 1247-1251.
[137] Linkous, D.H., et al., Evidence That the ZNT3 Protein Controls the Total Amount of Elemental Zinc in Synaptic Vesicles. J. Histochem. Cytochem., 2008. 56(1): p. 3-6.
[138] MAWSON CA, F.M., The occurrence of zinc in the human prostate gland. Can J Med Sci., 1952. 30(4): p. 4.
[139] Rasiah, K.K., et al., Prognostic significance of Gleason pattern in patients with Gleason score 7 prostate carcinoma. Cancer, 2003. 98(12): p. 2560-2565.
[140] Zaichick, V., T. Sviridova, and S. Zaichick, Zinc concentration in human prostatic fluid: Normal, chronic prostatitis, adenoma and cancer. International Urology and Nephrology, 1996. 28(5): p. 687-694.
[141] Thompson, R.B., B.P. Maliwal, and H.-H. Zeng, Zinc biosensing with multiphoton excitation using carbonic anhydrase and improved fluorophores. Journal of Biomedical Optics, 2000. 5(1): p. 17-22.
[142] Borsic, A. and et al., Sensitivity study and optimization of a 3D electric impedance tomography prostate probe. Physiological Measurement, 2009. 30(6): p. S1.
[143] Hwang, K., et al., Improved excitation light rejection enhances small-animal fluorescent optical imaging. Mol Imaging, 2005. 4(3): p. 11.

APPPENDICES

A.1 MATLAB code for converting FEM mesh from COMSOL .mphtxt file to NIRFAST format

```
clc;clear;close all;
filename='fine.mphtxt';
%------------------------------read-in---------------------------------
---%
data=comsol_node_read(filename);
domain=comsol_domain_read(filename,27715);
elements=comsol_element_read(filename,27715);
%-----------------------------set region-------------------------------
---%
%----1_bg---2_prostate---3_blob---add later

region_tmp=ones(length(data),1);

for j=1:length(elements)
    if (domain(j)==6 || domain(j)==7)
        for i=1:4
            region_tmp(elements(j,i)+1)=2;%prostate+blob
        end
    end
end

for j=1:length(elements)
    if (domain(j)==4 || domain(j)==5)
        for i=1:4
            region_tmp(elements(j,i)+1)=1;%bg
        end
    end
end
```

```
for j=1:length(elements)
    if (domain(j)==1 || domain(j)==2 || domain(j)==3)
        for i=1:4
            region_tmp(elements(j,i)+1)=4;%rectum
        end
    end
end

for j=1:length(elements)
    if (domain(j)==4 || domain(j)==5)
        for i=1:4
            region_tmp(elements(j,i)+1)=1;%bg
        end
    end
end


%-------------------------------------------------------------------------
---%
x=data(:,1);%_0905_1449
y=data(:,2);%_0905_1449
z=data(:,3);%_0905_1449

% Tes = delaunay3(x,y,z);

sd_num=7;

x_max=80;
y_max=80;
z_max=80;
mua_pro=0.06/10;%cm->mm
mus_pro=12.7/10;%12.7
% mua_can=0.2 /10;
% mus_can=16  /10;
mua_rec=0.1 /10;
mus_rec=10   /10;
mua_sur=0.02/10;
mus_sur=8   /10;

%-------------------------------------------------------------------------
---%
mesh.name='cube_stnd_blob';
mesh.dimension=3;
mesh.type='stnd';
%-------------------------------------------------------------------------
---%
elements(:)=elements(:)+1;
mesh.elements=elements;
mesh.nodes=data;

%-----------------------set boundary-----------------------------------
---%
mesh.bndvtx=zeros(size(mesh.nodes,1),1);
```

```
for i=1:size(mesh.nodes,1)
    tmp_curve=sqrt((mesh.nodes(i,2)-
y_max/2)^2+(mesh.nodes(i,3)+40*sqrt(3))^2);
    if mesh.nodes(i,3)>=z_max-2
        mesh.bndvtx(i)=1;
%     elseif mesh.nodes(i,3)<=0.5
%         mesh.bndvtx(i)=1;
    elseif mesh.nodes(i,2)<=2
        mesh.bndvtx(i)=1;
    elseif mesh.nodes(i,2)>79
        mesh.bndvtx(i)=1;
    elseif mesh.nodes(i,1)<=2
        mesh.bndvtx(i)=1;
    elseif mesh.nodes(i,1)>=x_max-2
        mesh.bndvtx(i)=1;
%     Left the arcade unattended for removing the elements in this
area,
%     come back later
    elseif tmp_curve<=80.001 && tmp_curve>=79.999
        mesh.bndvtx(i)=1;
    end
end
%------------------------set optical property-------------------------
---%
a=ones(size(mesh.nodes,1),1);
mesh.ri=1.33.*a;%reflect index

mesh.c=a;
mesh.mua=a.*0;
mesh.mus=a.*0;
mesh.kappa=a.*0;
for i=1:length(a)
    if region_tmp(i)==1
        mesh.mua(i)=mua_sur;
        mesh.mus(i)=mus_sur;
    elseif region_tmp(i)==2
        mesh.mua(i)=mua_pro;
        mesh.mus(i)=mus_pro;
    elseif region_tmp(i)==4
        mesh.mua(i)=mua_rec;
        mesh.mus(i)=mus_rec;
    end
end

mesh.kappa=1./(3.*(mesh.mua+mesh.mus));
%------------------------sources and detectors-------------------------
sd_num=7;

x_max=80;
y_max=80;
z_max=80;
mesh.source.fixed=1;
mesh.meas.fixed=1;
for i=1:sd_num
    tmp=10.*(1+(i-1));
    mesh.source.coord(i,1)=tmp;
```

```
    mesh.meas.coord(i,1)=tmp;
    mesh.source.coord(sd_num+i,1)=tmp;
    mesh.meas.coord(sd_num+i,1)=tmp;
end


for i=1:sd_num

    mesh.source.coord(i,2)=       y_max/2-15+(-1)^mod(i,2)*5;
    mesh.meas.coord(i,2)=         y_max/2-15-(-1)^mod(i,2)*5;

    mesh.source.coord(sd_num+i,2)=y_max/2+15-(-1)^(mod(i,2))*5;
    mesh.meas.coord(sd_num+i,2)=  y_max/2+15+(-1)^(mod(i,2))*5;

end
% clc;clear;
% load('pre.mat')
mesh.source.coord(:,3)=0;
mesh.meas.coord(:,3)=0;

for i=1:2*sd_num
    if mesh.source.coord(i,2)==60 || mesh.source.coord(i,2)==20
        mesh.source.coord(i,3)=sqrt(80^2-20^2)-40*sqrt(3)+1e-4;
    else
        mesh.source.coord(i,3)=sqrt(80^2-10^2)-40*sqrt(3)+1e-4;
    end


    if mesh.meas.coord(i,2)==60 || mesh.meas.coord(i,2)==20
        mesh.meas.coord(i,3)=  sqrt(80^2-20^2)-40*sqrt(3)+1e-4;
    else
        mesh.meas.coord(i,3)=  sqrt(80^2-10^2)-40*sqrt(3)+1e-4;
    end
end

%----------------------------link-----------------------------------------
for i=1:2*sd_num
    mesh.link(i,:)=1:2*sd_num;
end
%-------------------------------------------------------------------------
% save_mesh(mesh,'cube_stnd_recon_basis');
save_mesh(mesh,'cube_stnd_blob');

function data=comsol_node_read(filename)
fid=fopen(filename);

%nodes coord starts
start='# Mesh point coordinates';
finish='';

data=[];

sta=0;%status flag
i=1;
```

```
while(not(feof(fid)))
    if sta==0
        line=fgetl(fid);
        if isequal(start,line)
            sta=1;
        end
    elseif sta==1
        line=fgetl(fid);
        if isequal(finish,line)
            sta=2;
        else
            data(i,:)=str2num(line);
            i=i+1;
        end
    elseif sta==2
        break;
    end
end

function elements=comsol_element_read(filename,num_element)
fid=fopen(filename);
str_element=num2str(num_element);
%nodes coord starts
start_e1=cat(2,str_element,' # number of elements');
start_e2='# Elements';
finish='';

elements=[];

sta=0;
i=1;
while(not(feof(fid)))
    if sta==0
        line=fgetl(fid);
        if isequal(start_e1(1:end),line(1:end))
            sta=1;
        end
    elseif sta==1
        line=fgetl(fid);
        if isequal(start_e2,line)
            sta=2;
        end
    elseif sta==2
        line=fgetl(fid);
        if isequal(finish,line)
            sta=3;
        else
            elements(i,:)=str2num(line);
            i=i+1;
        end
    elseif sta==3
        break;
    end
end
```

```
function domain=comsol_domain_read(filename,num_domain)
fid=fopen(filename);
str_domain=num2str(num_domain);
%nodes coord starts
start1=cat(2,str_domain,' # number of domains');
start2='# Domains';

finish='';

domain=[];

sta=0;%status flag
i=1;

while(not(feof(fid)))
    if sta==0
        line=fgetl(fid);
        if isequal(start1(1:end),line(1:end))
            sta=1;
        end
    elseif sta==1
        line=fgetl(fid);
        if isequal(start2,line)
            sta=2;
        end
    elseif sta==2
        line=fgetl(fid);
        if isequal(finish,line)
            sta=3;
        else
            domain(i,:)=str2num(line);
            i=i+1;
        end
    elseif sta==3
        break;
    end
end
```

A.2 Derivation of PRUL model for multispectral optical tomography case

Starting from equ. (4.2-μ_s')

$$\mu_s' = A\lambda^{-b}$$

Take logarithm of both sides:

$$\log \mu_s' = \log A + (-b)\log \lambda \tag{A.1}$$

For multiple measurements, use matrix form:

$$\begin{bmatrix} \log[\mu_s'(\lambda_1)] \\ \log[\mu_s'(\lambda_2)] \\ \dots \\ \log[\mu_s'(\lambda_n)] \end{bmatrix} = \begin{bmatrix} 1 & \log\lambda_1 \\ 1 & \log\lambda_2 \\ \dots & \dots \\ 1 & \log\lambda_n \end{bmatrix} \times \begin{bmatrix} \log A \\ (-b) \end{bmatrix} \tag{A.2}$$

Multiple both side with $\begin{bmatrix} 1 & 1 & \dots & 1 \\ \log(\lambda_1) & \log(\lambda_2) & \dots & \log(\lambda_n) \end{bmatrix}$,

Left hand side of equ.)becomes:

$$\begin{bmatrix} 1 & 1 & \dots & 1 \\ \log(\lambda_1) & \log(\lambda_2) & \dots & \log(\lambda_n) \end{bmatrix} \times \begin{bmatrix} \log[\mu_s'(\lambda_1)] \\ \log[\mu_s'(\lambda_2)] \\ \dots \\ \log[\mu_s'(\lambda_n)] \end{bmatrix} = \begin{bmatrix} \sum_{i=1}^{n} \log[\mu_s'(\lambda_i)] \\ \sum_{i=1}^{n} \log(\lambda_i)\log[\mu_s'(\lambda_i)] \end{bmatrix} \tag{A.3}$$

Right hand side becomes:

$$\begin{bmatrix} 1 & 1 & \dots & 1 \\ \log(\lambda_1) & \log(\lambda_2) & \dots & \log(\lambda_n) \end{bmatrix} \times \begin{bmatrix} 1 & \log(\lambda_1) \\ 1 & \log(\lambda_2) \\ \dots & \dots \\ 1 & \log(\lambda_n) \end{bmatrix} \times \begin{bmatrix} \log A \\ (-b) \end{bmatrix}$$

$$= \begin{bmatrix} n & \sum_{i=1}^{n} \log(\lambda_i) \\ \sum_{i=1}^{n} \log(\lambda_i) & \sum_{i=1}^{n} \log^2(\lambda_i) \end{bmatrix} \times \begin{bmatrix} \log A \\ (-b) \end{bmatrix} \tag{A.4}$$

Solve for $\begin{bmatrix} \log A \\ (-b) \end{bmatrix}$ from (A.4):

$$\begin{bmatrix} \log A \\ (-b) \end{bmatrix} = \begin{bmatrix} n & \sum_{i=1}^{n} \log(\lambda_i) \\ \sum_{i=1}^{n} \log(\lambda_i) & \sum_{i=1}^{n} \log^2(\lambda_i) \end{bmatrix}^{-1} \times \begin{bmatrix} \sum_{i=1}^{n} \log[\mu_s'(\lambda_i)] \\ \sum_{i=1}^{n} \log(\lambda_i)\log[\mu_s'(\lambda_i)] \end{bmatrix} \tag{A.5}$$

where

$$\begin{bmatrix} n & \sum_{i=1}^{n}\log(\lambda_i) \\ \sum_{i=1}^{n}\log(\lambda_i) & \sum_{i=1}^{n}\log^2(\lambda_i) \end{bmatrix}^{-1} = \begin{bmatrix} \sum_{i=1}^{n}\log^2(\lambda_i) & -\sum_{i=1}^{n}\log(\lambda_i) \\ -\sum_{i=1}^{n}\log(\lambda_i) & n \end{bmatrix} \cdot \frac{1}{n\sum_{i=1}^{n}\log^2(\lambda_i) - [\sum_{i=1}^{n}\log(\lambda_i)]^2} \quad \text{(A.6)}$$

Therefore,

$$\begin{bmatrix} \log A \\ (-b) \end{bmatrix} = \frac{1}{n\sum_{i=1}^{n}\log^2(\lambda_i) - [\sum_{i=1}^{n}\log(\lambda_i)]^2} \cdot \begin{bmatrix} \sum_{i=1}^{n}\log^2(\lambda_i) & -\sum_{i=1}^{n}\log(\lambda_i) \\ -\sum_{i=1}^{n}\log(\lambda_i) & n \end{bmatrix} \times \begin{bmatrix} \sum_{i=1}^{n}\log[\mu_s'(\lambda_i)] \\ \sum_{i=1}^{n}\log(\lambda_i)\log[\mu_s'(\lambda_i)] \end{bmatrix} \quad \text{(A.7)}$$

And log(A) and b can be respectively expressed as:

$$\log A = \frac{1}{n\sum_{i=1}^{n}\log^2(\lambda_i) - [\sum_{i=1}^{n}\log(\lambda_i)]^2} \cdot \left[\sum_{i=1}^{n}\log^2(\lambda_i) \cdot \sum_{i=1}^{n}\log[\mu_s'(\lambda_i)] - \sum_{i=1}^{n}\log(\lambda_i) \cdot \sum_{i=1}^{n}\log(\lambda_i)\log[\mu_s'(\lambda_i)] \right] \quad \text{(A.8)}$$

$$b = \frac{1}{n\sum_{i=1}^{n}\log^2(\lambda_i) - [\sum_{i=1}^{n}\log(\lambda_i)]^2} \cdot \left[-\sum_{i=1}^{n}\log(\lambda_i) \cdot \sum_{i=1}^{n}\log[\mu_s'(\lambda_i)] + n\sum_{i=1}^{n}\log(\lambda_i)\log[\mu_s'(\lambda_i)] \right] \quad \text{(A.9)}$$

To Compare log(A) and b, the common terms need to be extracted:

$$\log A = \sum_{i=1}^{n}\log^2(\lambda_i) \cdot \begin{bmatrix} 1 & 1 & \dots & 1 \end{bmatrix} \times \begin{bmatrix} \log[\mu_s'(\lambda_1)] \\ \log[\mu_s'(\lambda_2)] \\ \dots \\ \log[\mu_s'(\lambda_n)] \end{bmatrix} - \sum_{i=1}^{n}\log(\lambda_i) \cdot \begin{bmatrix} \log(\lambda_1) \\ \log(\lambda_2) \\ \dots \\ \log(\lambda_n) \end{bmatrix}^T \times \begin{bmatrix} \log[\mu_s'(\lambda_1)] \\ \log[\mu_s'(\lambda_2)] \\ \dots \\ \log[\mu_s'(\lambda_n)] \end{bmatrix}$$

$$= \begin{bmatrix} \sum_{i=1}^{n}\log^2(\lambda_i) - \log(\lambda_1)\log[\mu_s'(\lambda_1)] \\ \sum_{i=1}^{n}\log^2(\lambda_i) - \log(\lambda_2)\log[\mu_s'(\lambda_2)] \\ \dots \\ \sum_{i=1}^{n}\log^2(\lambda_i) - \log(\lambda_n)\log[\mu_s'(\lambda_n)] \end{bmatrix}^T \times \begin{bmatrix} \log[\mu_s'(\lambda_1)] \\ \log[\mu_s'(\lambda_2)] \\ \dots \\ \log[\mu_s'(\lambda_n)] \end{bmatrix} \quad \text{(A.10)}$$

$$(-b)=\sum_{i=1}^{n}\log^2(\lambda_i)\cdot[1\quad 1\quad \ldots\quad 1]\times\begin{bmatrix}\log[\mu_s'(\lambda_1)]\\ \log[\mu_s'(\lambda_2)]\\ \ldots\\ \log[\mu_s'(\lambda_n)]\end{bmatrix}+n\cdot\begin{bmatrix}\log(\lambda_1)\\ \log(\lambda_2)\\ \ldots\\ \log(\lambda_n)\end{bmatrix}^T\times\begin{bmatrix}\log[\mu_s'(\lambda_1)]\\ \log[\mu_s'(\lambda_2)]\\ \ldots\\ \log[\mu_s'(\lambda_n)]\end{bmatrix}$$

$$=\begin{bmatrix}\sum_{i=1}^{n}\log^2(\lambda_i)+n\cdot\log(\lambda_1)\\ \sum_{i=1}^{n}\log^2(\lambda_i)+n\cdot\log(\lambda_2)\\ \ldots\\ \sum_{i=1}^{n}\log^2(\lambda_i)+n\cdot\log(\lambda_n)\end{bmatrix}^T\times\begin{bmatrix}\log[\mu_s'(\lambda_1)]\\ \log[\mu_s'(\lambda_2)]\\ \ldots\\ \log[\mu_s'(\lambda_n)]\end{bmatrix} \tag{A.11}$$

Therefore, comparison between log(A) and (-b) only need to consider the different factors on the right hand side of equ.s (A.10) and (A.11)

A.3 LabView interface and diagram for source-sweeping and CCD exposure synchronization

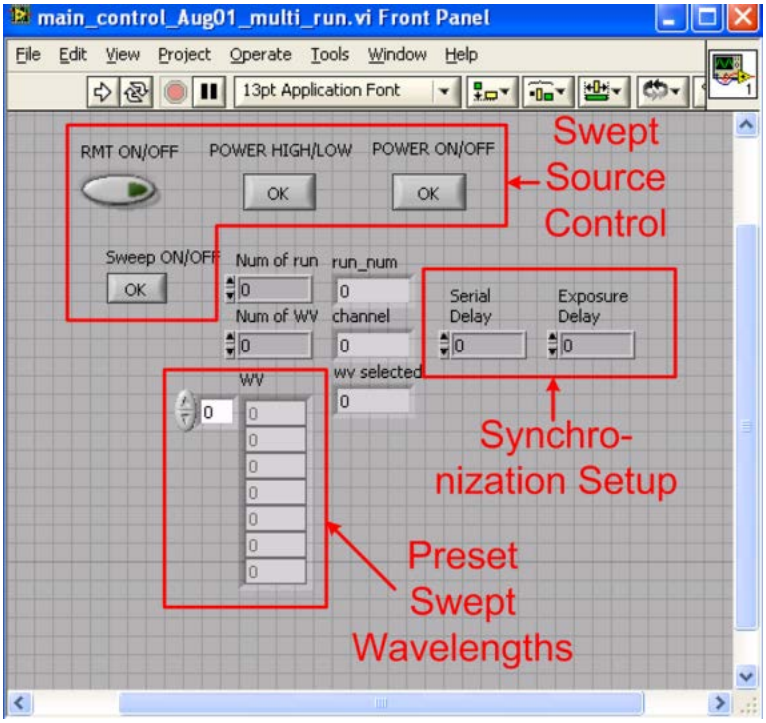

(a)

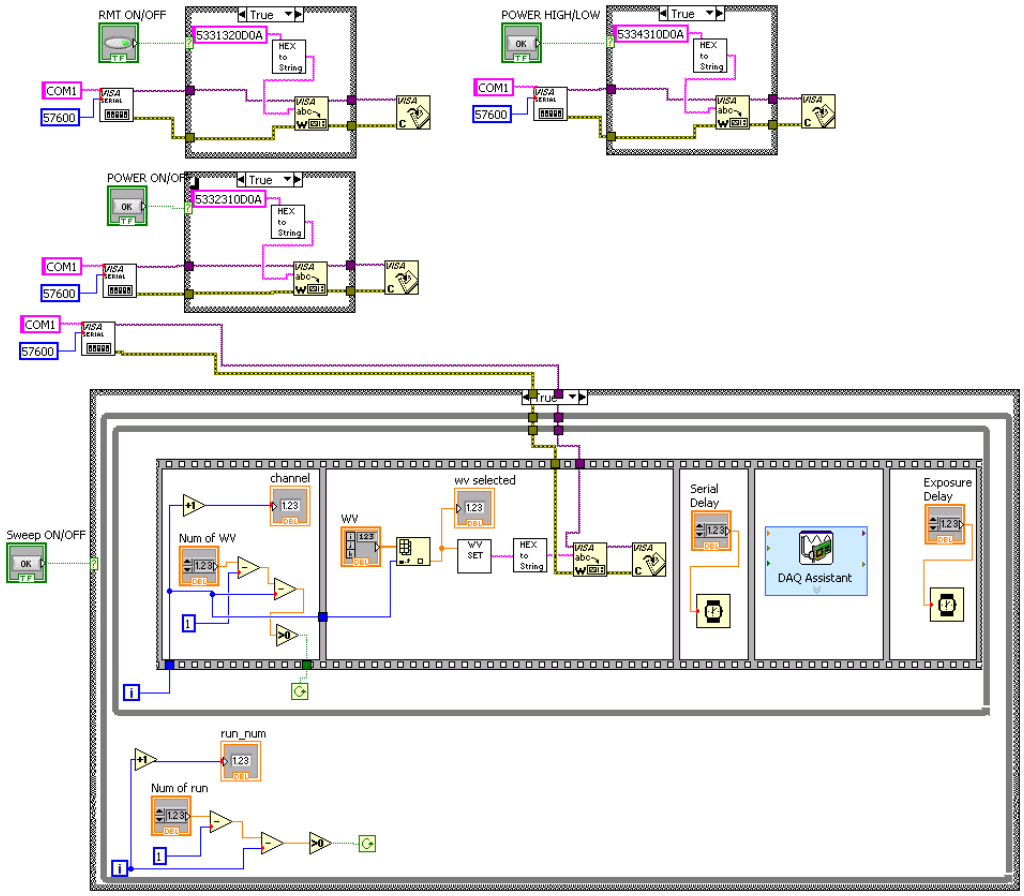

(b)

Fig.A.1 Labview interface and block diagram of the system

(a) Control interface (b) Block diagram

A.4 Linear transformation from conventional to geometric differential sensitivity profile

```
function J_geom_derv_dc=jacob_dc_stnd2geom(J_dc,mesh)

d_sta_num=1;
d_end_num=1;
s_num=size(mesh.link,1);
d_num=size(mesh.link,2);

  J_geom_derv_dc=[];

  for i=1:s_num
      for j=d_sta_num:d_num-d_end_num%
          J_geom_derv_tmp  =J_dc( (i-1)*d_num+1  :(i-1)*d_num+d_num-j,:
)-...
                           J_dc( (i-1)*d_num+1+j:(i-1)*d_num+d_num  ,:
);
          J_d_tmp=[];
```

```
            for k=1:size(J_geom_derv_tmp,2)
                J_d_tmp=[J_d_tmp J_geom_derv_tmp(:,k)];
            end
            J_geom_derv_dc=[J_geom_derv_dc;J_d_tmp];
        end
    end
```

VITA

GUAN XU

Candidate for the Degree of

Doctor of Philosophy/Education

Thesis: ENHANCEMENT OF NEAR-INFRARED DIFFUSE OPTICAL TOMOGRAPHY FOR PROSTATE CANCER IMAGING

Major Field: Electrical Engineering

Biographical:

Education:

Completed the requirements for the Doctor of Philosophy in Electrical Engineering at Oklahoma State University, Stillwater, Oklahoma in December, 2011.

Completed the requirements for the Bachelor of Science in your Electrical Engineering at Hebei Universityof Technology, Tianjin, China in 2006.

Experience:

Research Assistant (PhD program) 08/2006---present
School of Electrical and Computer Engineering, Oklahoma State University, Stillwater, OK
Computational modeling and instrumentation of Biomedical Optics

Research Assistant 08/2004---06/2006
School of Information Engineering, Hebei University of Technology, Tianjin, China
Intelligent information processing

Professional Memberships:

Student Member Society for Optical Engineering (**SPIE**)
Student Member Optical Society of America (**OSA**)
Student Member Institute of Electrical and Electronics Engineers (**IEEE**)

Name: GUAN XU Date of Degree: December, 2011

Institution: Oklahoma State University Location: Stillwater, Oklahoma

Title of Study: ENHANCEMENT OF NEAR-INFRARED DIFFUSE OPTICAL TOMOGRAPHY FOR PROSTATE CANCER IMAGING

Pages in Study: 172 Candidate for the Degree of Doctor of Philosophy

Major Field: Electrical Engineering

Scope and Method of Study:

The objective of this study is to enhance the functional imaging modality of Diffuse Optical Tomography (DOT) for the early diagnosis and accurate detection of prostate cancer. Enhancement approaches such as spatial *prior* extracted from Trans-Rectal Ultrasound (TRUS), spectral *prior* pre-calibrated with the absorption chromophores in biological tissue and metabolic fluorescence emitting biomarker has been implemented by either instrumentation or computational modeling techniques.

Findings and Conclusions:

A hard *prior* based hierarchical reconstruction algorithm for a TRUS-DOT combined system is developed and validated by both simulation and tissue phantom experiments.

A Parametric Recovery Uncertainty Level (PRUL) model is derived for DOT reconstruction based on measurements at both single and multiple wavelengths. The model indicates that steady state DOT system could produce reconstruction results comparable to frequency domain systems and direct current measurement components are not redundant in frequency domain reconstruction. The model can also be used to optimize the wavelength combination in multispectral optical imaging systems.

A rapid DOT system is fabricated based on a wavelength-swept light source. The system is validated by phantom experiments and is readily extendable for fluorescence signal acquisition.

A geometric-differential-sensitivity reconstruction algorithm is developed for reflectance imaging geometry in DOT for accurate target depth recovery.

The experiment setup for FDOT validation is designed. Preliminary simulation results support the hypothesis that the reverse fluorohphore uptake can be recovered within our imaging geometry.

ADVISER'S APPROVAL: Dr. Daqing Piao